

Spring 5-2009

Magnetic and Dielectric Properties of Sulfonated (S) Poly[(styrene)-(ethylene-co-butylene)-(styrene)] (SEBS) Block Copolymer/Magnetic Metal Oxide Nanocomposites Synthesized Via an In-situ Precipitation Method

Sateesh Kumar Peddini
University of Southern Mississippi

Follow this and additional works at: <https://aquila.usm.edu/dissertations>

 Part of the [Materials Chemistry Commons](#), and the [Polymer Chemistry Commons](#)

Recommended Citation

Peddini, Sateesh Kumar, "Magnetic and Dielectric Properties of Sulfonated (S) Poly[(styrene)-(ethylene-co-butylene)-(styrene)] (SEBS) Block Copolymer/Magnetic Metal Oxide Nanocomposites Synthesized Via an In-situ Precipitation Method" (2009). *Dissertations*. 1040.
<https://aquila.usm.edu/dissertations/1040>

This Dissertation is brought to you for free and open access by The Aquila Digital Community. It has been accepted for inclusion in Dissertations by an authorized administrator of The Aquila Digital Community. For more information, please contact aquilastaff@usm.edu.

The University of Southern Mississippi

MAGNETIC AND DIELECTRIC PROPERTIES OF SULFONATED (S) POLY
[(STYRENE)-(ETHYLENE-CO-BUTYLENE)-(STYRENE)] (SEBS) BLOCK
COPOLYMER/MAGNETIC METAL OXIDE NANOCOMPOSITES SYNTHESIZED
VIA AN *IN-SITU* PRECIPITATION METHOD

by

Sateesh Kumar Peddini

Abstract of a Dissertation
Submitted to the Graduate Studies Office
of The University of Southern Mississippi
in Partial Fulfillment of the Requirements
for the Degree of Doctor of Philosophy

May 2009

COPYRIGHT BY
SATEESH KUMAR PEDDINI

2009

The University of Southern Mississippi

MAGNETIC AND DIELECTRIC PROPERTIES OF SULFONATED (S) POLY
[(STYRENE)-(ETHYLENE-CO-BUTYLENE)-(STYRENE)] (SEBS) BLOCK
COPOLYMER/MAGNETIC METAL OXIDE NANOCOMPOSITES SYNTHESIZED
VIA AN IN-SITU PRECIPITATION METHOD

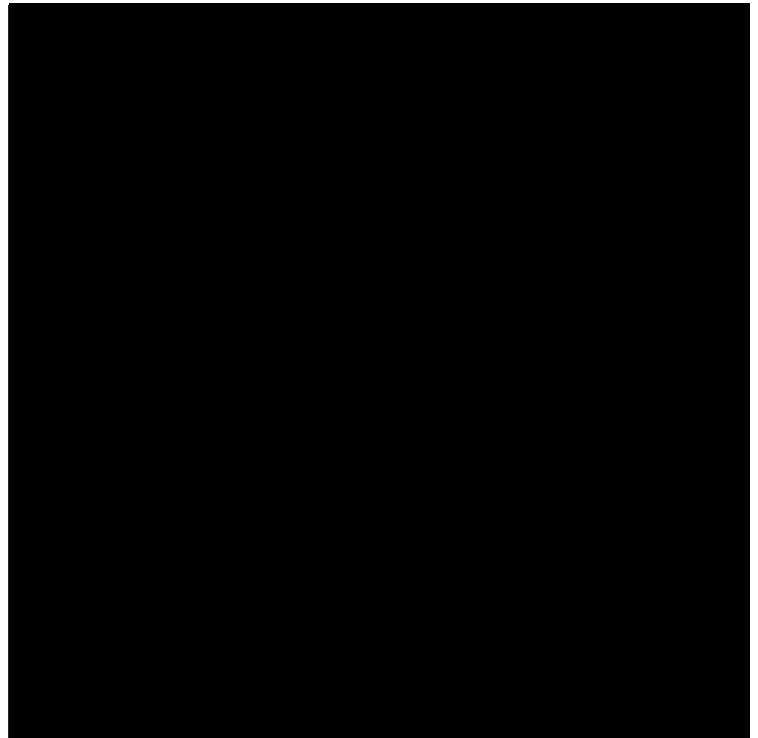
by

Sateesh Kumar Peddini

A Dissertation

Submitted to the Graduate Studies Office
of The University of Southern Mississippi
in Partial Fulfillment of the Requirements
for the Degree of Doctor of Philosophy

Approved:



May 2009

ABSTRACT

MAGNETIC AND DIELECTRIC PROPERTIES OF SULFONATED (S) POLY [(STYRENE)-(ETHYLENE-CO-BUTYLENE)-(STYRENE)] (SEBS) BLOCK COPOLYMER/MAGNETIC METAL OXIDE NANOCOMPOSITES SYNTHESIZED VIA AN *IN-SITU* PRECIPITATION METHOD

by Sateesh Kumar Peddini

May 2009

Block copolymer/magnetic metal oxide nanocomposites were synthesized by growing metal oxide nanoparticles (cobalt ferrite, CoFe_2O_4 and iron oxide, $\alpha\text{-Fe}_2\text{O}_3$) in sulfonated (s) poly (styrene) (PS) block domains of sulfonated poly [(styrene)-(ethylene-co-butylene)-(styrene)] (SEBS) BCP preformed films via an in-situ precipitation method by dissolving the salts of respective metal chloride (s) in a suitable solvent that selectively swells the sPS regions. Inorganic uptake was determined using thermogravimetric analysis (TGA), and it was observed that none of the samples incorporated more than 5 wt % of the inorganic component. Dynamical mechanical analysis was used to observe the changes in the glass transition temperatures (T_g) in both blocks of the BCP by plotting $\tan \delta$ vs. temperature responses in tensile mode on all samples. The results showed that the T_g of the sPS block domains increased with sulfonation level and further increased with the incorporation of both nanoparticles in the same blocks, indicating that growth of nanoparticles takes place only in sPS blocks. The crystalline structure of the nanoparticles was observed using wide angle X-ray diffractometry (WAXD), and it was determined that cobalt iron oxide nanoparticles in 20 mole % sulfonated SEBS exhibited an inverse spinel structure confirming the structure to

be CoFe_2O_4 . And with iron oxide nanoparticles in 10 mole % sulfonated SEBS exhibiting a hematite ($\alpha\text{-Fe}_2\text{O}_3$) phase. Transmission electron microscopy (TEM) was used to investigate the particle size and distribution of nanoparticles in sBCP matrices at all sulfonation levels. Select area electron diffraction in TEM was used to determine crystalline structures of individual nanoparticles to compare with the structure observed from WAXD.

The changes in thickness of interfaces between the individual PS and EB block domains with increase in sulfonation of PS blocks were investigated semi-quantitatively using tapping mode atomic force microscopy. The interfacial thickness decreased with the increase in sulfonation level up to 16 mole% and then increased from there onwards until 20 mole % sulfonation.

Magnetometric measurements were conducted on samples incorporated with inorganic metal oxide nanoparticles using an alternating gradient magnetometer at room temperature; and the samples showed superparamagnetism. Magnetic properties at temperatures near absolute zero and above were measured using a superconducting quantum interference device magnetometer and samples exhibited some magnetic hysteresis; hence they are ferrimagnetic. Zero field cooled and field cooled measurements were conducted on samples to determine the transition temperature at which the inorganic metal oxide transitions from being ferri- to superparamagnetic. Dielectric spectroscopy measurements were conducted on iron oxide nanoparticles in sSEBS matrices to observe the presence of nanoparticles in the PS blocks; the effect of nanoparticles on relaxation times and glass transition temperatures was investigated.

DEDICATION

To all mothers in the world for their endless patience

ACKNOWLEDGEMENTS

I would first like to thank my advisor Dr. Kenneth Mauritz for his valuable guidance, encouragement, help and wisdom throughout this project. I have sincere gratitude and veneration for him for his integrity, making me a good research student and also for providing me vast freedom in research. He is a cornucopia of knowledge in various scientific topics and I learned so many things from each and every discussion with him. I also thank my committee members, Drs. Robson Storey, Robert Lochhead, Charles Hoyle, and Sergei Nazarenko for their support over past several years.

Additionally, I would like to thank the past and present members of Mauritz Research Group for their help. I specially thank Dr. Kopchick for his patience to train me on various characterization techniques, Dr. Rajan for helping me to start working with magnetic measurements. I cannot forget the help that Dr. Hassan and Dr. Rhoades provided with understanding dielectric relaxation spectroscopy. I would also like to thank Dr. Patil for his valuable input and educational discussions during the past couple of years.

I would also like to extend my thanks to Drs. Nikles, Weston, Miao, and Shamshozzoha at the MINT Center at The University of Alabama for collaboration and providing magnetometry related measurements and discussions on magnetism-related issues. I would also like to thank Dr. Spinu, Dr. Radu and Huay Pham at AMRI at The University of New Orleans for sharing advanced magnetometry instruments.

I would like to thank Sara Bayley for her endless patience to train me on TEM and also on other characterization techniques. I would like to acknowledge Dr. Jarrett for his help in software-related issues. I would like to thank Steve Selph for helping me on

instrumentation repairs at the beginning of my research work. In the Polymer science department, I would like to thank Bret Calhoun, Machel Haynes, and Erin Price for helping me with course-related issues, and I cannot forget to thank Beverly McNeese for her help in assisting with auditorium reservations for practice talks. I would like to extend a special acknowledgement for Laura Fosselman for her help, encouragement and administrative capabilities which helped me till the end of my research. I would also like to thank The Polymer Science Department for giving me an opportunity to come and work at this wonderful facility.

I cannot forget to express my gratitude towards all my fall 2004 classmates, who were instrumental to help me understand American culture, improve my English language, and many other things. I would like to thank my good friend Andy Magenau for synthesizing SIBS block copolymers for me.

I would like to acknowledge the National Science Foundation (NSF) Material Research Science and Engineering Center (MRSEC) Division of Materials Research (DMR-0213883) for Stimuli Responsive Materials at the University of Southern Mississippi for funding. Being a part of MRSEC helped me attend different conferences and allowed me to access different shared facilities at other universities.

I would like to thank my best buddies Rupesh and Pavan for their providing endless encouragement and support, and I would also like to thank my friend Dana for having valuable discussions on different general issues.

Finally, and most importantly, I would like to thank my family for their unwavering support and trust in me throughout the entire process. I cannot forget the courage of my mother to send me back to the States immediately after loss of my father.

She is the whole reason for what I am now. I would like to thanks my sister for her caring nature and her precious kids, my niece and nephew, Bhavani and Pavan, who became an important part of my life.

I would like to thank Swamiji for his important teachings which made me know myself better.

TABLE OF CONTENTS

ABSTRACT	ii
DEDICATION	iv
ACKNOWLEDGEMENTS	v
LIST OF ILLUSTRATIONS	xii
LIST OF TABLES	xvi
CHAPTER	
I. INTRODUCTION	1
Introduction	
Polymer Matrix	
<i>Block Copolymers</i>	
<i>Morphology</i>	
<i>Properties</i>	
Styrene Containing BCPs	
<i>Sulfonated (s) poly (styrene-ethylene-co-butylene-styrene) (sSEBS)</i>	
Magnetic Nanoparticles	
Preparation techniques	
Magnetism Overview	
<i>Fundamentals of Magnetism</i>	
<i>Magnetic Domains and Domain Walls</i>	
<i>Magnetization and Hysteresis</i>	
Types of Magnetism and Magnetic Materials	
<i>Diamagnetism</i>	
<i>Paramagnetism</i>	
<i>Ferromagnetism</i>	
<i>Antiferromagnetism</i>	
<i>Ferrimagnetism</i>	
<i>Superparamagnetism</i>	
Magnetic Anisotropy	
<i>In-situ</i> Precipitation Method	
Dielectric Relaxation Spectroscopy	
<i>Static Polarization</i>	
<i>Dynamic Polarization</i>	
Dynamic Magnetic Relaxation	
Conclusions	
References	

CHAPTER

II. EXPERIMENTAL.....41

Introduction
Transmission Electron Microscopy (TEM)
Magnetic Measurements
Superconducting Quantum Interference Device (SQUID) Magnetometer
Zero-Field Cooled (ZFC) and Field Cooled (FC) Magnetic Measurements
Alternating Gradient Magnetometer (AGM)
References

CHAPTER

III SECTIONAL ANALYSIS OF POLY [(STYRENE)-(ETHYLENE/BUTYLENE)-(STYRENE)] TRIBLOCK COPOLYMERS USING ATOMIC FORCE MICROSCOPY: CHANGES IN INTERFACIAL THICKNESS WITH SULFONATION47

Abstract
Introduction
Experimental
Materials
Sulfonation Procedure
Film Casting Procedure
Samples for AFM and DMA Investigations
AFM and DMA Measurements
Results and Discussion
Conclusions
Acknowledgements
References

CHAPTER

IV STRUCTURE AND PROPERTIES OF SULFONATED POLY [STYRENE-b-(ETHYLENE-co-BUTYLENE)-b- STYRENE]/ [COBALT FERRITE] NANOCOMPOSITES69

Abstract
Introduction
Experimental
Materials
Sulfonation and Film Formation
Metal Oxide Nanoparticle Incorporation
Material Structure/Property Characterization

Results and Discussion
Conclusions
Acknowledgements
References

CHAPTER

V MORPHOLOGY AND MAGNETIC PROPERTIES OF SULFONATED POLY [STYRENE-(ETHYLENE/BUTYLENE)-STYRENE]/ IRON OXIDE COMPOSITES.....92

Abstract
Introduction
Experimental
 Materials
 Sulfonation Reaction
 Metal Oxide Incorporation
 Material Characterization
Results and Discussion
 Sample Analysis
 Morphology
Conclusions
Acknowledgements
References

CHAPTER

VI BROADBAND DIELECTRIC SPECTROSCOPIC CHARACTERIZATION OF SULFONATED POLY [STYRENE-(ETHYLENE/BUTYLENE)-STYRENE]/ IRON OXIDE COMPOSITES GROWN VIA AN IN-SITU PRECIPITATION METHOD118

Abstract
Introduction
 Broadband Dielectric Spectroscopy (BDS)
Experimental
 Materials
 Sulfonation Procedure
 Film Casting Procedure
 Metal Oxide Incorporation
 Samples for AFM and BDS Investigations
Material Characterization
 Fourier Transform Infrared spectroscopy (FTIR)
 AFM
 Dielectric Spectroscopy Measurements
Results and Discussion

Conclusions
Acknowledgements
References

LIST OF ILLUSTRATIONS

Figure

I-1.	Schematic representation of PS based triblock copolymers with IB block as rubbery center block.	4
I-2.	Range of possible equilibrium morphologies for A-B-A triblock copolymers.	6
I-3.	Schematic representation of magnetic domains separated by magnetic domain walls in a multi-domain magnetic nanoparticle.	13
I-4.	Typical M-H curve for a magnetic material with hysteresis.	15
I-5.	M-H curve for a diamagnetic material.	17
I-6.	M vs. H for a paramagnetic material showing no hysteresis.	18
I-7.	Alignment of magnetic moments in zero applied magnetic fields at room temperature for A) paramagnetic or superparamagnetic, B) ferromagnetic, C) antiferromagnetic and D) ferrimagnetic materials.	20
I-8.	Three crystalline structures A) cubic, B) inverse spinel, and C) hexagonal structures exhibited by most of the ferrimagnetic/ferromagnetic materials.	22
I-9.	Depiction of magnetic domain nature from multi-domain to superparamagnetic with decreasing the particle diameter and its effect on coercivity.....	24
I-10.	Depiction of easy and hard axes of magnetization in bcc Fe, fcc Ni and hcp Co.	25
I-11.	Depiction of in-situ precipitation of CoFe_2O_4 nanoparticles in sPS domains.	26
I-12.	Depiction of electric field between two parallel plate electrodes of equal and opposite charges Q with vacuum in between.	27
I-13.	Unbalanced electric charges at the interfaces between a dielectric and electrodes on application of electric field.	28
I-14.	Types of polarization mechanisms at different times scales of measurement. Typical BDS test window of 10^{-6} to 10^2 sec also shown.	30

I-15.	A schematic representation of complex polarization P^* ($= P_\infty + P_1 + P_2$) as a function of angular frequency ($\omega = 2\pi f$). $P_\infty + P_1$ contains the storage component P_1 and the loss component P_2	32
I-16.	Hypothetical magnetic loss permeability μ'' as a function of frequency by, f.	34
II-1.	SAED patterns for two different samples. A) ring pattern for multi crystalline structure, B) dot pattern for a single crystalline structure.	42
II-2.	Schematic representation of a Josephson junction electric circuit in SQUID magnetometer.	43
III-1.	Hypothetical concentration profiles of A and B components in a mixed interface (interphase) region of an immiscible polymer blend or phase separated block copolymer where the concentrations of A and B are equal.....	48
III-2.	Molecular view of limited block miscibility at the interface in phase separated block copolymers.	49
III-3.	Graph of driving force - response phase lag in AFM measurements when a cantilever tip is in contact with substrate surface in tapping mode.	51
III-4 (a-e).	TM-AFM phase images of 0SEBS, 6SEBS, 10SEBS, 16SEBS, and 20SEBS respectively. Lines along which sectional analysis was performed are in white.	56
III-5 (a-e).	Representative sectional analysis profiles at single locations on samples 0SEBS, 6SEBS, 10SEBS, 16SEBS and 20SEBS, respectively.	59
III-6.	Graphical description of method of determining interfacial thickness (d) from AFM tapping-phase profiles.	62
III-7.	Tan δ vs. T plots for samples 0SEBS, 6SEBS, 10SEBS, 16SEBS and 20SEBS.	64
IV-1.	Wide angle X-ray diffraction peaks for a 20.0% sSEBS sample incorporating CoFe_2O_4 particles.	75
IV-2.	TEM micrograph for 16.4% sSEBS incorporating CoFe_2O_4 nanoparticles. Scale bar at lower-left is 200 nm.	77
IV-3.	TEM micrograph for 20.0% sSEBS incorporating CoFe_2O_4 nanoparticles. The scale bar at lower-left is 100 nm.	78

IV-4.	TGA thermograms for sSEBS/cobalt ferrite nanocomposites having two percent sulfonations	79
IV-5.	Tan δ vs. T curves for unmodified SEBS, 16.4% sSEBS and 16.4% sSEBS incorporating CoFe_2O_4	80
IV-6.	Dynamic mechanical tan δ vs. T curves for unmodified SEBS, 20% sSEBS and 20.0% sSEBS incorporating CoFe_2O_4	80
IV-7.	Room temperature AGM scans of magnetization (in electromagnetic units [emu]/g) vs. applied magnetic field (in Oersteds = Oe) for sSEBS/ CoFe_2O_4 nanocomposites having the indicated SEBS sulfonation percents.	83
IV-8.	ZFC and FC plots for [20.0% sSEBS]/ CoFe_2O_4 obtained using SQUID.	85
V-1 (a-c).	TGA scans of 10SEBS/iron oxide, 16SEBS/iron oxide and 20SEBS/iron oxide, respectively.	98
V-2.	WAXD scan for the 10SEBS/iron oxide nanocomposite having 3.3 wt% iron oxide filler. Miller indices of prominent reflections are indicated.....	100
V-3 (a-c).	TEM micrographs of 10SEBS/iron oxide, 16SEBS/iron oxide and 20SEBS/iron oxide, respectively. The image insets are SAED diffraction patterns of iron oxide crystalline structures.....	102
V-4.	Tan δ vs. T for (a) 10SEBS/iron oxide, (b) 16SEBS/iron oxide and (c) 20SEBS/iron oxide, respectively.	103
V-5 (a-c).	ZFC-FC plots of 10SEBS/iron oxide, 16SEBS/iron oxide and 20SEBS/iron oxide measured at 50 and 100 Oe, respectively.	106
V-6 (a-c).	Overlay M vs. H plots measured at temperatures of 5, 150 and 300 K for 10SEBS/iron oxide, 16SEBS/iron oxide and 20SEBS/iron oxide, respectively.	109
VI-1.	FTIR/ATR absorbance spectra of sulfonated and unsulfonated SEBS.....	129
VI-2 (a-b).	TMAFM phase images of 16SEBS/iron oxide and 20SEBS/iron oxide showing nanoparticles size of ~ 75 nm, respectively.....	130
VI-3.	3D surface showing ϵ'' versus $\log_{10}f$ versus temperature for 0SEBS sample. .	131
VI-4 (a-e).	ϵ'' versus $\log_{10}f$ plots for 0SEBS, 16SEBS, 16SEBS/iron oxide, 20SEBS, 20SEBS/iron oxide, respectively in EB block region. (The contribution of DC conductivity is subtracted from ϵ'' data in above all five figures).	132

VI-5 (a-e). ϵ'' vs. $\log_{10} f$ for 0SEBS, 16SEBS, 16SEBS/iron oxide, 20SEBS, 20SEBS/iron oxide, respectively, for PS block domain relaxation. (The contribution of DC conductivity is subtracted from ϵ'' data in above all five figures).	135
VI-6 (a-e). ϵ' versus $\log_{10} f$ plots for 0SEBS, 16SEBS, 16SEBS/iron oxide, 20SEBS, 20SEBS/iron oxide, respectively in EB block region. (The contribution of DC conductivity is subtracted from ϵ'' data in above all five figures).	139
VI-7 (a-e). ϵ' vs. $\log_{10} f$ for 0SEBS, 16SEBS, 16SEBS/iron oxide, 20SEBS, 20SEBS/iron oxide, respectively, for PS block domain relaxation. (The contribution of DC conductivity is subtracted from ϵ'' data in above all five figures).	141
VI-8. VFT equation fittings to data for unsulfonated and sulfonated SEBS and sulfonated SEBS filled with iron oxide nanoparticles in the EB glass transition region.	145
VI-9. VFT equation fits to data in the PS block domain glass transition region for unsulfonated, sulfonated and sulfonated SEBS filled with iron oxide.	145
VI-10 (a-b): Merging of β and α transitions near the PS block glass transition region for 16 and 20SEBS/iron oxide.	147

LIST OF TABLES

Table

III-1.	Sample codes for different degrees of sulfonation.	53
III-2.	Interfacial thickness values (d) at different mole % sulfonation.	63
III-3.	Hard and soft block glass transition temperatures.	65
IV-1.	WAXD peak intensity 2θ positions and comparisons with corresponding literature values for bulk cobalt ferrite. First column contains corresponding Miller indices for observed reflections.	76
IV-2.	T_g (tan δ peak temperature) for EB and PS block domains after sulfonation and after subsequent cobalt ferrite incorporation.....	81
V-1.	Bragg spacings and Miller indices for 10SEBS/iron oxide sample... ..	100
V-2.	Glass transition temperatures for the ethylene-butylene and styrene block domains for unmodified SEBS, sulfonated (s) SEBS and sSEBS containing iron oxide.	104
VI-1.	IR absorption band assignments for unsulfonated and sulfonated SEBS samples.	128
VI-2.	VFTH parameters for α transitions in both EB and PS regions for all the samples.	148

CHAPTER I

INTRODUCTION

Electromagnetic wave interference (EMI) is an interesting phenomenon which is a problem in electronics with improper shielding. EMI is also extensively used to alter RADAR signatures in the field of stealth technology. In the case of current electronics, which consists of electrical motors, armatures, and other electrical related circuit boards, there are stray electromagnetic radiations which may be harmful to the consumer on long exposure.

In stealth-related applications, aircraft which fly at very low altitudes need to be invisible to long RADAR waves. This can be achieved by reducing the RADAR cross-section, which needs proper engineering to absorb radiation and sacrifice aerodynamic features to deflect radiation. In application, creating low RADAR cross-section objects without hampering performance is an expensive route. The alternative route, which is more efficient in terms of expense and success, is coating the surface with composite materials capable of absorbing all incident RADAR wave frequencies or absorbing all and emitting different frequencies to cause confusion. In the former method, which makes the entire object invisible but is difficult to achieve; latter method can be successfully done by proper choice of composite materials.

Other applications where electromagnetic radiation needs to be filtered or blocked are in the security and consumer electronic packaging fields. In the case of security applications, important information can be detected from signals leaked from phone lines and/or data storage media with improper coatings. In the case of consumer electronics, for example, cellular phones which commonly work at megahertz (MHz) frequencies,

emit stray EM frequencies (which is why one must turn off a cell phone on aircraft) and cause electromagnetic pollution which may be harmful to humans on long-time exposure.

As an effective alternative to reduce RADAR cross section, rubber-based composite materials were used as radar absorbing materials (RAM) to reduce or weaken EMI in one way.¹ In rubber-based RAMs, rubber serves as a host for electromagnetic (EM) wave absorbing fillers such as carbonyl iron. The advantage of rubber is its softness and flexibility, and it can also be used over a wide temperature range. For higher temperature applications, the fillers should possess higher Curie temperatures and have good stability in the matrix. Fillers with high magnetic permeability serve better in EM wave absorption due to this property. For this reason, carbonyl iron can be used as microwave absorption filler in the 2.6 – 18 GHz range and also above this frequency range and high temperature because of its high Curie temperature value.²⁻⁵ Carbonyl iron can also be used in synthetic rubbers such as ethylene-propylene-diene-monomer (EPDM) due to its excellent resistance towards weathering, aging and chemicals. EPDM is also used with many other types of fillers with particle size lesser than 10 μm and these micron size fillers also provide strength to the matrix.⁶

Even though rubber matrix based RAMs are good EM absorbing materials, they suffer major disadvantages when it comes to high end applications in defense and stealth coatings. Their use is limited in the aforementioned fields due to their bulky nature, and it is hard to disperse the micro-size filler particles to prevent aggregation which makes the coating permeable to the incident RADAR waves. To overcome particle aggregation in the matrix, polymers are suitable in numerous ways: compatible nature, ease of modification, availability in different molecular architectures, ability to form nano-

reactors etc. In the following paragraphs, currently available polymer related matrices and their use in formation of nanocomposite materials are discussed.

Polymer Matrix

Polymers can be electrical insulators, possess flexibility and have good mechanical properties. As such, they can be used as a dispersing medium for conductive fillers to impart good electrical properties. Polymer- ferrite composite materials find applications in insulation and data storage applications.⁷⁻⁹ The dielectric and magnetic properties of this composite depends on the dielectric permittivity¹⁰ and magnetic permeability¹¹ of the individual components as well as particle size, ferrite loading and spatial distribution of the particles. When the ferrite filler exhibits a high conductivity compared to the polymer matrix, the composite system may exhibit particle/matrix interfacial polarization, which is also called the Maxwell-Wagner effect.¹²

By considering the effect of the dielectric contribution of polymer matrix to the resultant polymer composite material, block copolymers with two or more different blocks might not be a bad choice to achieve higher energy dissipation if the difference in dielectric constants of each individual block is large enough to cause the Maxwell-Wagner effect to be great. This effect can be explained as follows: when an alternating current is applied to these block copolymer systems, each block acts as a capacitor due to its dielectric constant and formation of a series of equal numbers of positive (+) and negative (-) charges developed side by side in individual blocks. When a sinusoidal electric field is applied, fluctuating charge can develop at the interfaces due the dielectric permittivity contrast between the different blocks. This dynamic interfacial polarization has a characteristic relaxation time with an energy absorption that dissipates as heat.¹³

This mode of dielectric energy absorption can be used in addition to the magnetic energy dissipation when block copolymers are used as host matrix for the dispersion of magnetic nanoparticles. The important parameter that effects the energy dissipation by dielectric process is the mesophase separated morphology of the block copolymer.

Block Copolymers

Block copolymers are an interesting class of polymer materials due to a variety of properties and ability to form different ordered morphologies. They are formed by covalent linking of two or more dissimilar homopolymers. Diblock copolymers (A-B) and triblock copolymers (A-B-A or B-A-B) can be formed by chemical means, if two homo polymers, A and B which are completely different in chemical and physical properties. Due to their ability to form various structures at molecular level and nanometer order of their radius of gyration, BCPs have become attractive as examples for the past few decades in the field of nanocomposite materials¹⁴ and host material for data storage media. Figure I-1 illustrates a triblock copolymer having hard (PS) and rubbery blocks (IB).

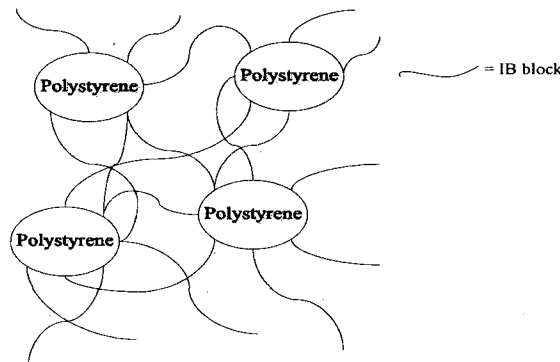


Figure I-1. Schematic representation of PS based triblock copolymers with IB block as rubbery center block.

Due to the dissimilar chemical nature of different blocks, particular phase separated morphologies can form and these can be altered by changing either physical or thermodynamic parameters of the individual blocks or both. In the following paragraphs, more detailed discussion of A-B-A type BCP morphology is discussed which plays a major role in properties of nanocomposites in this dissertation.

Morphology

Microphase separation occurs in block copolymers due to energetic incompatibility between chemically dissimilar blocks. Phase separation occurs when molecular weight crosses a critical value, and its spatial extent is limited due to the connectivity of blocks imposed by the architecture of blocks and as a compromise, different microphase separated phase morphologies occurs in an effort to minimize the area of contact between the different block domains.¹⁵ The length scale of these domains is comparable to the size of block copolymer molecules - typically in the order of tens of nanometers and these morphologies can be altered by changing the volume or weight fraction of A to B and the method of film preparation.¹⁶ Four primary equilibrium architectures as illustrated in Figure I-2 are observed when the volume fraction of the minor phase A to major phase B, f_A , is increased. These morphologies are body-centered-cubic spheres (BCC) ($< \sim 17\%$ A), hexagonally close packed cylinders (HPC) ($\sim 17-28\%$), gyroid (G) ($\sim 28-34\%$), and lamellar (L) ($\sim 34-50\%$).

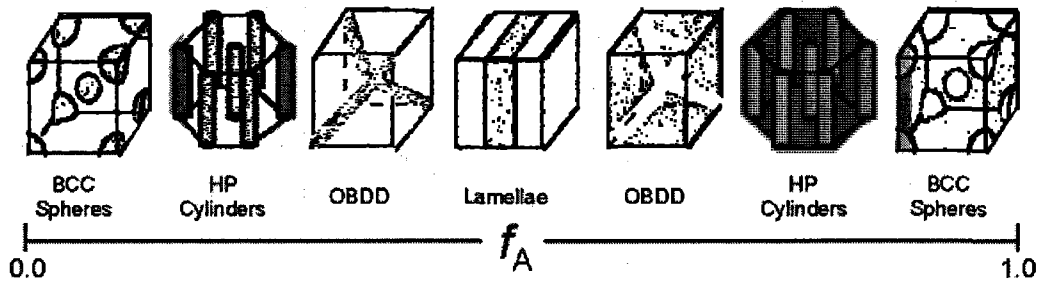


Figure I-2. Range of possible equilibrium morphologies for A-B-A triblock copolymers (reproduced from ref. ²⁹).

In all the above four morphologies, the objects in minor phase A are dispersed in major phase B. When f_A becomes larger than 50 % phase inversion occurs with minor phase B block dispersed in major phase A.^{17,18} The aforementioned morphologies are achieved when all the polymer chains are thermodynamically at their lowest possible energy conditions which can be achieved by proper annealing conditions,¹⁹ choice of solvent,¹⁶⁻¹⁸ solvent evaporation rate.

In addition to f_A , the extent of microphase separation controlled by the Flory-Huggins inter-segmental interaction parameter between blocks A and B (χ_{A-B}), temperature (T), and total degree of polymerization of the block copolymer (N). The thermodynamic entropic and enthalpic contribution of polymer chains for microphase separated morphology is give be the product, $\chi_{A-B}N$.¹⁷ Based on the magnitude of this product, three regimes of BCP phase separation may be assumed when plotting it against volume fraction of block A (f_A). The first regime at very large $\chi_{A-B}N$ values ($\gg 10$) is called as the strong segregation limit (SSL) and phase separation is insensitive to temperature fluctuations and morphology is solely dependant on f_A . In this region, according to Helfland and Wasserman, interfaces between micro domains are narrow

with thickness $\sim a\chi_{A-B}^{1/2}$, where “ a ” is the statistical segment length.²⁰ When, $\chi_{A-B}N$ is decreased (<10) (or T is increased) at a fixed composition f_A , the system reaches the weakly segregated limit (WSL) and interfaces between domains broadens. Above a certain critical temperature called the order-disorder-transition temperature (ODT), the two phases are statistically mixed and the BCP displays rheological behavior consistent with a homogeneous melt. Leibler et al. predicted that near the ODT there exists a transition temperature, where transitions between ordered states take place, e.g., BCC to HCP, called an order-order-transition temperature (OOT).²¹ The third region of phase behavior, where $\chi_{A-B}N$ is between 15 and 60, is called as an intermediate segregation regime. In this regime, unstable phase morphological structures exist, for e.g., gyroid (G), perforated lamellar (PL), and the unstable orthogonally bonded double diamond (OBDD) structures, in addition to the classical BCC, HCP and L structures. These complex phases are mainly unstable due to the restrictions on chain stretching and deviations of the microdomains from the equilibrium curvatures of lowest energy.

Properties

In A-B-A type BCPs, when one block (A) constitutes a hard phase with high glass transition temperature (T_g) (e.g., poly(styrene) (PS), poly (methacrylate), and poly(divinylbenzene)) and the other block (B) comprises a soft rubbery phase with low T_g (e.g., poly(ethylene-co-butylene), poly(isobutylene), and poly(butadiene)), the hard block acts as continuous physical cross-links and provides excellent stability and strength while the soft block offers flexibility and mechanical dampening. The hard block phase serves as a reinforcing filler.²²

Styrene Containing BCPs

Poly (styrene-ethylene-co-butylene-styrene) (SEBS) and poly (styrene-isobutylene-styrene) (SIBS) have been of interest for their stability against thermal-oxidative and UV degradation due to the presence of their saturated soft center blocks. Another advantage of using hydrogenated center blocks is increased χ_{A-B} compared to unsaturated soft blocks, which gives controlled morphological structures, better phase separation and decreased interfacial volume.

One of the main goals of this research with a BCP matrix is to identify or modify an existing BCP matrix that has a moderate to high dielectric contrast between the individual blocks. Mechanical related properties are not considered here. Many research groups studied the dielectric properties of styrene containing BCPs in unmodified and in some cases with the modification of one of the blocks. The styrene blocks in the aforementioned BCPs can be chemically modified by attaching acid groups on the benzene rings. Usually post-sulfonation reaction is considered as an effective method of converting these BCPs into their ionomeric forms.²³ Introduction of sulfonic acid (-SO₃H) groups on styrene blocks of BCPs cause change in morphology²⁴ and also causes property enhancements in mechanical and dielectric properties along with water transport properties.²⁵ In the following paragraphs, brief discussions of properties and morphology of sulfonated SEBS are given for clear understanding of the changes occurring at the molecular level with the introduction of polar groups on one particular block (in this case PS).

Sulfonated (s) poly (styrene-ethylene-co-butylene-styrene) (sSEBS)

Sulfonated forms of poly (styrene-ethylene-co-butylene-styrene) (sSEBS) were extensively studied by Weiss et al. during the early 1990's by investigating their mechanical, rheological, and viscoelastic properties.²⁶ They also reported the morphological transformations using small angle X-ray scattering (SAXS) when the styrene blocks are sulfonated and observed that the inter-domain distances between EB and PS blocks in unsulfonated SEBS are about 22-30 nm. The selective sulfonation of PS blocks leads to the formation of strong $-\text{SO}_3\text{H}-\text{OSO}_2\text{H}$ interactions which are connected to form cross-linking networks when heated. Blackwell et al. studied the presence of sulfonic acid groups on the T_g of the PS blocks before and after the sulfonation and concluded that T_g of the PS block domains increased substantially with increase in sulfonation level without effecting the T_g of EB block.²⁷ These $-\text{SO}_3\text{H}$ groups can be exchanged with various cations to adjust the electrostatic interactions to a degree depending on the counter ion size and valence and whether the counter ion is mineral or organic in nature.²⁸ For example, neutralization of $-\text{SO}_3\text{H}$ groups in SEBS with Zn led to a morphological transition from HPC to L with a long range order whereas neutralization with Na^+ , led to a frustrated morphology. The reason for this is ascribed to a reduction in chain mobility resulting from stronger interactions in the Na-neutralized samples that retards the development of an equilibrium morphology.²⁹⁻³¹

Mauritz *et al.*³² successfully employed sSEBS BCPs as reaction templates for incorporating silica nanoparticles by domain targeted *in-situ* sol-gel reactions of hydrolyzed metal alkoxides in an effort to create novel organic-inorganic nanocomposite materials. The presence of polar groups ($-\text{SO}_3\text{H}$ here) on one of the blocks in a BCP

makes the respective block hydrophilic while the other block is hydrophobic. When films sSEBS are cast under proper annealing conditions for equilibrium morphology, hydrophilic $-\text{SO}_3\text{H}$ groups form clusters which act as nano-reactors. In the current research dissertation, we followed a similar domain targeting *in-situ* process to grow inorganic metal oxide nanoparticles.

Magnetic Nanoparticles

Many researchers studied nanocomposite materials consisting of a polymer matrix in which were dispersed various soft ferrite materials such as cobalt-ferrite (CoFe),³³ nickel zinc-ferrite (NiZnFe),³⁴ and manganese zinc ferrite (MnZnFe)^{35,36} for their magnetic properties at nanosize level and vast temperature ranges. Hard ferrites such as barium ferrites³⁷ and doped/substituted barium ferrites³⁸ were also studied for their huge magneto-crystalline nature, and dielectric and magnetic permeabilities. In the above mentioned ferrites, soft ferrites are more widely used due to their ease to synthesize and are cheaper to produce. Different oxides of iron were also used and were mainly used in colloidal dispersions and medical applications.³⁹ Some of the typical polymer matrices that were used to disperse the pre-prepared nanoparticles were poly(urethane), poly (vinylidene fluoride), (PVDF) and poly (vinyl alcohol) due to their dielectric properties.⁴⁰

Preparation Techniques

Magnetic nanoparticles can be prepared via two routes: top-to-bottom and bottom-up processes. In the top-to-bottom process, bulk magnetic metal oxides are reduced to nanoscale sizes by different techniques, both chemical and physical.^{41,42} In the case of the latter, nanoparticles are grown from their respective ions atom-by-atom followed by

either oxidation or reduction to their respective oxides followed by heating. Nanoparticles that are prepared by top-to-bottom do have excellent control over crystallinity, uniform particle size distribution and thus resultant magnetic properties, but when they are dispersed in polymer matrix, tend to agglomerate or aggregate due to increased surface to volume ratio.⁴³

The bottom-up process can be performed inside or around nano-reactors made of hydrophilic regions in polymers. Typical examples of reaction environments are carboxylate (-COOH), hydroxyl (-OH) and sulfonic acid (-SO₃H) clusters.⁴⁴ Nanoparticles from this route can also be synthesized by a micro-emulsion method, which is very useful in the case of preparing magnetic ferrofluids in medicinal applications such as drug delivery.⁴⁰ Kofina *et al.* successfully employed this bottom-up process to synthesize cobalt ferrite (CoFe₂O₄) nanoparticles in poly [(norbornene)-co-(2-norbornene-5,6-dicarboxylic acid)] block copolymers containing carboxylate (-COOH) nano-reactor clusters at room temperature.

Magnetism Overview

While discussing more about EM properties of complex materials, it is appropriate to discuss the basic concepts of magnetism briefly to facilitate understanding how structure, size and other parameters affect the final properties. Since the discovery of the naturally occurring magnetic material, magnetite, magnetism has been exploited in various disciplines including data storage media, medicine, mining and stealth applications.

Fundamentals of Magnetism

The theory of electromagnetism was developed by Faraday and Maxwell in the 19th century with four equations that connect magnetism and electricity.⁴⁶ It was explained that magnetic fields can be generated electric currents. Matter can be explained at the atomic level in terms of electrons revolving around a nucleus. Each electron possesses spin which generates a magnetic dipole moment (μ_s) as well also an orbital magnetic dipole moment (μ_{orb}). The spin magnetic dipole moment is an intrinsic property of an electron and is related to spin angular momentum (S) by the equation:

$$\mu_s = -\frac{e}{m}S \quad \text{Equation 1}$$

e and m are the charge and mass of an electron, respectively. S is quantized and can only be $\pm \frac{1}{2}$. Electrons generate magnetic moments in only in the z direction of the rotation, so S can be measured as a z component of spin magnetic dipole moment ($\mu_{s,z}$) from the following equation:

$$\mu_{s,z} = \pm \frac{eh}{4\pi m} \quad \text{Equation 2}$$

h is the Plank's constant. The positive value of this equation, know as the Bohr magneton (μ_B), has a value of $9.27 \times 10^{-24} \text{ JT}^{-1}$.⁴⁷ The Bohr magneton is a fundamental unit in magnetism and magnetic materials are described in terms of this quantity. Orbital magnetic dipole moment arises due to the movement of electrons around the nucleus of an atom. The spin magnetic dipole moment and orbital magnetic dipole moment together combine to give the total magnetic properties which determine what type of magnetism a material displays.

Magnetic Domains and Domain Walls

Magnetic materials can be viewed as a collection of connected magnetic domains which are specific locations in which all the magnetic dipoles are oriented in one particular direction. The size of the magnetic domain depends on the final material element size, which can be in its bulk, micro or nano-scopic size. If magnetic dipoles are depicted as arrows which represent the vector sum of all the individual magnetic dipole moments from self spin and rotation of electrons around the nuclei of individual atoms, a magnetic domain is a group of these arrows pointing in one particular direction.

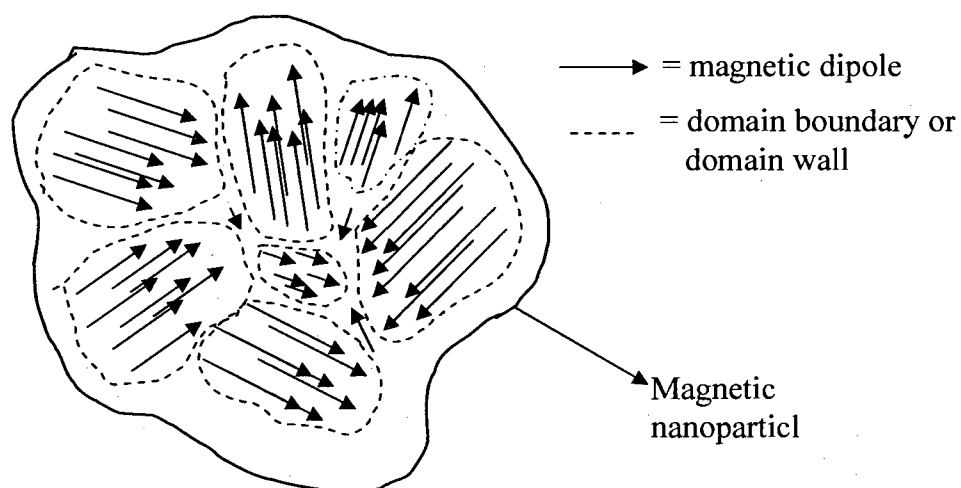


Figure I-3. Schematic representation of magnetic domains separated by magnetic domain walls in a multi-domain magnetic nanoparticle.

In magnetic materials, all magnetic domains will not always point in one direction. Rather, there are groups of adjacent moments in a domain that all point in the same direction but the moments do not point in the same direction over the ensemble of domains but are directed randomly. In the case where the moments are oriented in one direction in a domain, there are boundaries called 'domain walls' between other adjacent

groups of moments pointing in different directions. A schematic representation of magnetic domains separated by domain walls is given in Figure I-3.

Magnetic domains can be originally oriented in a single direction as in the case of strong natural magnets as AlNiCo etc. But if they are not, they can be oriented in any single direction by magnetizing using a strong magnetic field. Magnetic dipole moments that are randomly oriented will result in neutral or negative magnetic dipole moments. In the following paragraphs, different types of magnetism and magnetic materials will be discussed based on the orientations of magnetic dipoles.

Magnetization and Hysteresis

When a magnetic material is magnetized in an external magnetic field, H , inducing a magnetization, M , magnetic moments will orient on the average in the direction of H . The final orientation of all magnetic moments will be, in theory, in the same direction as H , at the saturation field (M_s) which depends on the final size of the crystal and other parameters. When H is reversed the magnetization curve will not retrace itself because magnetic domains are oriented in the previous direction and the expansion of domain walls to facilitate the reorientation of domains leads to an irreversible absorption of energy. When H is zero in the reverse direction the residual magnetization, is called remanence (M_r). On further reversal of H , and until this magnetization becomes zero, the negative intercept of the applied field, called coercivity (H_c), is the magnetic field required to completely demagnetize the material. Beyond this point, if the material further magnetized in the reverse direction, it again attains saturation of magnetic moments but in the opposite direction. A typical hysteresis or M - H curve is shown in

Figure I-4. The area within in the loop represents the energy lost per cycle of applied magnetic field due to the motion of magnetic domains and domain walls.

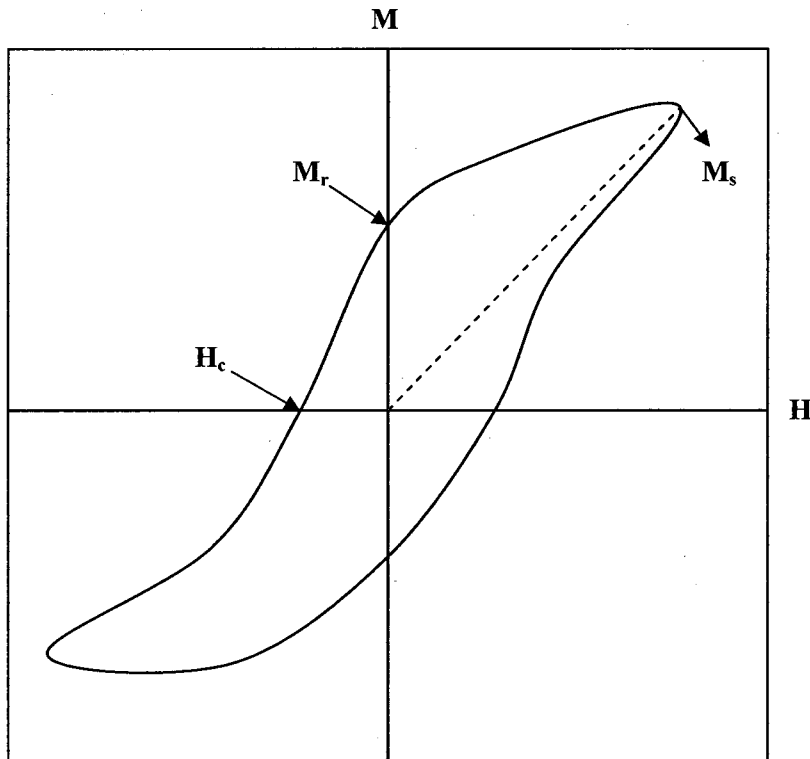


Figure I-4. Typical M-H curve for a magnetic material with hysteresis.

Types of Magnetism and Magnetic Materials

The magnetic nature of a material is governed by the electronic structure of the atoms present in the material. There are six classes of magnetic materials: 1) diamagnetic, 2) paramagnetic, 3) ferromagnetic, 4) antiferromagnetic, 5) ferrimagnetic and 6) superparamagnetic. The most important property of magnetic materials is the magnetic susceptibility (χ) given by:

$$\chi = \frac{M}{H}$$

Equation 3

M is the magnetization affected by H , the applied magnetic field (sometimes also called B), both of which have units of $A\ m^{-1}$. Magnetic susceptibility depends on temperature - except for diamagnetic materials - according to the equation:

$$\chi = \frac{C}{T \pm \theta} \quad \text{Equation 4}$$

C and θ are constants that differ for each material.⁴⁶ θ is called the Curie temperature of a material which is a transition temperature at which a ferromagnetic or ferromagnetic material changes into being diamagnetic.

Diamagnetism

Diamagnetism arises in materials that have fully filled electronic shells and exhibit no net spin moments or orbital moments. Materials that also have partially filled electron shells exhibit other types of magnetic properties that outweigh diamagnetism. Diamagnetic materials have negative susceptibility (χ) values and when placed in magnetic field they turn opposite to the applied field and the resultant magnetization curve consists a straight line passing through the origin with a negative slope. This can be explained in terms of Lenz's law which states that the magnetic field due to the current of electrons opposes the change in the magnetic field which induced the current.⁴⁶ Typical examples for diamagnetic materials are polymers. A hypothetical M-H curve for a diamagnetic material is shown in Figure I-5.

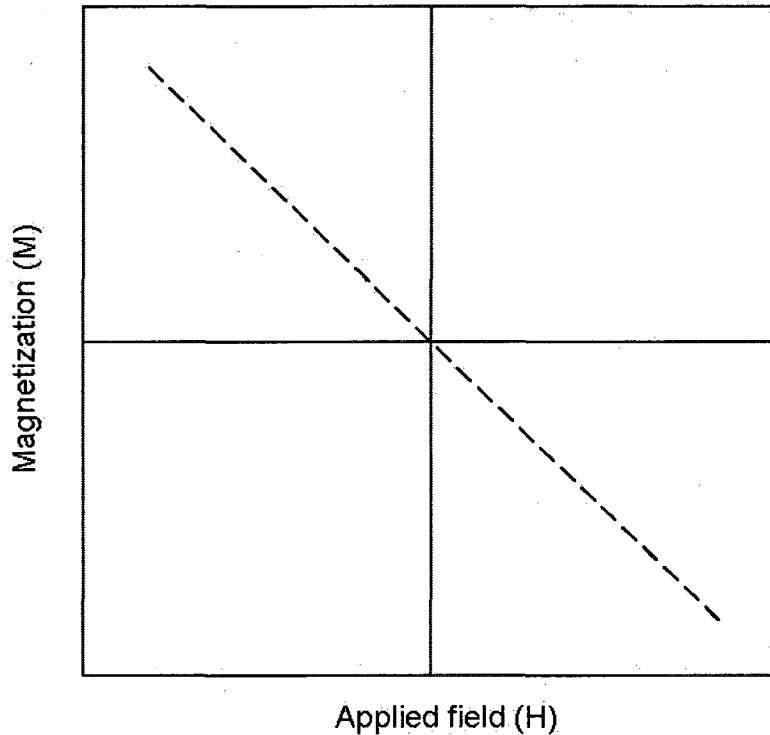


Figure I-5. M-H curve for a diamagnetic material.

Paramagnetism

Paramagnetism occurs in materials having permanent magnetic moments such as atoms or molecules with odd numbers of electrons and atoms or ions with unfilled electron shells.⁴⁸ When these paramagnetic materials placed in zero applied fields, atoms with magnetic dipole moments align in such a way to give zero net moment. However, when exposed to external magnetic fields, a small amount of magnetization occurs due to partial alignment of atoms in the direction of field. The reason for the partial alignment of the moments can be explained by the relationship between χ with T: $\chi = C/T$, the value of C, is expressed by the following equation:

$$\chi = \frac{c\mu_0 Nm^2}{kT}$$

Equation 5

c is a constant, μ_0 is the magnetic permeability of a vacuum, N is number of magnetic dipoles (m) per unit volume, k is the Boltzmann's constant and T is the absolute temperature.⁴⁶ Equation 5 is called the Curie Law and ideal paramagnetic materials obey it at all temperatures except at very low temperatures (< 5 K). The value of kT is the governing factor for the behavior of paramagnetic materials, as it is greater than the energy required to align magnetic dipole moments.⁴⁶ A typical M-H plot of a paramagnetic material is shown in Figure I-6.

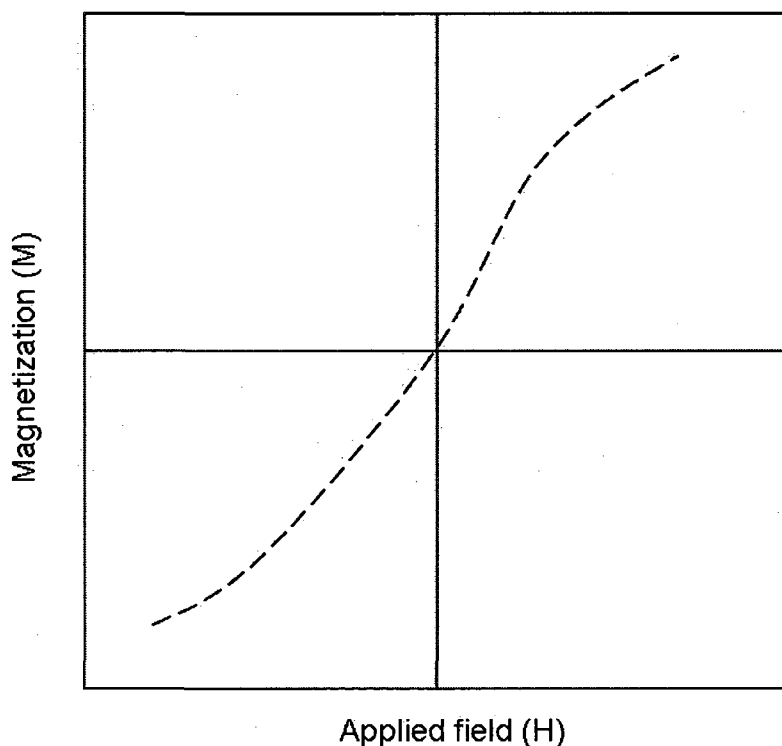


Figure I-6. M vs. H for a paramagnetic material showing no hysteresis.

Ferromagnetism

Ferromagnetic materials differ from weaker diamagnetic and paramagnetic materials in that, in the former, electrons of neighboring atoms interact with each other in a process called exchange coupling.⁴⁶ Exchange coupling is caused by exchange fields

and results in the magnetic dipole moments of atoms being aligned at room temperature despite the effect of thermal randomization, i.e., kT . The most common ferromagnetic materials are zero-valent transition metals such as Fe^0 , Ni^0 , and Co^0 . Ferromagnetism is strongly temperature dependent and the susceptibility of ferromagnetic material is inversely related to temperature by:

$$\chi = \frac{C}{T - \theta} \quad \text{Equation 6}$$

C is a constant and θ is close to the Curie temperature (θ_c) for the material. θ_c is the temperature above which the exchange coupling ceases to exist. So, above θ_c a ferromagnetic material randomizes its electronic structure and moments due to the thermal energy as in a paramagnetic material. The above Equation 6 can be expanded as the Curie-Weiss Law:

$$\chi = \frac{\mu_0 N m^2 c / k}{T - \mu_0 N m^2 c w / k} \quad \text{Equation 7}$$

C is defined by the numerator and θ defined by the fraction in the denominator where w is called the exchange field coefficient.^{46,47} Thus, ferromagnetic materials exhibit highest magnetization values at 0 K and magnetization decreases up to the Curie temperature where it disappears. The Curie-Weiss law explains the higher magnetic susceptibility of ferromagnetic materials, because of the subtraction of θ from T in the denominator. This increased susceptibility enables ferromagnetic materials to saturate at very low magnetic fields, sometimes less than 1 Tesla (T).

Antiferromagnetism

Antiferromagnetic materials consist of sublattices of atoms with magnetic dipole moments aligned antiparallel to each other. Due to this antiparallel alignment, these

materials exhibit very weak magnetic susceptibility values similar to paramagnetic materials. Typical examples of antiferromagnetic materials are transition metal compounds and some transition metal oxides such as CuCl_2 , CoO and NiO . The antiparallel alignment will cease to exist when these materials are heated above a specific temperature called the Neel temperature (θ_N). Above θ_N , antiferromagnetic materials have some positive susceptibility values compared to paramagnetic materials. Below θ_N , antiferromagnetic materials have a spontaneous magnetization ($H=0$) that causes the magnetic moments of the sublattices align antiparallel to each other. Magnetic moment alignments for a) paramagnetic, b) ferromagnetic, c) antiferromagnetic and d) ferrimagnetic materials are displayed in Figure I-7.

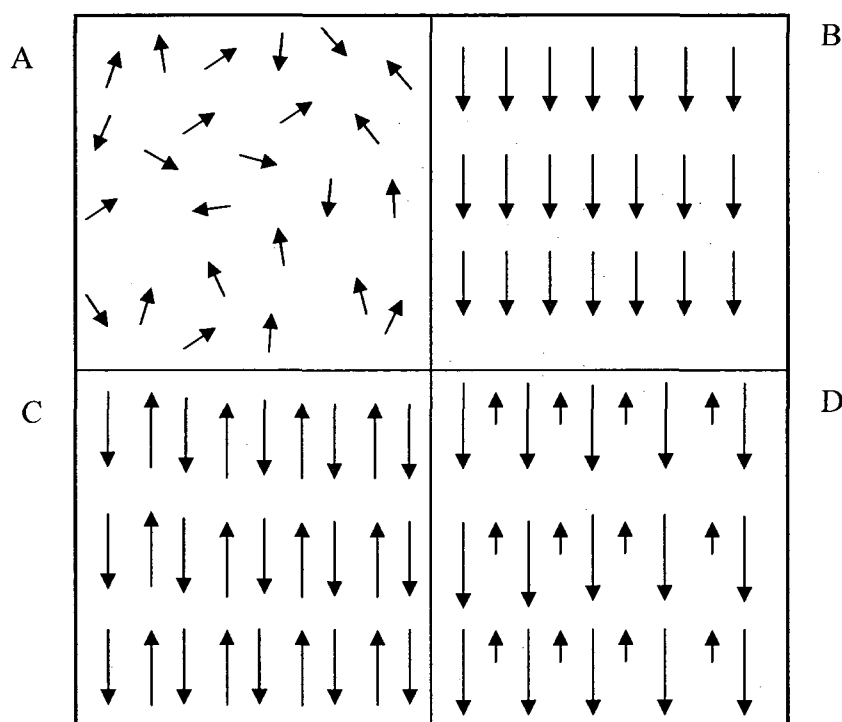


Figure I-7. Alignment of magnetic moments in zero applied magnetic fields at room temperature for A) paramagnetic or superparamagnetic, B) ferromagnetic, C) antiferromagnetic and D) ferrimagnetic materials.

Ferrimagnetism

Ferrimagnetic materials exhibit substantial spontaneous magnetization at room temperature just like ferromagnetic materials. Again, as for ferromagnetic materials, they consist of self-saturated magnetic domains, and exhibit the phenomena of magnetic saturation and hysteresis. Their spontaneous magnetization disappears above the Curie temperature and they become paramagnetic. The magnetic dipole moments in a ferrimagnetic material are divided into sublattices and are classified as a subset of antiferromagnetic materials. Each sublattice can be treated as a ferromagnetic material where the difference between the magnetic dipole moments for the sublattices results in net magnetization for the ferrimagnetic material.⁴⁹ The difference between ferri- and antiferromagnetic materials is that either the magnitude or number of the moments of the sublattices is different.⁴⁶ Most important ferrimagnetic substances are certain double oxides of iron and other metals, called ferrites. Magnetic ferrites fall mainly into three groups with different crystalline structures: cubic, inverse spinel and hexagonal.

Both cubic and inverse spinel structures have the general formula $AO \cdot B_2O_3$ where M is a divalent metal ion, like Mn, Ni, Co, Fe, Mg. In case of inverse spinel structure, A^{2+} atoms occupy half of the octahedral coordination sites and the other half are occupied by the half of B^{3+} atoms. The remaining half of B^{3+} atoms occupies all of the tetrahedral coordination sites. For hexagonal crystalline materials, barium ferrite $BaO \cdot (Fe_2O_3)_6$ is a good example. A schematic of these three crystalline structures are shown Figure I-8.

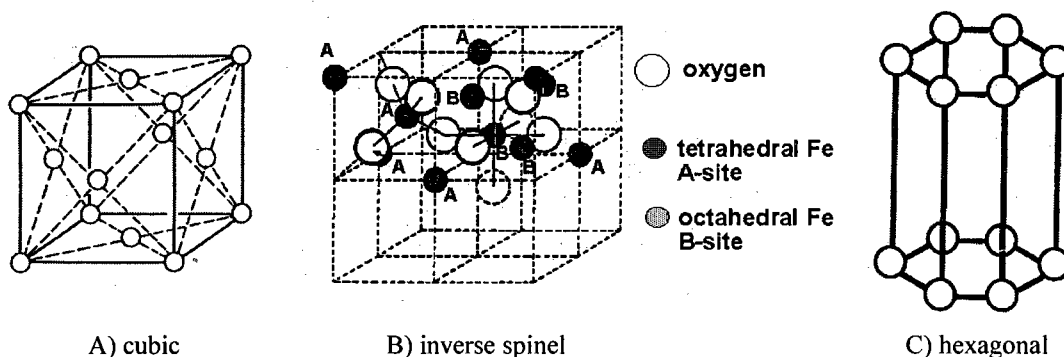


Figure I-8. Three crystalline structures A) cubic, B) inverse spinel, and C) hexagonal structures exhibited by most of the ferrimagnetic/ferromagnetic materials.

Superparamagnetism

When a macroscopic sample is magnetized the free energy is minimized by aligning the magnetic moments in the direction of applied field. By shrinking the magnetic particle size to critical diameter D_c and below, formation of magnetic domains is not energetically favored. This critical diameter D_c is determined by the value of magnetic saturation (M_s), and the exchange constant A of that material⁵⁰ by equation 8:

$$D_c \approx \frac{k_0}{M_s} \sqrt{\frac{A}{\mu_0}} \quad \text{Equation 8}$$

μ_0 is the magnetic permeability of vacuum and k_0 is a constant of the order of 10^1 . For most magnetic particles the critical diameter for single domain ranges from 10 to 100 nm.⁴⁹ The single domain (SD) sizes for spherical particles of iron, cobalt, nickel, manganese, and maghemite are 14, 70, 55, 128, and 166 nm, respectively.⁵² For cobalt ferrite it is ~ 40 nm⁵³ and for cobalt iron oxide it is 14 nm.⁵⁴

When particle size is further decreased, there is another critical size, below which it becomes superparamagnetic as both M_r and H_c go to zero and the M-H curve exhibits no hysteresis with the magnetization-demagnetization process.

Superparamagnetic materials behave like ferromagnetic or ferrimagnetic materials below a temperature called the blocking temperature (T_B) which is similar to the Curie temperature for ferromagnetic materials. Above T_B , superparamagnetic materials behave like paramagnetic materials displaying no hysteresis.⁵⁵ As discussed, superparamagnetism is related to particle size and temperature, and the particle size depends on T_B by the following equation:⁵⁶⁻⁵⁸

$$T_B = \frac{KV}{25k_B} \quad \text{Equation 9}$$

K is the anisotropy constant for the material and V is the particle volume. Below T_B the magnetic moments of the particles are fixed (their approach to thermodynamic equilibrium is blocked). Above T_B , the magnetic moments acquire thermal energy due to the kinetic vibrations and are free to align randomly in the absence of an external field. A depiction of shrinking of particle size with coercive field is in Figure I-9.

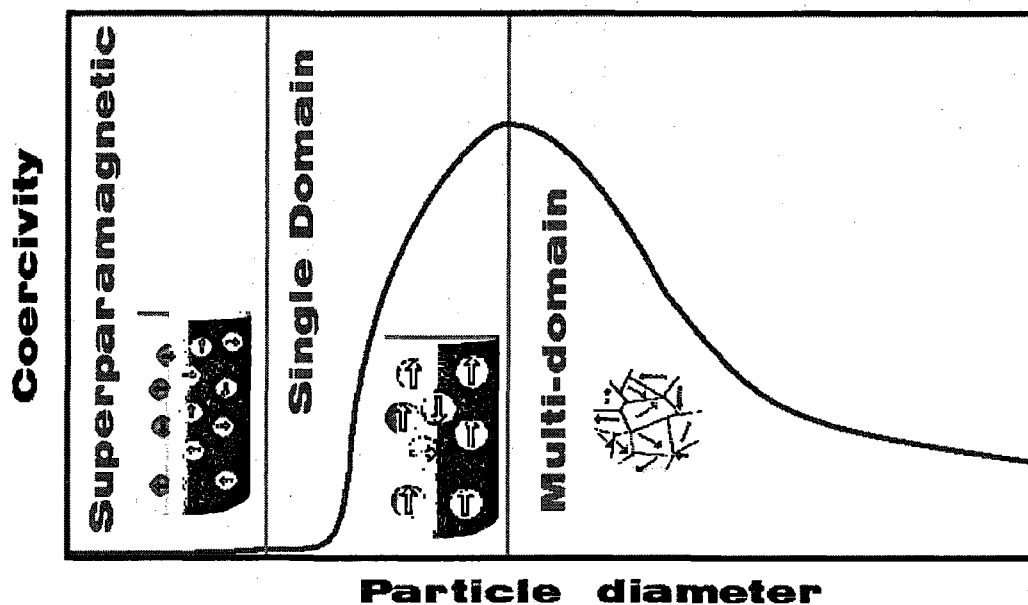


Figure I-9. Depiction of magnetic domain nature from multi-domain to superparamagnetic with decreasing the particle diameter and its effect on coercivity (adapted from ref. ⁵⁹).

Magnetic Anisotropy

Before concluding this chapter it is relevant to introduce an important parameter that governs magnetism in materials, namely, magnetic anisotropy. This property originates from sample shape, crystal symmetry, and stress or directed atomic pair ordering. Of these parameters, crystal symmetry is more important in the case of magnetic metal oxides exhibiting different crystalline structures. The ease of magnetization depends on the anisotropy of the crystalline structure that the metal oxide that is found in nature. For instance, magnetic anisotropy in single crystals of Fe, Ni and Co depends entirely on the crystalline structure that exists. The ease of magnetization depends on the atoms that are aligned along the *easy* axis. 'Easy axis' is a column, row or a diagonal axis of atoms in a crystal consisting of a less number of atoms when compared to the hard axis. A hard axis is one which consists of more number of atoms aligned and

thus it requires more energy to magnetize. Figure I-10 shows three different crystalline atoms, viz, body centered cubic (*bcc*) Fe, face centered cubic (*fcc*) Ni, and a hexagonally close packed (*hcp*) Co. From the figure, the magnetization process for *bcc* Fe in the *easy* axis $\langle 100 \rangle$ is easier to reach saturation rather than magnetizing to saturation along the *hard* axis $\langle 111 \rangle$. For *fcc* Ni, and *hcp* Co the easy axes are $\langle 111 \rangle$ and $\langle 0001 \rangle$, respectively.

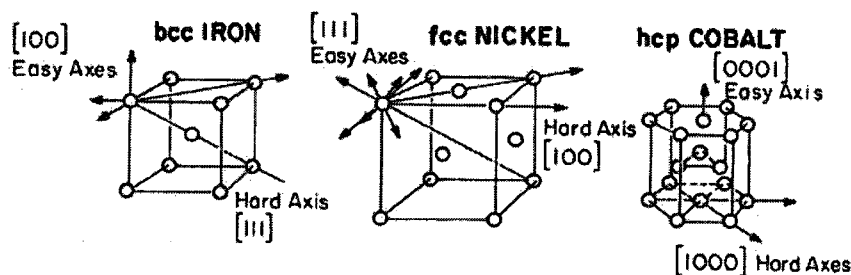


Figure I-10. Depiction of easy and hard axes of magnetization in *bcc* Fe, *fcc* Ni and *hcp* Co (adapted from ref.⁵⁷).

In-situ Precipitation Method

Conventional addition of preformed nanoparticles to a polymer matrix causes agglomeration due to high surface-to-volume ratio. To prevent aggregation and enhance dispersion, growth at selective domains, and control of particle size, *in-situ* precipitation offers an option to incorporate nanoparticles by a bottom-up process where nanoparticles are grown from their precursor salts by an atom by atom.

Lopez *et al.* used a sulfonated PS matrix to grow cobalt ferrite (CoFe_2O_4) nanoparticles from their respective metal chlorides in an aqueous solution at room temperature. The nanoparticles thus grown in the sPS matrix were crystalline and exhibited other physical properties like magnetism as they would have in bulk⁴⁰ Kofinas *et al.* synthesized CoFe_2O_4 nanoparticles in poly [(norbornene)-co-(2-norbornene-5,6-

dicarboxylic acid)] (NOR/NORCOOH) block copolymers *via* an *in-situ* precipitation method. Nanoparticles of size 3-6 nm formed and were well distributed in the matrix.⁶⁰ A schematic representation of the *in-situ* precipitation process is shown in Figure I-11.

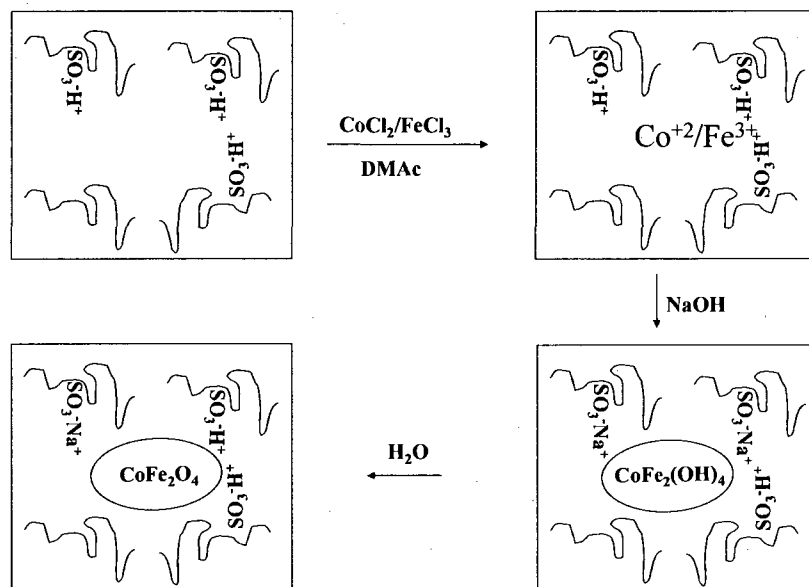


Figure I-11. Depiction of *in-situ* precipitation of CoFe_2O_4 nanoparticles in SPS domains (adapted from ref.⁵⁹).

Guru *et al.*⁴⁴ synthesized CoFe_2O_4 nanoparticles in an sSEBS matrix *via* this process and studied the *magnetic* behavior of these composites at room and sub-zero temperatures. This work of this dissertation starts from that of Guru *et al.* The study of the magnetic nature of incorporated nanoparticles and also the dielectric properties sSEBS/metal oxide nanocomposites was conducted.

Dielectric Relaxation Spectroscopy

The study of materials in alternating electric fields based on the dynamic behavior of dipoles can be accomplished using dielectric relaxation spectroscopy. Orientation of

dipoles takes place towards the direction of applied electric fields. These motions of dipoles as attached to polymer chains are termed 'relaxations'. There are different types of electrical polarization due to charge motions that occur in polymers and they are electronic, atomic, ionic, dipolar, and interfacial/space charge polarizations. The technique uses sinusoidal voltage impressed over a sample over a specific frequency range and this is referred to as broadband dielectric spectroscopy (BDS). In the following discussion, polarization mechanisms under static fields are given for its easiness to understand.

Static Polarization

The force between two electric charges in a dielectric medium is governed by Coulomb's Law:

$$F_C = \frac{1}{4\pi\epsilon_s} \frac{q_1 q_2}{r^2} \quad \text{Equation 10}$$

F_C is the force between two charges q_1 and q_2 that are separated by distance r . ϵ_s is the static permittivity of the dielectric material. The electric field, E , at charge q_1 is F_C/q_1 . As the permittivity increases the electric field decreases.

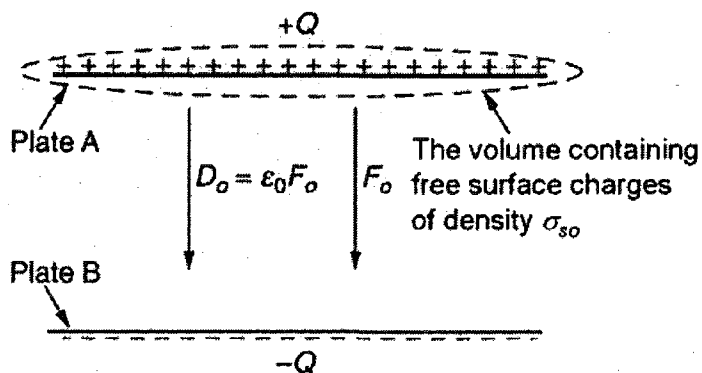


Figure I-12. Depiction of electric field between two parallel plate electrodes of equal and opposite charges Q with vacuum in between (adapted from ref.⁶¹).

Now consider two electric plates equal and oppositely charged and separated by as distance d , as in Figure I-12.

The vacuum permittivity is given by the following equation:

$$\epsilon_0 = \frac{D_0}{E_0} \quad \text{Equation 11}$$

D_0 is the electric flux density and E_0 is the electric field strength in vacuum. According to Gauss's law, an equal number of positive and negative charges are on the plates.⁶¹ Due to these charge separation on electric plates, a potential difference V is generated as illustrated in Figure I-13.

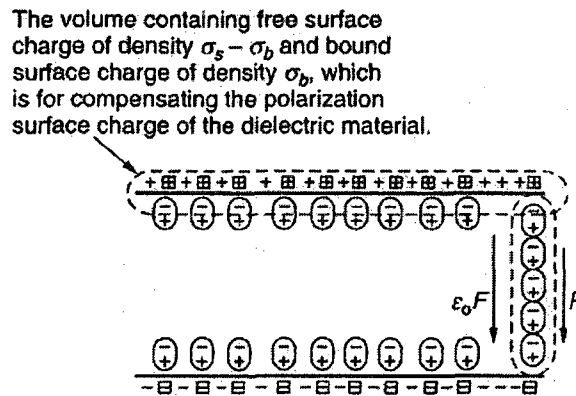


Figure I-13. Unbalanced electric charges at the interfaces between a dielectric and electrodes on application of electric field (adapted from ref.⁶¹).

Q is directly proportional to V by a constant, C which is the capacitance. The relationship between Q and V can also be given by the surface charge density σ_s , which is the total charge per unit area.

$$Q = C(Ed) = \sigma_s A \quad \text{Equation 12}$$

Where d is the distance between the two oppositely charged plates and from this equation permittivity of vacuum can be derived from the following equation:

$$C_0 = \frac{Q}{V} = \frac{\sigma_s A}{Ed} = \epsilon_0 \frac{A}{d} \quad \text{Equation 13}$$

It is easy to calculate C_0 and ϵ_0 by knowing applied field strength, the distance between and area of the plates, and measuring the resultant field strength E . When a dielectric material is introduced between the same electric plates, the system adjusts itself to accommodate the applied field and charge separation occur across the sample at the interfaces between the material and electrodes as shown in the Figure I-13.

With the presence of dielectric material, a portion of the surface charge density σ_s is used to polarize the dielectric material surface to the extent of σ_b and the remainder of it is still under the prior vacuum conditions ($\sigma_s - \sigma_b$) creating an electric flux density D , as shown in following equations:

$$D = \epsilon_0 E \quad \text{Equation 14}$$

Therefore,

$$\begin{aligned} \sigma_s &= (\sigma_s - \sigma_b) + \sigma_b \\ &= D = D_0 + P \\ &= \epsilon_s E = \epsilon_0 E + (\epsilon_s - \epsilon_0)E \end{aligned} \quad \text{Equation 15}$$

Where polarization is expressed as

$$P = (\epsilon_s - \epsilon_0)E = \sigma_b = \textit{polarization} \quad \text{Equation 16}$$

From equation 16, the static permittivity ϵ_s of the dielectric material can be used to calculate the relative static permittivity ϵ_{sr} according to the following equation

$$\epsilon_{sr} = \frac{\epsilon_s}{\epsilon_0} \quad \text{Equation 17}$$

Thus, for any dielectric material, the relative dielectric permittivity can be determined experimentally by applying a static electric field. This value is independent of electric

field strength at low electric fields. ϵ_{sr} is a function of chemical structure, material imperfections and physical parameters such as temperature and pressure.

Dynamic Polarization

When a dielectric is placed in a fluctuating electric field, ϵ_{sr} depends on the frequency of the applied voltage. Dipoles that interact with the field do not respond instantaneously but are time dependent, which is why the frequency of applied field is important. If the frequency is so high that the period of oscillation is much greater than the natural time scale of the material polarization, polarization will not be observed.

Figure I-14 illustrates characteristic (t) time scales of different polarizations in materials.

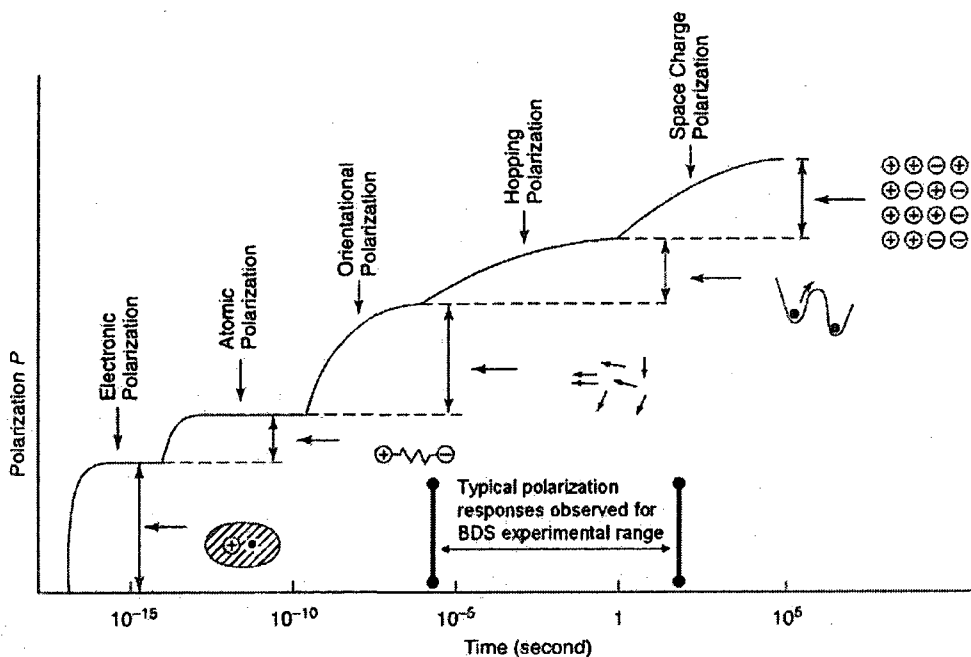


Figure I-14. Types of polarization mechanisms at different times scales of measurement. Typical BDS test window of 10^{-6} to 10^2 sec also shown (adapted from ref. ⁶¹).

From Figure I-14, it can be observed that the larger the entity or longer the motional scale, the greater the corresponding polarization time.

At a time scale of 10^{-10} sec only atomic and electronic polarizations are observed. For polarization involving larger structures the time response is sluggish due to difficult charge rearrangements. If the applied frequency is 100 Hz the response of the system must occur within $\frac{1}{2} \times 10^{-2}$ sec. At this time scale, electronic, atomic, orientational, and hopping polarization mechanisms can be observed whereas space charge polarization is not observed as its time scale is longer than the experimental time scale as shown in Figure I-14.

Due to the constraints of scale of different polarization processes and frequency limitations in a BDS instrument, designing an experiment is important to sample polarizations that are fingerprints of molecular motions. For example, a frequency range of 10^2 to 10^6 Hz in BDS experiment corresponds to a time scale of 100 to 10^{-6} sec. In this time scale, only atomic and electronic polarizations and their related molecular motions observed as they respond ($<10^{-10}$ sec) much faster than the applied frequency and indicated in Figure I-14. As these two polarization which can be perceived in the time window because of their time scale can be picturized as a spring in a mechanical testing, where as other polarizations, which are much slower and hard to perceive by the instrument in this time scale can be behave as a dashpot in the same material. As a result, these polarizations can be viewed as viscoelastic material with both storage and loss modulus, designated as P_1 and P_2 respectively. In other words, the dipoles, which can not respond to the applied electric field experience some energetic loss, termed as dielectric loss. Thus, the polarization responses are complex P^* , which have storage P' and loss component P'' as shown in Equation 18:

$$P^* = P' - jP''$$

Equation 18

Following the above equation, complex permittivity ϵ^* is expressed in terms as their corresponding storage ϵ' and loss ϵ'' permittivities by the following equation:

$$\epsilon^* = \epsilon' - i\epsilon'' \quad \text{Equation 19}$$

And the loss tangent for both the above equations is written as:

$$\tan \delta = \frac{P''}{P'} = \frac{\epsilon''}{\epsilon'} \quad \text{Equation 20}$$

The storage and loss permittivity responses for an applied sinusoidal voltage are shown in Figure I-15.

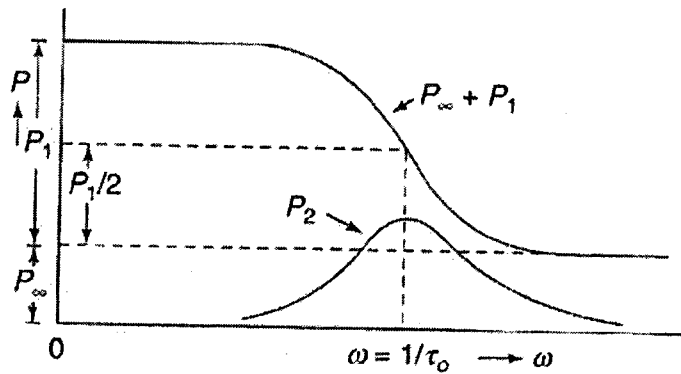


Figure I-15. A schematic representation of complex polarization $P^* (= P_\infty + P_1 + P_2)$ as a function of angular frequency ($\omega = 2\pi f$). $P_\infty + P_1$ contains the storage component P_1 and the loss component P_2 (adapted from ref. ⁶¹).

In Figure I-15, P_∞ and P_1 comprise the storage and it decreases stepwise with increasing angular frequency. The loss polarization, identified as P_2 , is a curve with a peak. P_∞ component of the storage polarization is identified as the instantaneous storage response of electronic/atomic polarization. It characteristically exhibits a flat line, which is present at all tested frequencies but becomes more apparent at higher frequencies in the absence of P_1 and P_2 . Additionally there is no detectable loss polarization is observed in this region. Usually P_1 component is in phase with relaxation process as it the storage

component and P_2 , which is the loss component of the polarization, is out of response with the relaxation process. The frequency at peak max for curve P_2 occurs gives the time scale at which maximum energy loss due to polarization is occurring. The concept of BDS data analysis and techniques are given in chapter 6 due to its relevance.

Dynamic Magnetic Relaxation

As described earlier, in cases of a multi-domain magnetic nano- or macro- sized materials, the magnetic moments in domains are surrounded by domain walls. When these materials are subjected to a single cycle of magnetic field (usually a quasi-static) variance, they may exhibit magnetic hysteresis loops due to energy loss. Energy lost is due to orientation of magnetic domains in by the applied field and domain wall expansion and contraction. When the same magnetic material is place in an alternating magnetic field, magnetic domains change their direction from positive to negative directions where the process depends on the frequency of the applied field. Domains which lag behind the applied field relax slowly and there is a loss of the magnetic energy. So, for each cycle of applied alternating magnetic field with a frequency ω , the complex permeability (μ^*) is given by Equation 21:

$$\mu^* = \mu' + i\mu'' \quad \text{Equation 21}$$

μ' and μ'' are the magnetic storage and loss magnetic permeabilites, and $i = \sqrt{-1}$.

Magnetic moments relax and their detection depends on the frequency of the applied magnetic field. As in dielectric spectroscopy, there are energy loss peaks corresponding to a frequency $\omega_{\max} = 2\pi f_{\max}$ as shown in following Figure I-16.

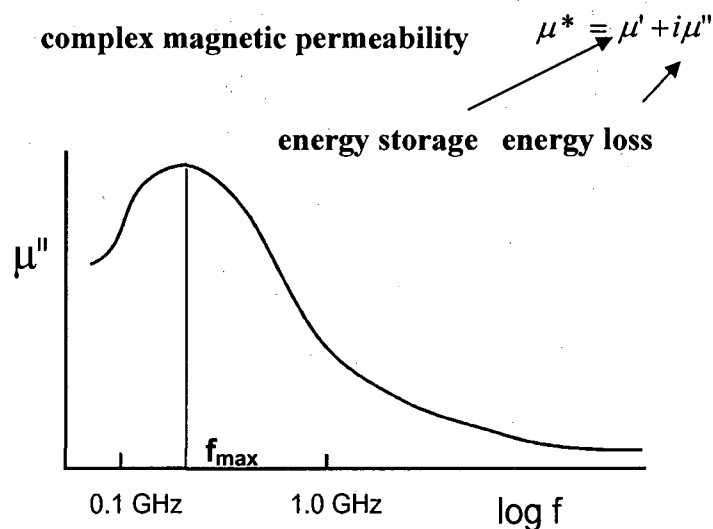


Figure I-16. Hypothetical magnetic loss permeability μ'' as a function of frequency by, f .

Conclusions

Motivated by increased concern about electromagnetic wave interrogative radiation in defense applications and the shielding of components from stray or intrusive radiation in consumer electronics applications, block copolymer/magnetic metal nanocomposites were studied. The effect of morphology the effect of attached sulfonic acid groups, on magnetic properties imparted by in-situ synthesized magnetic metal oxide nanoparticles was explored.

And, the dielectric behavior of sSEBS/magnetic metal oxide nanocomposites was investigated at different frequencies and temperatures.

The primary goal of this research was to understand the effect of morphology and effect of sulfonation in the SEBS BCP matrix on the magnetic particle growth, particle dispersion, and the magnetic and dielectric properties. Two types of magnetic metal oxide nanoparticles were synthesized: CoFe_2O_4 and $\alpha\text{-Fe}_2\text{O}_3$ in sulfonated domains of SEBS BCP and their electrical and magnetic properties were studied at different temperatures.

Chapter II describes advanced characterization techniques that were used to measure magnetic properties at room and sub-zero temperatures and the crystalline nature of nanoparticles dispersed in sSEBS matrices. Chapter III reports an investigation of PS block sulfonation on the interfacial thickness and equilibrium morphology of the sSEBS matrix and evolution of morphology from HPC to lamellar to frustrated morphology with increase in mole % of sulfonation. The effect of morphology on magnetic properties of CoFe_2O_4 and $\alpha\text{-Fe}_2\text{O}_3$ nanoparticles grown in selective sPS domains of SEBS block is discussed in Chapters IV and V and Chapter VI describes the dielectric properties of sSEBS/ $\alpha\text{-Fe}_2\text{O}_3$ nanocomposites and the effect of nanoparticles on the relaxation behavior in the PS block domain regions.

References

- (1) Feng, Y. B.; Qiu, T.; Shen, C. Y.; Li, X. Y. *IEEE Transactions on Magnetics* **2006**, 42, 363.
- (2) Deng, L. J.; Xie, J. L.; Liang, D. F.; Guo, B. J. *Journal Functional Materials* **1999**,30,118.
- (3) Liu, A. X.; Ru, M. Y.; Meng, F. J.; Zhang, W. X.; Zhang, Q. Z.; Zhou. Q. F. *Acta Polymerica Sinica*, **2003**, 5, 757.
- (4) Pinho, M. S.; Gregori, M. L.; Nunes, R. C. R.; Soares, B. G. *Polymer Degradation and Stability* **2001**, 73, 1.
- (5) W. Yong, M. N. Afsat, and R. Grignon. *IEEE Antennas and Propagation Society* **2003**, 4, 619.
- (6) Feng, Y.B.; Qiu, T.; Zhang, J. *Aerospace Material Technology* **2005**,35, 37.
- (7) Dormann, J. L.; Fiorani, D.; Editors, *Magnetic Properties of Fine Particles. Proceedings of the International Workshop on Studies of Magnetic Properties of Fine Particles and Their Relevance to Materials Science, Rome, Italy, November 4-8, 1991. 1992*; p 430 pp.
- (8) Popplewell, J.; Sakhnini, L. *Journal of Magnetism and Magnetic Materials* **1995**, 149, 72.
- (9) Raj, K.; Moskowitz, B.; Casciari, R. *Journal of Magnetism and Magnetic Materials* **1995**, 149, 174.
- (10) Wang, J. W.; Shen, Q. D.; Yang, C. Z.; Zhang, Q. M. *Macromolecules* **2004**, 37, 2294.
- (11) Kodama, R. H. *Journal of Magnetism and Magnetic Materials* **1999**, 200, 359.

- (12) Wagner, K. W. *Berlin Physikalische Gesellschaft* **1913**, 45-6.
- (13) Narkis, M.; Ram, A.; Stein, Z. *Polymer Engineering and Science* **1981**, 21, 1049.
- (14) deGennes, P. G. *Scaling Concepts In Polymer Physics*; Cornell University Press: New York, 1979.
- (15) Thomas, E. L.; Lescanec, R. L. *Philosophical Transactions of the Royal Society of London Series A-Mathematical Physical and Engineering Sciences* **1994**, 348, 149.
- (16) Noshay, A.; McGrath, J.E. *Block Copolymers: Overview and Critical Survey*; Academic Press: New York, 1997.
- (17) Bates, F. S.; Fredrickson, G. H. *Annual Review of Physical Chemistry* **1990**, 41, 525.
- (18) Hajduk, D. A.; Harper, P. E.; Gruner, S. M.; Honeker, C. C.; Kim, G.; Thomas, E. L.; Fetters, L. J. *Macromolecules* **1994**, 27, 4063.
- (19) Register, R. A.; Prud'homme, R. K. *In Ionomers: Synthesis, structure, Properties, and Applications*; Tant, M. R.; Mauritz, K. A.; Wilkes, G. L., Eds.; Chapman & Hill: New York, 1997.
- (20) Helfland, E.; Wesserman, Z. *In development in Block Copolymers*; Goodman, I. Applied Science: New York, 1982; vol 1.
- (21) Leibler, L. *Macromolecules* **1980**, 13, 1602.
- (22) Holden, G. *Understanding Thermoplastic Elastomers*; Hanser Publishers: Munich, 2000; p 150 pp.
- (23) Mauritz, K. A.; Storey, R. F.; Mountz, D. A.; Reuschle, D. A. *Polymer* **2002**, 43, 4315.
- (24) Mauritz, K. A.; Blackwell, R. I.; Beyer, F. L. *Polymer* **2004**, 45, 3001.

- (25) Elabd, Y. A.; Napadensky, E. *Polymer* **2004**, 45, 3037.
- (26) Weiss, R. A.; Sen, A.; Pottick, L. A.; Willis, C. L. *Polymer Communications* **1990**, 31, 220.
- (27) Blackwell, R. I.; Mauritz, K. A. *Polymer* **2004**, 45, 3457.
- (28) Weiss, R. A.; Sen, A.; Pottick, L. A.; Willis, C. L. *Polymer* **1991**, 32, 2785.
- (29) Weiss, R. A.; Sen, A.; Willis, C. L.; Pottick, L. A. *Polymer* **1991**, 32, 1867.
- (30) Lu, X.; Steckle, W. P.; Weiss, R. A. *Macromolecules* **1993**, 26, 5876.
- (31) Lu, X.; Steckle, W. P.; Weiss, R. A. *Macromolecules* **1993**, 26, 6525.
- (32) Blackwell, R. I.; Mauritz, K. A. *Polymers for Advanced Technologies* **2005**, 16, 212.
- (33) Vaishnav, P. P.; Senaratne, U.; Buc, E.; Naik, R.; Naik, V. M.; Tsoi, G.; Wenger, L. E.; Boolchand, P. *Journal of Applied Physics* **2006**, 99, (8G702).
- (34) Nakamura, T.; Tsutaoka, T.; Hatakeyama, K. *Journal of Magnetism and Magnetic Materials* **1994**, 138, 319.
- (35) Yavuz, O.; Ram, M. K.; Aldissi, M.; Poddar, P.; Hariharan, S. *Journal of Materials Chemistry* **2005**, 15, 810.
- (36) Kazantseva, N. E.; Bespyatykh, Y. I.; Sapurina, I.; Stejskal, J.; Vilcakova, J.; Saha, P. *Journal of Magnetism and Magnetic Materials* **2006**, 301, 155.
- (37) Li, B. W.; Shen, Y.; Yue, Z. X.; Nan, C. W. *Journal of Magnetism and Magnetic Materials* **2007**, 313, 322.
- (38) Ghasemi, A.; Hossienpour, A.; Morisako, A.; Saatchi, A.; Salehi, M. *Journal of Magnetism and Magnetic Materials* **2006**, 302, 429.

- (39) Hussain, S.; Youngs, I. J.; Ford, I. J. *Journal of Physics D-Applied Physics* **2007**, 40, 5331.
- (40) Lopez, D.; Cendoya, I.; Torres, F.; Tejada, J.; Mijangos, C. *Journal of Applied Polymer Science* **2001**, 82, 3215.
- (41) Lee, J.-G.; Park, J. Y.; Oh, Y.-J.; Kim, C. S. *Journal of Applied Physics* **1998**, 84, 2801.
- (42) Okuno, S. N.; Hashimoto, S.; Inomata, K. *Journal of Applied Physics* **1992**, 71, 5926.
- (43) Ziolo, R. F.; Giannelis, E. P.; Weinstein, B. A.; O'Horo, M. P.; Ganguly, B. N.; Mehrotra, V.; Russell, M. W.; Huffman, D. R. *Science (Washington, DC, United States)* **1992**, 257, 219.
- (44) Rajan, G. S.; Mauritz, K. A.; Stromeyer, S. L.; Kwee, T.; Man, P.; Weston, J. L.; Nikles, D. E.; Shamsuzzoha, M. *Journal of Polymer Science Part B-Polymer Physics* **2005**, 43, 1475.
- (45) Ahmed, S. R.; Kofinas, P. *Macromolecules* **2002**, 35, 3338.
- (46) Halliday, D.; Resnick, R.; Walker, J. *Fundamentals of Physics: Extended*, 5th Ed., John Wiley & Sons, Inc., New York, 1997.
- (47) Jakubovics, J. P. *Magnetism and Magnetic Materials*, 2nd Ed., 1994; p 165 pp.
- (48) Kittel, C. *Introduction to Solid State Physics. Vol. 1. 6th Ed.*, 1988; p 346 pp.
- (49) Craik, D. *Magnetism: Principles and Applications*; John Wiley & Sons, Inc., New York, 1995.
- (50) Kodama, R. H. *Journal of Magnetism and Magnetic Materials* **1999**, 200, 359.
- (51) Skomoski, R.; Liu, J. P.; Sellmeyer, D. J. *Physical Review B* **1999**, 60, 7359.

- (52) Klabunde, K. J.; Editor, *Nanoscale Materials in Chemistry*. 2001; p 292 pp.
- (53) Chinnasamy, C. N.; Jeyadevan, B.; Shinoda, K.; Tohji, K.; Djayaprawira, D. J.; Takahashi, M.; Joseyphus, R. J.; Narayanasamy, A. *Applied Physics Letters* **2003**, *83*, 2862.
- (54) Hoh, J. C.; Yaacob, I. I. *Journal of Materials Research* **2002**, *17*, 3105.
- (55) Leslie-Pelecky, D. L.; Rieke, R. D. *Chemistry of Materials* **1996**, *8*, 1770.
- (56) Chikazumi, S. *Physics of Magnetism*; John Wiley: New York, 1964.
- (57) Cullity, B. D. *Introduction to Magnetic Materials*; Addison-Wesley Series: 1972; p 666 pp.
- (58) O'Handley, R. C. *Modern Magnetic Materials: Principles and Applications*. 1999; p 704 pp.
- (59) Chipara, M.; Hui, D.; Sankar, J.; Leslie-Pelecky, D.; Bender, A.; Yue, L.; Skomski, R.; Sellmyer, D. J. *Composites, Part B: Engineering* **2004**, *35B*, 235.
- (60) Ahmed, S. R.; Ogale, S. B.; Papaefthymiou, G. C.; Ramesh, R.; Kofinas, P. *Applied Physics Letters* **2002**, *80*, 1616.
- (61) Kao, K.C.; *Dielectric Phenomena in Solids*; Elsevier Academic Press: New York, 2004.

CHAPTER II

EXPERIMENTAL

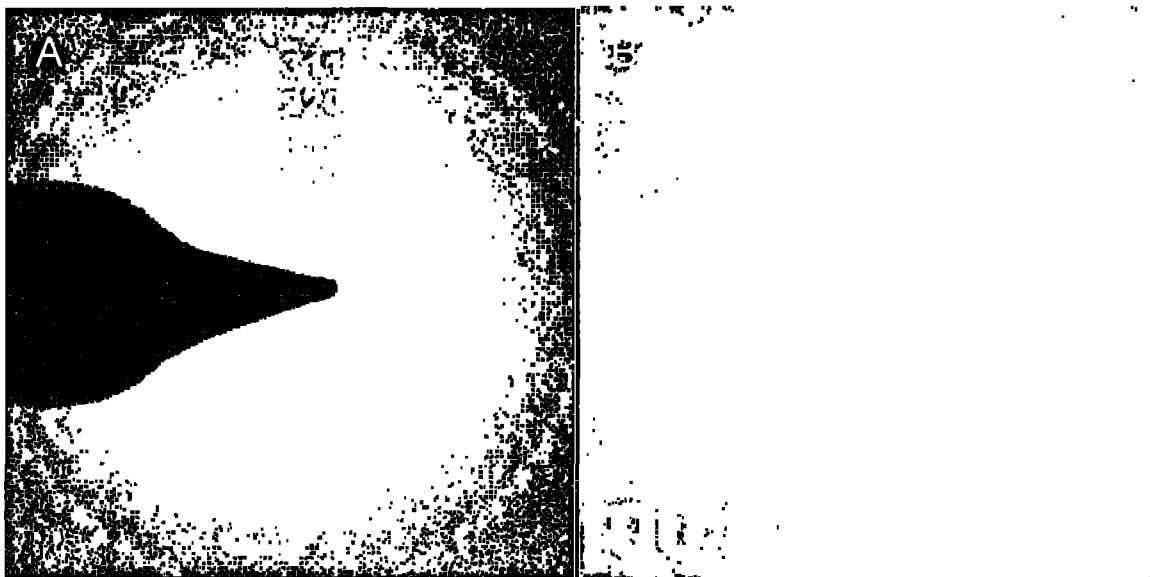
Introduction

This chapter discusses three major characterization techniques to determine crystalline nature and magnetic properties of nanoparticles in nano-phase. Crystallinity of nanoparticles was determined using select area electron diffraction (SAED) mode on transmission electron microscope (TEM). Magnetic properties at room and sub-zero temperatures were measured using a superconducting quantum interference device (SQUID) magnetometer and an alternating gradient magnetometer (AGM).

Transmission Electron Microscopy (TEM)

Transmission electron microscopy (TEM) was used in this study to determine the particle size, size distribution and crystalline nature of in-situ grown magnetic metal oxide nanoparticles in the sulfonated SEBS BCP matrix. Morphology of SEBS BCPs has been studied in unsulfonated, sulfonated, and with inorganic metal oxides. In this dissertation, we will emphasize particle size and size distribution of magnetic nanoparticles in one of the BCP phase (sPS block here).

After studying particle size of sSEBS/magnetic nanocomposites and its crystalline nature was investigated using TEM in SAED mode. In this technique, the incident electron beam is condensed to form a fine spot beam by means of a diffraction grating. The spot beam on interaction with an isolated nanoparticle produces its diffraction pattern. Based on the crystal structure, the pattern forms are rings (in case of multi domain crystals) or dots for single crystals. Typical ring formation for a multi-crystalline structure and dot pattern for a single crystalline structure are shown in Figure II-1.



FigureII-1. SAED patterns for two different samples. A) ring pattern for multi crystalline structure, B) dot pattern for a single crystalline structure (adapted from ref.¹).

Transmission electron microscope column camera length (λ_L), at a given magnification, is a product of the diameter of the diffraction ring (R_s) and its crystal index parameter (a).¹ A diffraction pattern of a standard sample, which has crystal index parameter is reported in the literature, was obtained to ascertain (λ_L) before obtaining the diffraction pattern of nanoparticles. The crystal index parameter (a') for the nanoparticles was computed using equation 1, after measuring diameter (r) of its diffraction pattern at the same magnification.

$$\lambda_L = R_s \cdot a = r \cdot a' \quad \text{Equation 1}$$

For identifying very low intensity diffraction rings, circular hough transform diffraction analysis script was used. The script was used with Digital Micrograph™ software developed by Mitchell *et al.*² The script measures diameter of each ring at ten different locations and provides an average diameter. By knowing the lattice parameter of the standard sample, the lattice parameter of nanoparticles will be determined.

Magnetic Measurements

Magnetic properties of nanocomposites were studied at room temperature and at temperatures close to absolute zero to predict whether the magnetic nanoparticles are superparamagnetic or ferri/ferromagnetic in nature. SQUID magnetometer measures these properties over a range of temperatures and is capable of measuring the effect of heating/cooling rates on magnetic properties.

Superconducting Quantum Interference Device (SQUID) Magnetometer

A SQUID magnetometer is a very sensitive magnetometer due to its ability to measure small changes in electrical current when a magnetic sample is introduced in a sensing coil. It consists of superconducting electric pick-up coils which works on the concept of a Josephson junction. Josephson junction is an electric circuit which can conduct electric current at temperatures close to absolute zero. Each pick-up coil has at least one or more weak junctions which flows less critical current i_c , than the entire coil. A schematic representation of Josephson junction is shown in Figure II-2.

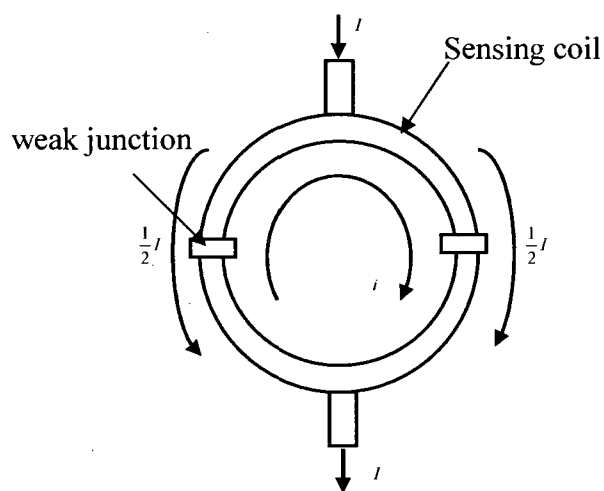


Figure II-2. Schematic representation of a Josephson junction electric circuit in SQUID magnetometer.

When a magnetic flux is applied, the electron flows at these weak links lose momentum than the rest of the coil and generates a phase difference. The dependence of magnetic flux is observed as a function of current or vice versa. And, when a magnetic sample is introduced at the center of the coil, the change in the current in the coil is measured as function of magnetic flux generated by the magnetic moments present in the material and calibrated to give magnetic long moments.

Using SQUID, the superparamagnetic nature of nanoparticles can be studied by conducting heating/cooling rate measurements.

Zero-Field Cooled (ZFC) and Field Cooled (FC) Magnetic Measurements

ZFC and FC methods measure the magnetization as a function of temperature (T). ZFC is a common method to measure the transition temperature (T_B) at which a ferri- or ferromagnetic material translates into a paramagnetic material. ZFC measurements are beginning sequence of the method where the sample is cooled to 4 or 5 K in zero applied magnetic field (no field) and stabilized for 5 minutes. The temperature is then ramped to 300 K at an interval of 10 K. When the sample is cooled to 5 K in zero field, all the magnetic moments are frozen in their current state, and when temperature is ramped in presence of a small magnetic field, they will align in the direction of field and magnetization value will increase to peak value until a certain temperature (T_B), called blocking temperature is reached. After passing this T_B , magnetic moments will randomize due to increase in thermal energy kT and net magnetic moment will decrease. In case of FC measurements, the sample is cooled to 5K in presence of a small magnetic field. Due to the initial presence of applied field before freezing the sample, all magnetic moments are oriented in the direction of applied field and frozen in that direction. When

temperature is ramped up to 300 K at an interval of 10 K, due to the increase in thermal energy, the magnetic dipoles will randomize and decrease the net magnetic moment. The sharpness of ZFC curve gives information about the distribution of magnetic dipole moments and thus can be correlated to the distribution of their particle size.

SQUID is also used to measure the magnetic hysteresis (M vs. H) at different temperatures as a function of applied field strength. With the T_B , obtained from ZFC measurements, M vs. H curves can be obtained at temperatures below and above T_B and also near 300 K to study the superparamagnetic nature of magnetic nanoparticles.

Alternating Gradient Magnetometer (AGM)

AGM was used to measure the magnetic properties at room temperature. A magnetic sample was mounted at one end of a non-magnetic bimorph and the other end was rigidly connected to a piezo-electric transducer. When a magnetic sample containing bimorph was placed between two coils, and when an alternating gradient force was passed through these coils, it develops a magnetic flux and induces a magnetic force on the sample and makes it to deflect in the field. The movements of bimorph in x and y directions were transferred to the piezo transducer and calibrated as magnetic moment in the sample. Using AGM, hysteresis (M vs. H) measurements were performed at room temperature as a function of applied magnetic fields.

References

- (1) Electron Microscopy Sciences, Catalogue XVI.
- (2) Mitchell, D. R. G. *Ultramicroscopy* **2008**, 108, 367.

CHAPTER III

SECTIONAL ANALYSIS OF POLY [(STYRENE)-(ETHYLENE/BUTYLENE)-
(STYRENE)] TRIBLOCK COPOLYMERS USING ATOMIC FORCE MICROSCOPY:
CHANGES IN INTERFACIAL THICKNESS WITH SULFONATION

Abstract

The variation in styrene | ethylene/butylene block domain interfacial thickness with varying degree of sulfonation in poly [styrene-(ethylene/butylene)-styrene] triblock copolymers was studied via atomic force microscopy (AFM). Chemical composition was assumed to be proportional to the value of the phase in tapping mode AFM. Phase vs. distance profiles were generated and a geometrical method used to calculate interfacial thickness. Dynamic mechanical analyses (DMA) studies were also performed on these samples to understand phase separation and the effect of sulfonation. DMA indicated a consistent shift of the polystyrene block T_g to higher values, while T_g for the ethylene/butylene) blocks only increased slightly.

Introduction

Styrene containing triblock copolymers (BCP) with rubbery inner blocks belong to a family of thermoplastic elastomers (TPE) having excellent mechanical properties¹ and ease of processing in extrusion and injection molding.² BCP TPEs have thermally reversible, i.e., physical, rather than permanent chemical crosslinks.³ The 'crosslinks' consist of the hard block domains that have a high T_g . In styrene based BCPs, polystyrene (PS) blocks constitute the minor phase while rubbery blocks such as polybutadiene, polyisobutylene (PIB), poly (ethylene/propylene), poly (ethylene/butylene = EB) constitute the continuous major phase. The volume fraction of PS blocks, ϕ_{PS}

determines the morphology of the block copolymer, be it spheres, rods or lamellae in order of increasing ϕ_{PS} .^{4,5}

Mauritz *et al.* studied the structure and properties of PS-PIB-PS block copolymers and sulfonated versions which were used as templates for in situ sol-gel reactions that led to polymer/inorganic oxide nanocomposite materials⁶⁻⁹ and did the same for PS-P(E/B)-PS block copolymers, which is the system of interest here.¹⁰⁻¹²

In a simple view of the interface between two immiscible polymer, A and B, phases, whether in block copolymers two component polymer blends, the concentration of A is uniform throughout its phase, and likewise for B, and the composition profile perpendicular to the interface is a step function. However, this sort of discontinuity is an energetically unfavorable situation and limited mixing to varying extents causes narrow *interphases* with continuous rather than step composition profiles as depicted in Figures III-1 and III-2.

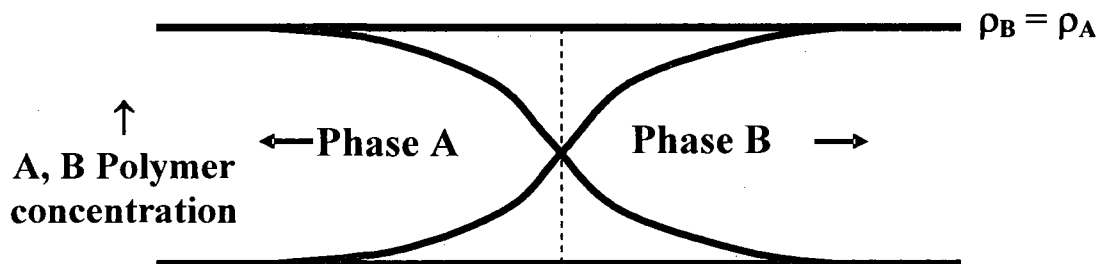


Figure III-1. Hypothetical concentration profiles of A and B components in a mixed interface (interphase) region of an immiscible polymer blend or phase separated block copolymer where the concentrations of A and B are equal.

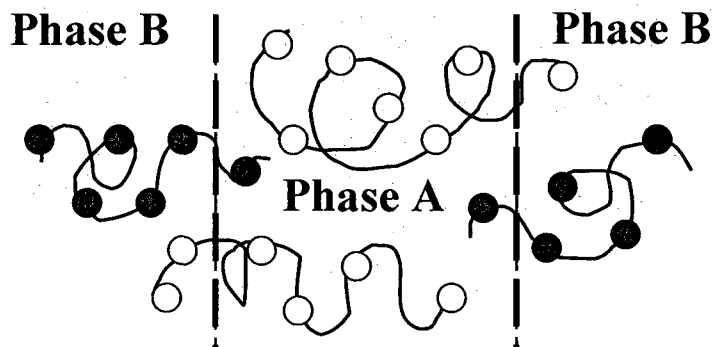


Figure III-2. Molecular view of limited block miscibility at the interface in phase separated block copolymers.

Helfand and Tagami developed a theory for inhomogeneous polymer-polymer interfaces in BCPs from which equations for the interfacial thickness result.^{13,14} The simplest theory assumes that the bulk densities of both polymers are equal ($\rho_A = \rho_B$), the degrees of polymerization (Z) of A and B are equal and approach ‘infinity’, for both polymers the effective length of a repeat unit (i.e., Kuhn length) is b so that the unperturbed mean square end-to-end distance is Zb^2 , and the compressibilities of both phases are equal. Of course, for SEBS, the densities of the PS and EB blocks are not equal and the degree of polymerization of the ethylene/butylene block is greater than that of the PS block. Nonetheless, in order avoid more complicated equations, those from the simple form of the theory will be used in discussion in a qualitative sense.

In the simple theory, the interfacial thickness (d) is related to the Flory-Huggins interaction parameter (χ) and b by the equation,¹³

$$d = 2b / (6\chi)^{1/2} \quad \text{Equation 1}$$

Thus, d becomes thinner as χ increases, i.e., as the energetic compatibility of the two polymers decreases. For the case at hand, this was affected by rendering the hard

blocks more polar through sulfonation. It should be remembered that both b and χ are a function of temperature.

Different groups employed nano-indentation and scanning probe techniques to determine interfacial thickness. Hozdic *et al*¹⁵ used nano-indentation to estimate the thickness of interfaces in polymer/glass composites and determined that the interface has stronger material properties than its constituent materials and the apparent width of interfacial regions between glass and polymer was about 2-6 μm . Van Landingham *et al*¹⁶ compared nano-indentation responses of both interface regions with its individual constituent materials of a polysulfone-epoxy adhesive system. They measured the width of the interface as approximately 3 μm based on variations in the response of interface and bulk epoxy and bulk polysulfone. Kim *et al*¹⁷ studied the effect of silane coupling agents on the interface properties of an E-glass woven fabric reinforced vinyl ester matrix composite. They observed the effect of silane coupling agents on elastic modulus of the matrix resin and the interfacial thickness was approximately 1 μm . However, each nano-indentation technique produced values which were not in agreement. Bogetti *et al*¹⁸ employed an AFM indentation method to study the interface properties and concluded that the thickness of interface was very small compared to the probe tip.

Tapping mode AFM is a very appropriate probe for differentiating between soft and hard phases in block polymers as it senses gradients in local viscoelastic properties. In operation, a cantilever tip taps across the surface and the hard and soft block phases are differentiated on the basis of the phase lag between the signal of the deflection of the vibrating cantilever and the input driving signal of the quartz crystal. The shade-coded pixels of the hard segments are bright when the phase lag is zero or very small, and the

phase lag of the soft segments is about 90° as depicted in Figure III-3. The phase angle value depends on local viscoelastic properties as well as attractive and repulsive forces between the surface and tip.

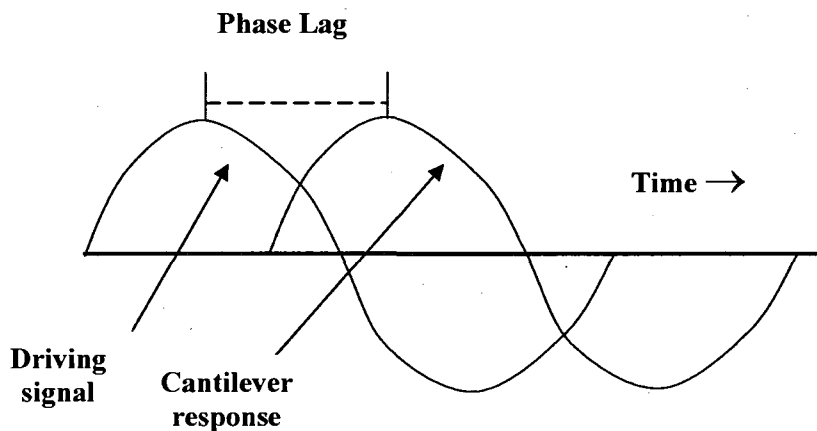


Figure III-3. Graph of driving force - response phase lag in AFM measurements when a cantilever tip is in contact with substrate surface in tapping mode.

Recently, Paradkar *et al*¹⁹ employed tapping mode AFM (TMAFM) to investigate interfacial thicknesses of multilayer polyolefin films. Gao *et al*²⁰ employed TMAFM to investigate interfacial properties of glass-fiber-reinforced polypropylene and epoxy matrix composites.

In the work reported here, this semi quantitative evaluation of limited mixing at interfaces and interfacial thickness was used for SEBS samples wherein the polarity of the hard block was varied by degree of sulfonation. The two publications mentioned in the previous paragraph involved polymer blend/composite systems with very long segments (on the order of micrometers). In our studies we investigated the interface thickness of BCPs with inter-domain spacing of about 20-30 nm.^{11,21} The following assumptions were made for easy mathematical calculations: 1) variation of density along

a sectional analysis profile will not affect the interface thickness, 2) convolution of the tip (related to bluntness) is negligible and will not affect sectional profile extraction.

Experimental

Materials

The SEBS block copolymer, Kraton[®] G1652, obtained from Kraton[®] LLC, had ~30 mol % styrene and total $M_n = 73,600$ g/mol. All reagents used for sulfonation were used without further purification. Dichloroethane (DCE) (99.8%), toluene, 1-hexanol (98%), acetic anhydride (ACS grade) and sulfuric acid (ACS grade) were obtained from Fisher Co.

Sulfonation Procedure

Sulfonation of styrene blocks in SEBS was performed up to ~20 mole % according to a previously reported procedure.^{10,22} In brief, the BCP was dissolved in DCE at ~54° C. The sulfonating agent, acetyl sulfate, was prepared by mixing DCE and acetic anhydride and cooled to -10° C after which sulfuric acid was added. Once acetyl sulfate was prepared, it was used in less than 10 min. In order to obtain the desired final sulfonation level, a required amount of acetyl sulfate was added to the BCP/DCE mixture. The color of the final reaction mixture changed from normal to light brown and then to dark brown from lower to higher levels of sulfonation. The reaction proceeded for 2h and the final polymer was recovered by boiling it several times, filtration, and finally drying under vacuum at 60° C for 7d to remove any residual water. The sulfonation level was determined by dissolving 0.1 mg of sample in a toluene/hexanol mixture at 80° C against standardized base to a phenolphthalein end point. Percent sulfonation values obtained from standard titration were 2-3 % consistent with values obtained from

elemental analysis. All five samples are labeled as in Table III-1. For example, 0SEBS means 0 mole % sulfonation, and 6SEBS means 6 mole % sulfonation of SEBS.

Table III-1. Sample codes for different degrees of sulfonation

Sample	Sample ID
Un sulfonated SEBS	0SEBS
6 mole % sulfonated SEBS	6SEBS
10 mole % sulfonated SEBS	10SEBS
16 mole % sulfonated SEBS	16SEBS
20 mole % sulfonated SEBS	20SEBS

Film Casting Procedure

A 10% solution was prepared by dissolving an unmodified BCP in toluene which was then cast in a Teflon[®] petri dish and allowed to dry at ~45° C for 7d and then annealed under vacuum (~30 in Hg) at 120° C for 2d. Films of sulfonated SEBS were cast in the same manner but they were dissolved in a mixture of toluene and hexanol as a co-solvent.

Samples for AFM and DMA Investigations

All films were cut into small triangular shapes with a base at least 10 mm wide and pasted vertically on 12 mm diameter AFM discs with an epoxy steel resin, and dried for a few hours until the epoxy hardened. Prior to pasting, the surfaces of AFM discs were polished with sandpaper to facilitate proper contact between epoxy and the metal surface. The top tip of a triangular shaped sample was trimmed with a razor blade to avoid wiggling when the sample approached a diamond knife. The surface polishing was performed at - 75° C as T_g of the EB block is around - 40° C. In order to avoid loss of surface features on the polished samples, the temperature below T_g of the EB block was

chosen so that both PS and EB chains are frozen. Each sample was placed in a Leica ultra cryo-microtome chamber (UC FC6) at -75°C .

Samples for DMA were prepared by cutting pre-formed films with a standard 5.3 mm width punch from TA Instruments and the length of each sample was maintained at 12-15 mm.

AFM and DMA Measurements

AFM sectional profiles were obtained by tapping polished mirror surfaces of samples generated by cryo-microtoming. Scans were performed at ambient conditions using a Dimension 3000 AFM with NanoScope[®] III controller from Veeco Co. (Digital Instruments). Tapping mode was used for analyzing the surface over at least at a scan area of $2 \times 2 \mu\text{m}^2$. RTESPW[™] probes from Veeco[™] Co. with a typical cantilever length of 115-135 μm were chosen for this work. The nominal spring constant and resonance frequency ranges were 20-80 N/m and 239-286 kHz, respectively. The tip radius curvature, as reported by the manufacturer, was less than 10 nm. High resonance frequency tips were used to ensure maximized phase contrast between hard and soft blocks. The main goal was to determine how interfacial thickness varies with degree of SEBS sulfonation from the AFM tapping-phase profiles. It is assumed that phase contrast issuing from AFM-tapping is proportional to the composition at a given point in the mixed regions because the hard and soft phases have widely different glass transition temperatures. To be sure, the output is not chemical composition *per se* but the results have significance at least in a qualitative sense and data trends are meaningful. Images were obtained at a frequency of 1 Hz or lower for highest resolution. (Resolution depends on the number of line scans that complete a full scan at a specified frequency).

Instrumental parameters such as tip shape, feed back control, etc., were controlled to obtain maximum possible resolution. Once the samples were surface polished with the cryo-microtome, they were placed in the AFM within 5 min to avoid dust deposition on the surface giving image artifacts. For each sample, a new tip was used to ensure that tip convolution was not a factor.

DMA measurements were performed using a DMA Q800 equipped with a GCA liquid nitrogen chilling unit capable of cooling samples to -160°C in the DMA sample chamber. For all DMA vs. temperature (T) scans, the tensile mode was used at 1 Hz in the range of -60 to 160°C at a heating rate of $2^{\circ}\text{C}/\text{min}$.

Results and Discussion

All samples were microtomed to observe the morphology of cross sections. Post-microtoming steps were followed as described in the Experimental section. Tapping mode AFM (TMAFM) phase images of all five samples, 0SEBS, 6SEBS, 10SEBS, 16SEBS and 20SEBS are shown in Figures III-4 a-e.

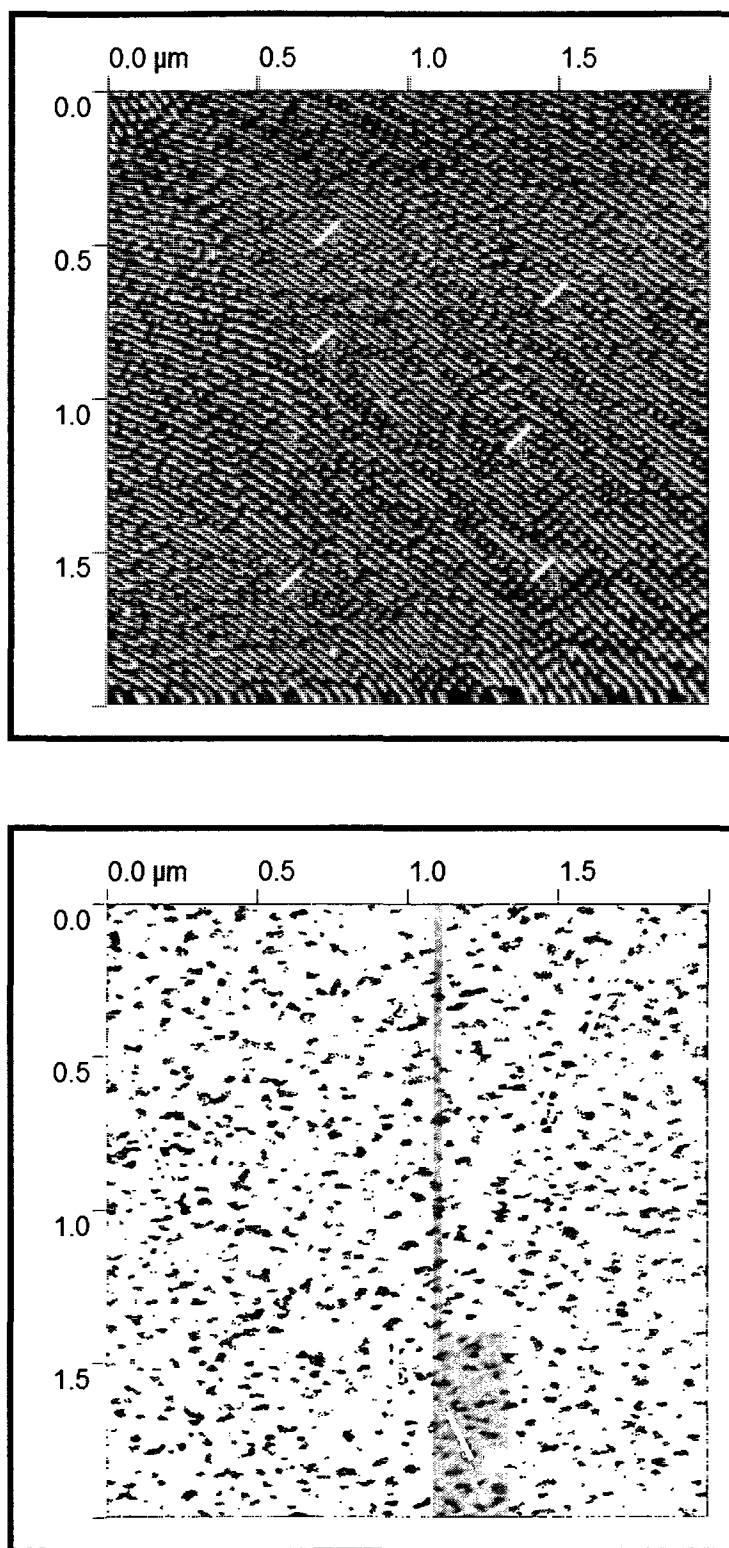
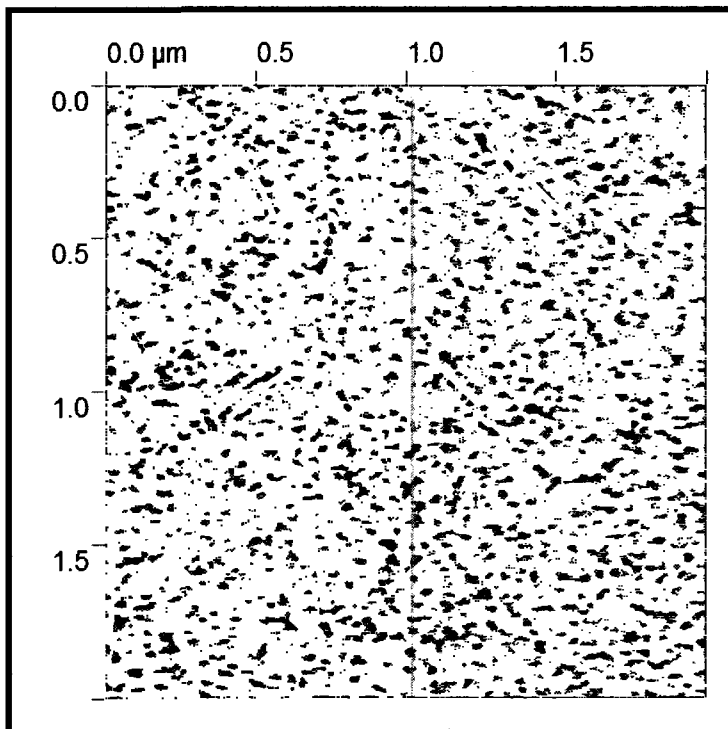
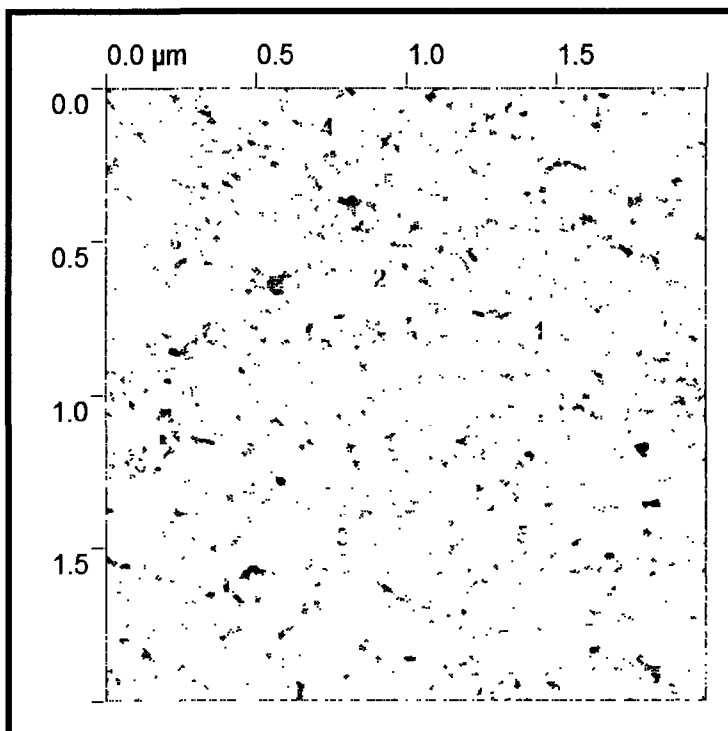
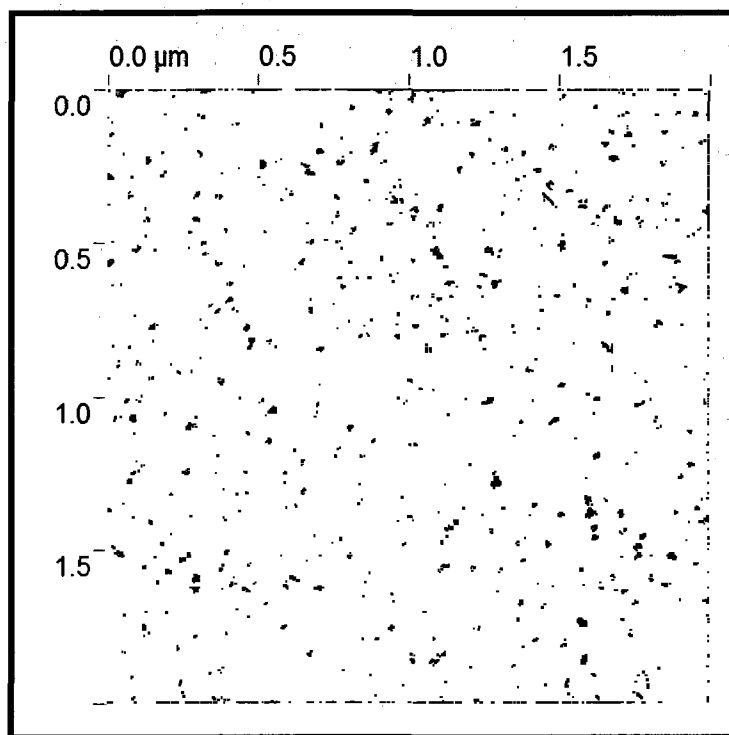


Figure III-4 (a-e). TM-AFM phase images of 0SEBS, 6SEBS, 10SEBS, 16SEBS and 20SEBS, respectively. Lines along which sectional analysis was performed are in white.





In these figures the lines along which sectional analysis of each sample was performed, for least at six different locations, are indicated in white. For sample 0SEBS (unsulfonated) in Figure III-4 (a), there is clear hexagonal packed cylindrical (HPC) morphology with an inter-domain spacing of ~ 25 nm which is very close to the values obtained from small angle X-ray scattering studies.²¹ These are rods rather than lamella because circular cross sections perpendicular to the image are seen. In earlier work, Blackwell *et al.* observed a change in morphology of sulfonated (s) SEBS from that of hexagonal packed cylinders to lamellae when increasing the mole percent sulfonation to ~ 14 % [11]. Transition of morphology from HPC to lamellar patterns for 0SEBS to 10SEBS (Figures III-4 a through c) and then from 10SEBS to 20SEBS (III-4d and e) to a frustrated morphology, was observed. The formation of less-organized granular-like

morphology at higher degree of sulfonation might be due to considerably retarded chain motions in the PS blocks during the process of film formation [10].¹⁰

Raw phase images from Veeco™ Dimension software were processed using Gwyddion 2.9 software with a GTK+ graphical user interface.²³ For each profile, at least 4 megabytes of text data was acquired in BSpline mode to attain highest resolution of data processing. Typical sectional profiles for each sample are displayed in Figures III-5 a-e. No two profiles are exactly alike but capture the nature of compositional variation and yield inter-feature distances within narrow ranges over the image. In each profile of every sample, a complete single cycle of tip track (maximum-to-immediate maximum point) was taken.

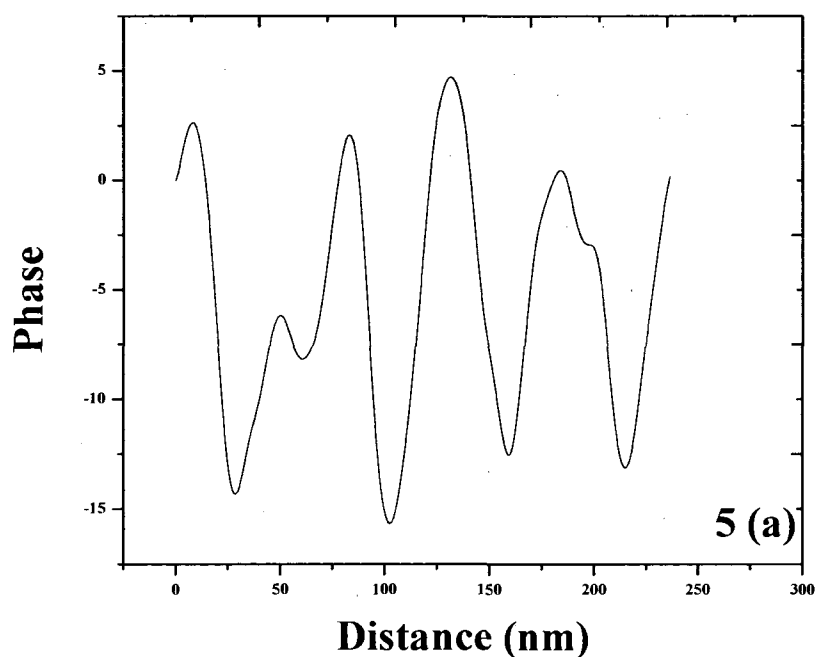
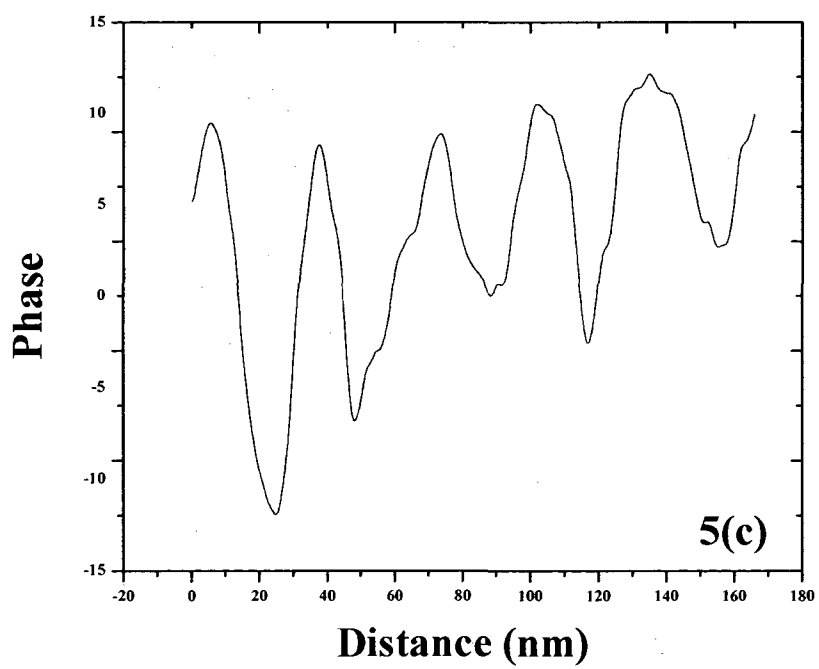
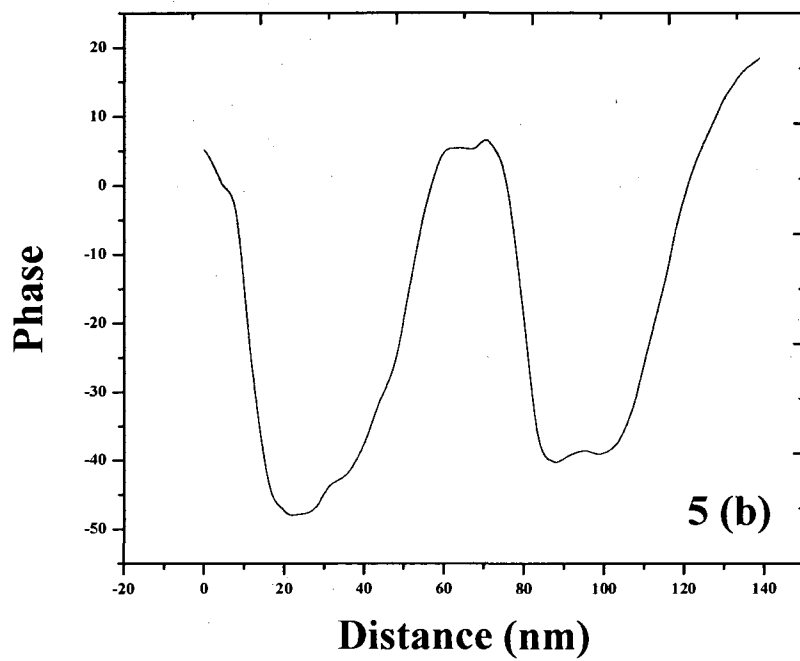
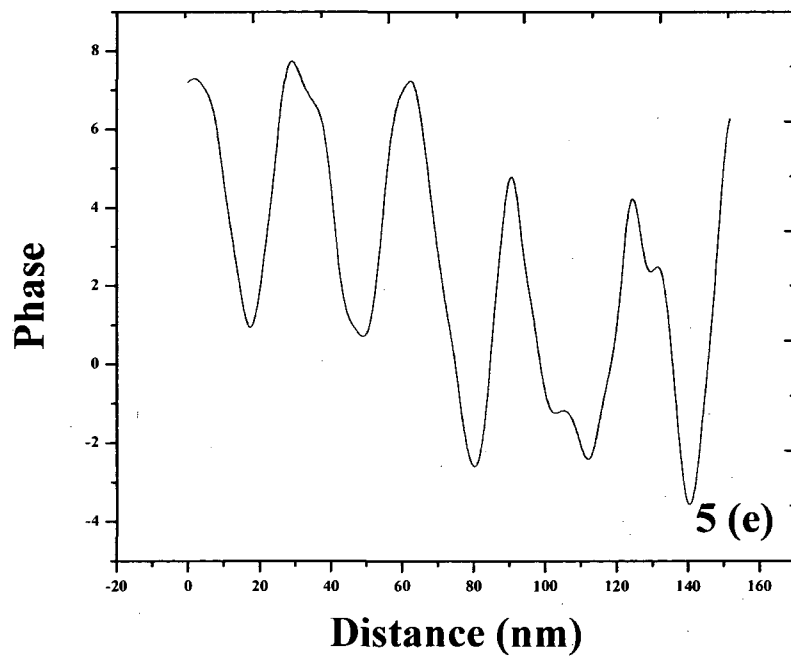
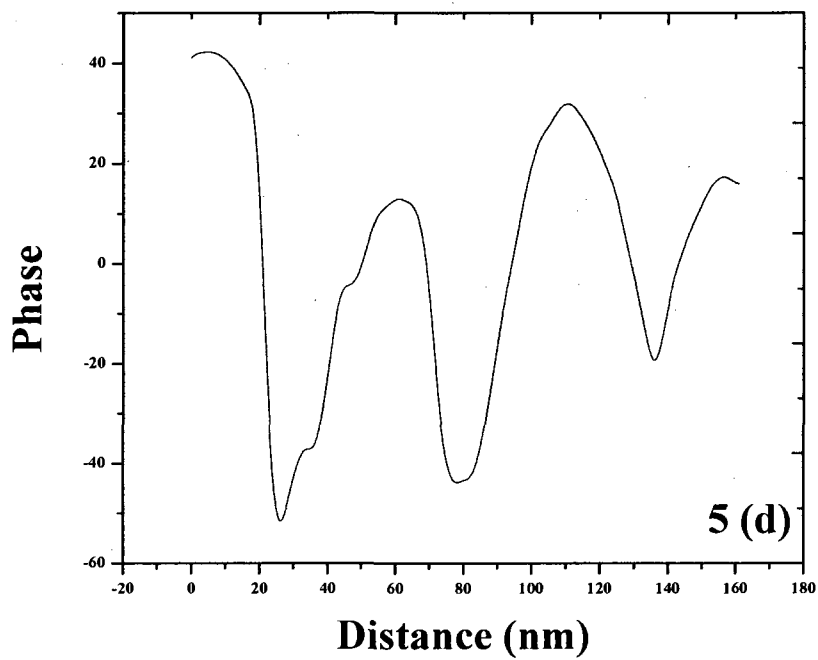


Figure III-5 (a-e). Representative sectional analysis profiles at single locations on samples 0SEBS, 6SEBS, 10SEBS, 16SEBS and 20SEBS, respectively.





Tangent lines at inflection points and an adjacent peak point can be drawn as shown in Figure III-6 to locate the intersection of these tangents. The horizontal distance between two intersection points gives a measure of interfacial thickness d .

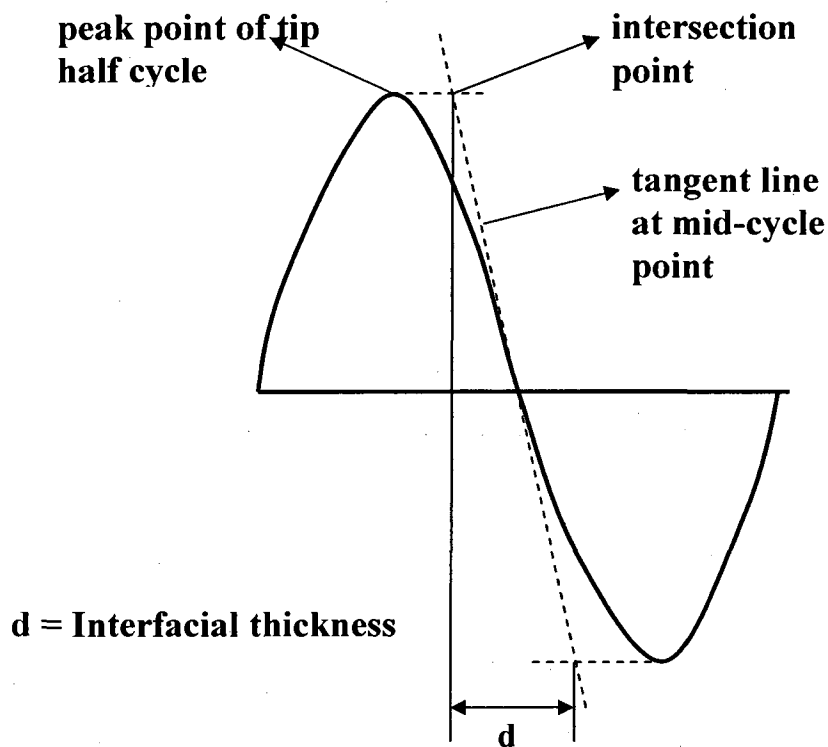


Figure III-6. Graphical description of method of determining interfacial thickness (d) from AFM tapping-phase profiles.

d values at different percent sulfonation are listed in Table III-2. It is observed that with increase in sulfonation to 10%, d decreases, presumably due to an increase in χ between sPS-EB blocks. However, for 16 and 20 percent sulfonation, d rises. This might be explained in the following way. Above 10 percent sulfonation PS block mobility becomes considerably restricted due to hydrogen bonding interactions between sulfonic acid groups. This kinetic impediment does not allow for sharp demarcation between the two phases and interfacial thickness consequently increases. In these cases, the structure

of interphase regions is more the consequence of slow chain rearrangement kinetics rather than the energetics embodied in the equilibrium parameter χ .

Table III-2. Interfacial thickness values (d) at different mole % sulfonation

Sample Name	Interfacial thickness (nm)	% change
0SEBS	19.52	
6SEBS	14.30	-26.7
10SEBS	11.26	-42.3
16SEBS	15.06	-22.8
20SEBS	16.28	-16.6

From values shown in Table III-2, it is also evident that interfacial thickness values are lesser than the experimental inter-domain spacing, which is 20-30 nm.^{10,21} With increase in sulfonation, the decrease of interfacial thickness (d) for 0SEBS to 6SEBS is 26.7 % and for 0SEBS to 10SEBS, it is 42.3% while for 0SEBS to 16SEBS is 22.8% For sample 20SEBS, decreased to 16.6%, much less than for 16SEBS.

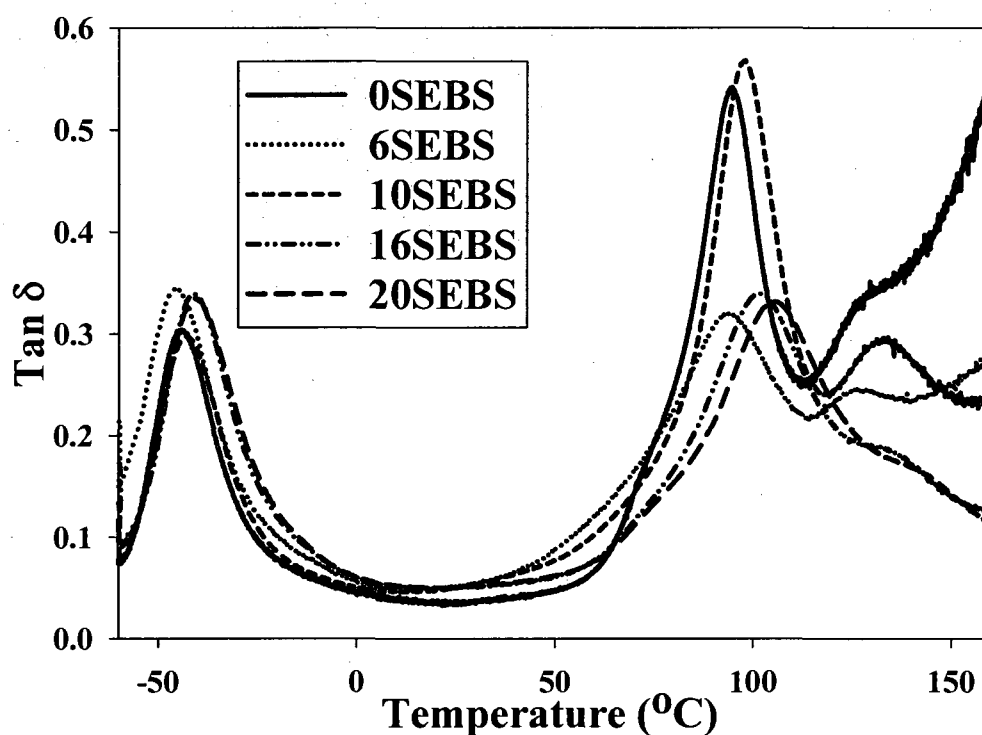


Figure III-7. Tan δ vs. T plots for samples 0SEBS, 6SEBS, 10SEBS, 16SEBS and 20SEBS.

DMA experiments on all five samples were performed at least twice to demonstrate tan δ vs. T data reproducibility and it was seen that this is the case. The curves for all samples are shown in Figure III-7. There are two glass transitions, as seen in our earlier work on SEBS materials.¹⁰ T_g values (taken as peak temperatures) for all five samples for the EB and PS (sPS) block domains before and after sulfonation are listed in Table III-3. As shown in Figure III-7, the PS block domain tan δ peak undergoes a significant shift to higher temperatures from 95.4 to 105.4° C from 0SEBS to 20SEBS and the peak height decreases with increasing percent sulfonation. This behavior is attributed to restricted chain mobility with increase in $\text{SO}_3\text{H} \cdots \text{OSO}_2\text{H}$ hydrogen bonding interactions. EB block T_g values did not vary as much, being around -40° C, with a spread of 4.8° C although the peaks do shift somewhat to higher temperatures with

increase in percent sulfonation. This shift may be due to stronger interactions in the hard block domains that anchor the inner blocks more firmly with increase in sulfonation. The EB peaks broaden toward their high temperature side which may be due to an overlapping peak due to sub-Rouse motions.²⁴

There is a distinct peak above the PS block domain glass transition for all samples including the unsulfonated control. According to Weiss *et al.*, a peak at high temperatures ($\sim 120^\circ\text{C}$) is due to formation of $-\text{SO}_3\text{H}$ rich sub-domains in the PS blocks, which could be the acid group associations mentioned above. In the case of unmodified SEBS, the high temperature peak past the PS T_g is attributed in the literature to the lattice-disorder temperature.²⁵ In Figure III-7, it is observed that there is a shoulder just before the PS $\tan \delta T_g$ peak and this may be attributed to the diffusion of PS chain ends into EB blocks and vice versa, i.e., mixed interphases. The broadening of the PS peak may be due to a broadening of the distribution of unsulfonated (PS) and sulfonated (sPS) chain segments.

Table III-3. Hard and soft block glass transition temperatures

Sample ID	T_g of EB block ($^\circ\text{C}$)	T_g of PS/sPS) block ($^\circ\text{C}$)	ODT ($^\circ\text{C}$)
0SEBS	-44.3	94.4	127.2
6SEBS	-45.3	93.8	127.0
10SEBS	-42.9	97.8	132.7
16SEBS	-40.5	101.7	135.5
20SEBS	-40.8	105.4	145.5

Conclusions

Sectional analyses of composition gradients, from the perspective of AFM tapping-phase, were performed for unsulfonated and sulfonated SEBS samples to

determine interfacial thickness d in these two phase systems. d decreases with increase in sulfonation up to 10 mole % and then increases for 16, and then again for 20 mole % sulfonation. The initial decreasing behavior is viewed in terms of an increase in the Flory-Huggins interaction parameter owing to the increase in polarity of the PS phase. The subsequent increase in d might be viewed as being due to chain motional constraints owing to interactions between SO_3H groups that influence the kinetics of film formation which is not accounted for in the conventional equilibrium theory of interfaces that favors weak interactions. The increase in the glass transition peak temperature as well as its suppression, for the sPS block phase as seen in dynamic mechanical $\tan \delta$ vs. temperature spectra is in harmony with this notion.

Acknowledgements

We acknowledge the National Science Foundation (NSF) Material Research Science and Engineering Center (MRSEC) Division of Materials Research (DMR-0213883) for Stimuli Responsive Materials at the University of Southern Mississippi for funding. We also thank Kraton® LLC for donating SEBS block copolymers.

References

- (1) Holden, G. *Understanding Thermoplastic Elastomers*. Munich: Hanser Publishers, 2000.
- (2) Craver, C. D.; Carraher, C.E, Jr., editors. *Applied Polymer Science: 21st Century*, 2000.
- (3) Holden, G.; Legge, N. R.; Quirk, R. P.; Schroeder, H. E, editors. *Thermoplastic Elastomers*, 2nd ed. 1996.
- (4) Bates, F. S.; Fredrickson, G. H. *Annual Reviews In Physical Chemistry* **1990**,41,525.
- (5) Hajduk, D. A.; Harper, P. E.; Gruner, S. M.; Honeker, C. C.; Kim, G.; Thomas, E. L.; Fetters, L.J. *Macromolecules* **1994**,27,4063.
- (6) Mauritz, K. A.; Storey, R. F.; Mountz, D. A.; Reuschle, D. A. *Polymer* **2002**,43,4315.
- (7) Mauritz, K. A.; Storey, R. F.; Reuschle, D. A.; Beck Tan, N. *Polymer* **2002**,43,5949.
- (8) Kwee, T.; Taylor, S. J.; Mauritz, K. A.; Storey, R. F. *Polymer* **2005**,46,4480.
- (9) Mountz, D. A.; Storey, R. F.; Mauritz, K. A. *Journal of Polymer Science Part B: Polymer Physics* **2005**,43,764.
- (10) Blackwell, R. I.; Mauritz, K. A. *Polymer* **2004**,45,3457.
- (11) Blackwell, R. I.; Mauritz, K. A.; Beyer, F. L. *Polymer* **2004**,45,3001.
- (12) Blackwell, R. I.; Mauritz, K. A. *Polymer Advanced Technology* **2005**,16,212.
- (13) Helfand, E. *Accounts in Chemical Research* **1975**, 8,295.

- (14) Helfand, E.; Tagami, Y. *Journal of Polymer Science Part B: Polymer Physics* **1971**,9,741.
- (15) Hodzic, A.; Stachurski, Z. H.; Kim, J. K. *Polymer* **2000**,41,6895.
- (16) Vanlandingham, M. R.; McKnight, S. H.; Palmese, G. R.; Bogetti, T. A.; Eduljee, R. F.; Gillespie, J.W. Jr. *Matereal Research Society Symposium Proceedings* **1997**,458(Interfacial Engineering for Optimized Properties),313.
- (17) Kim, J-K.; Sham, M-L.; Wu, J. *Composites, Part A* **2001**,32A ,607.
- (18) Bogetti, T. A.; Wang, T.; VanLandingham, M. R.; Gillespie, J. W. Jr. *Composites, Part A* **1998**,30A,85.
- (19) Paradkar, R. P.; Li, J.; Bar, G.; Pham, H.; Bosnyak, C.; Weinhold, J. *Journal of Applied Polymer Science* **2007**,106,1507.
- (20) Gao, S-L.; Mader, E. *Composites, Part A* **2002**,33A,559.
- (21) Weiss, R. A.; Sen, A.; Pottick, L. A.; Willis, C. L. *Polymer* **1991**,32,2785.
- (22) Weiss, R. A.; Sen, A.; Willis, C. L.; Pottick, L. A. *Polymer* **1991**,32,1867.
- (23) Gwyddion® is a Free and open Source software for evaluating Scanning Probe Microscopy (SPM) data. Development is supported by Czech Metrology Institute.
- (24) Santangelo, P. G.; Ngai, K. L.; Roland, C. M. *Macromolecules* **1993**, 26,2682.
- (25) Tse, M. F. *Journal of Adhesion Science and Technology* **1989**,3,551.

CHAPTER IV
STRUCTURE AND PROPERTIES OF SULFONATED POLY [STYRENE-b-
(ETHYLENE-co-BUTYLENE)-b- STYRENE]/ [COBALT FERRITE]
NANOCOMPOSITES

Abstract

Cobalt ferrite nanoparticles were grown in sulfonated (s) poly(styrene-ethylene/butylene-styrene) (SEBS) triblock copolymers *via an in-situ* precipitation method. Thermogravimetric analysis indicated single step degradation and the inorganic content of these materials. Transmission electron microscopy (TEM) revealed particles with sizes of ~20 nm. Wide angle ray diffraction results showed that the nanoparticles possess an inverse spinel cobalt ferrite crystal structure. The shifts of the glass transition temperatures for the two block phases upon sulfonation, and then with cobalt ferrite incorporation, suggest that the nanoparticles selectively incorporate in the sSEBS phase, which is also seen by TEM. Magnetization curves derived using an alternating gradient magnetometer show no hysteresis and that these nanocomposites are superparamagnetic at room temperature. Zero-field-cooled and field-cooled curves generated using SQUID magnetometry revealed a blocking temperature of 50K which reinforces the idea that these nanocomposites are superparamagnetic at room temperature.

Introduction

Magnetic ferrite materials in different forms are considered for applications involving microwave frequency electromagnetic (EM) wave absorption,¹⁻³ in particular, as radar absorbing materials (RAM).⁴ As opposed to EM wave absorption in dielectric materials, advantages of magnetic RAM coatings are that they can be thinner and provide

low frequency range performance. As in the case of dielectric permeability, the magnetic permeability is the sum of real and imaginary components, $\mu^* = \mu' + i \mu''$ that are frequency dependent. Cobalt ferrites are considered in this context because they possess high cubic magnetocrystalline anisotropy, high coercivity and moderate magnetization saturation values.^{5,6} Moreover, cobalt ferrites can be magnetized in weak fields ($H \leq 8 \times 10^4$ Oe). Absorption properties are favorable in bulk samples or at least down to the microscopic level but when the particle size is reduced to a critical nanoscopic size their EM absorption is enhanced at different frequencies due to an increase in surface area-to-volume ratio.⁷

There are ways of generating nanoscopic particles by high temperature methods^{8,9} although these processes are costly, energy-intensive, and nanoparticle aggregation imparts undesirable electrical inter-particle conductance. This problem can be avoided by the use of *in-situ* precipitation methods¹⁰ that are simple, can be performed at room temperature, and are of low cost.

Nanoparticle dispersion can be improved by atom-by-atom growth of particles throughout an organic polymer matrix. The issues affecting the EM wave absorption signature for these materials are nanoparticle size, shape, size distribution, volume fraction and degree of particle aggregation. Interfacial issues in diamagnetic organic polymer matrix media may also be important, not necessarily from the magnetic, but rather from the dielectric perspective. In particular, nanoparticle/matrix interfacial polarization relaxation can occur owing to high particle surface-to-volume ratio and differences in the dielectric permittivity values of the nanoparticles and polymer host.

In an effort to disperse *in situ*-grown nanoparticles by an atom-by-atom building process, block copolymers offer advantages over simple homopolymers.¹¹⁻¹⁴ An ordered phase separated morphology of hard/soft block copolymers in which the hard block is polystyrene (PS), which can be sulfonated, provides an interactive template in which metal ions and water from an external contacting electrolyte preferentially migrate to the polar sulfonated domains. This, in fact, has been performed by Rajan et al. and the work reported herein is a continuation of these efforts.^{15,16}

In this work, a sulfonated poly[styrene-(ethylene/butylene)-styrene] (SEBS) triblock copolymer was used in this role. The random ethylene-*co*-butylene (EB) soft blocks, whose domains have a low glass transition temperature, serve to prevent the material from becoming too brittle which is a disadvantage for a RAM coating on a flexible surface. Once the magnetic metal ions reside at/in the polar domains, metal oxide nanoparticles can be grown via the reactions described here. While the equilibrium morphology of SEBS consists of hexagonal packed PS rods in a continuous EB phase, it was seen to shift to lamellar morphology upon sulfonation to a degree of 12-14%. The inter-domain spacing in these materials, determined from AFM and SAXS investigations, is ~ 20-30 nm, which is also the anticipated order of the size of magnetic metal oxide nanoparticles grown in this morphology.¹⁷

Bulk cobalt ferrite (CoFe_2O_4) material has an inverse spinel crystalline structure, AB_2O_4 , in which the Co^{+2} and half of the Fe^{+3} ions exist in octahedral coordinated sites (B) and the remaining half of the Fe^{+3} ions exist in tetrahedral sites (A).¹⁸ In the bulk state, the magnetic remanance (σ_r) and saturation magnetization (σ_s) are 67 and 81 emu/g, respectively.¹⁹⁻²¹ The critical diameter for a single particle is 14 nm in that beneath this

size the particle behaves in paramagnetic fashion and the coercivity (H_c) and σ_r go to zero.²²

Of particular interest in these studies are nanoparticles dispersed throughout a phase separated polymer matrix such that they are above the critical size whereby the material behaves in ferromagnetic fashion at room temperature. Materials that absorb incident electromagnetic radiation on the basis of magnetic interactions must exhibit hysteresis so that energy is absorbed during each cycle of magnetic field oscillation. It is postulated here that frequency-selective absorption of electromagnetic energy can be achieved by tailoring the size, size distribution, shape, and inter-nanoparticle spacings for various compositions.

Experimental

Materials

The poly[styrene-(ethylene/butylene)-styrene (SEBS)] block copolymer (BCP) used in these studies was commercial Kraton G[®], grade 1652, obtained from Kraton LLC. This polymer has a number average molecular weight, $M_n = 79,000 \text{ g}\cdot\text{mol}^{-1}$ and ~30 mol % styrene block composition. Toluene, 1, 2-dichloroethane (DCE), dimethyl acetamide (DMAc), 1-propanol, acetic anhydride, 98% sulfuric acid, anhydrous ferric chloride (FeCl_3), cobalt chloride ($\text{CoCl}_2\cdot 6\text{H}_2\text{O}$) and sodium hydroxide (NaOH) were obtained from Fisher Scientific. All these reagents were used without further purification.

Sulfonation and Film Formation

The styrene blocks of SEBS were sulfonated to the degree 15-20 mole% as outlined in earlier similar studies.^{23,24} Percent sulfonation was determined from elemental analysis and the results compared favorably with those of titration. Also, consistency

was seen in the measurement of sulfonation by titration as 5 different pellets were tested for each sample and there was little deviation from the average in each case. The sulfonated SEBS (sSEBS) pellets were dissolved in a toluene/propanol 85/15% (v/v) mixture and cast into films of thickness 0.1- 1.0 mm on Teflon[®] petri dishes. These films were then dried in an oven at 45° C for 7d and then at 120° C in a vacuum oven for 2d.

Metal Oxide Nanoparticle Incorporation

The chemical reactions used to generate in situ nanoparticles are based on our previous work.^{15,16} The sSEBS films were swollen in DMAc for 24h after which they were removed and wiped with tissue paper. The films were tightly sealed in ziplock bags and thoroughly vacuum dried at 40° C prior to the swelling step which was intended to improve subsequent permeation of reactants. Then, the films were placed in a FeCl₃ + CoCl₂.6H₂O salt solution in DMAc (2:1 mol/mol) for another 24h, after which they were taken out of solution and their surfaces cleaned with tissue paper to remove possible surface precipitates. Following this, the films were soaked in 2M NaOH for another 24h and finally washed with DI water for 24h to remove excess electrolyte. After this ion exchange reaction the samples were dried in a vacuum oven at 120° C for 48h.

Material Structure/Property Characterization

The crystal structure of the inorganic oxide inclusions was determined using a Phillips X'PERT[™] x-ray diffractometer with CuK_{α1} radiation of wavelength 1.54 Å. X-ray scans were performed in the 2θ angle range of 15 to 75°. Nanoparticle size and size distribution was inspected using a JEOL JEM-2100 transmission electron microscope (TEM). 50 nm thick samples were obtained using a Leica cryo-ultra microtome. TEM samples were prepared at -70° C.

The inorganic content of these composites was determined using a TGA Q50 thermogravimetric analyzer and the data was analyzed *via* Thermal Advantage[®] software.

The glass transitions of the hard and soft block domains were determined using a TA DMA Q800 dynamic mechanical analyzer equipped with Advantage software.

Experiments were conducted in tensile mode with samples having a width of 5.3 mm.

The oscillatory frequency was 1 Hz and samples were ramped in temperature from -60 to 160° C at 2° C/min. For each sample, 2 runs were performed to assure data reproducibility, which was seen to be the case. DMA data was represented in terms of the temperature (T) dependence of the dynamic loss tangent, $\tan \delta = E''/E'$, where E' and E'' are the storage and loss moduli, respectively.

Magnetic hysteresis measurements at 5 K, zero field cooled (ZFC) and field cooled (FC) tests were performed using a Quantum Design Model MPMS SQUID magnetometer equipped with a helium flow cryostat. The ZFC and FC studies were performed to determine the blocking temperature (T_B) of the nanoparticles. In the ZFC study, the sample was cooled to 5K and stabilized at 5K for 15 min in the absence of a magnetic field and then heated to 375K in steps of 10 K.min⁻¹. A magnetic field of 200 Oe (Oersted) was applied and the magnetization (M) was measured during this heating. The system was allowed to stabilize at 375 K for 15 min, and then for FC measurements, cooled to 5K in steps of 10 K.min⁻¹ in the presence of a 200 Oe magnetic field and magnetization values were obtained when lowering the temperature. In both ZFC and FC studies, each measurement was taken after a stabilization time of 2 min for each step. Magnetometric measurements at room temperature were performed using a MicroMag™ 2900 alternating gradient magnetometer (AGM, Princeton measurements).

Results and Discussion

The crystalline nature of the metal oxide nanoparticles was determined using WAXD in the $15 - 75^\circ 2\theta$ angular range and the results are shown in Figure IV-1. The intensity peak positions were compared with literature values for bulk cobalt ferrite. From the Miller indices (hkl) for the peaks for this sample listed in Table IV-1 match those of a cobalt ferrite inverse spinel unit cell.²⁵

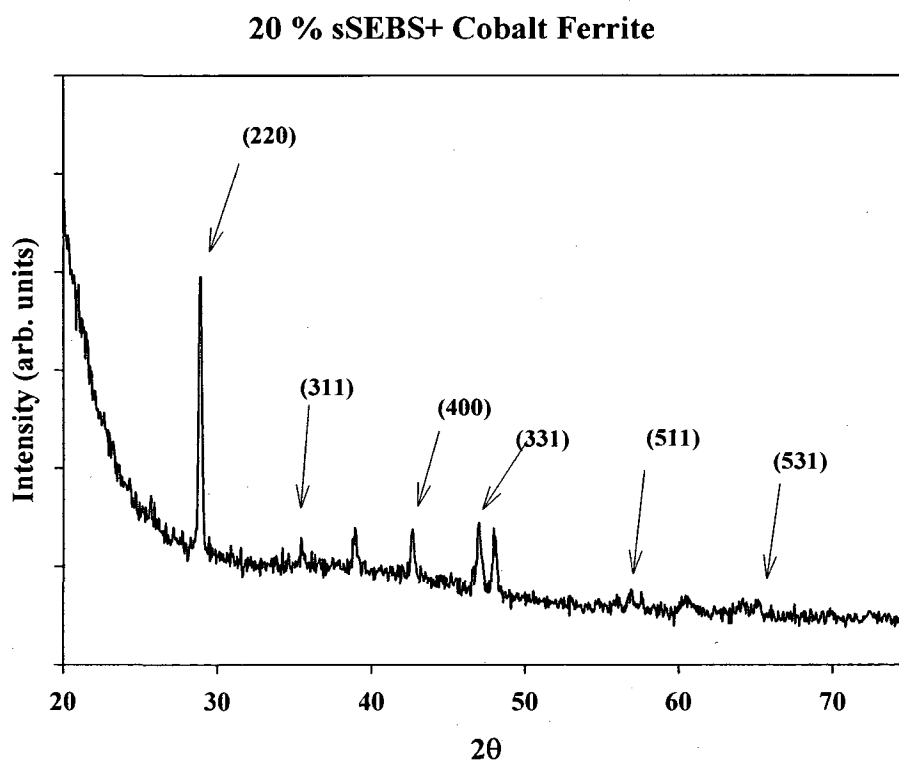


Figure IV-1. Wide angle X-ray diffraction peaks for a 20.0% sSEBS sample incorporating CoFe_2O_4 particles.

Table IV-1. WAXD peak intensity 2θ positions and comparisons with corresponding literature values for bulk cobalt ferrite. First column contains corresponding Miller indices for observed reflections.

hkl	Experimental (2θ)	Literature (2θ)
220	28.9	30.0
311	35.4	35.4
400	42.7	43.0
331	47.0	47.0
511	57.0	56.9
531	65.3	65.7

TEM was used to observe the particle size and size distribution. The sizes were observed to be ~ 20 nm as can be seen in the micrographs in Figures IV-2 and IV-3. Given the magnitude of these particle dimensions, the materials can be properly referred to as nanocomposites. In the image for a sample composed of 16.4% sSEBS incorporated with cobalt ferrite (Figure IV-2), the morphology of the block copolymer matrix can be faintly seen despite the fact that the polymer was unstained. Interestingly, the nanoparticles reside in the PS inter-domain regions whose spacings (~ 20 -30 nm) are only somewhat larger than the particle sizes. This might reflect the influence of morphology in a low order templating process. While some of the inclusions are likely aggregates of smaller particles, the array is reasonably well dispersed and this may be due to preferred particle incorporation in the hard block phases.

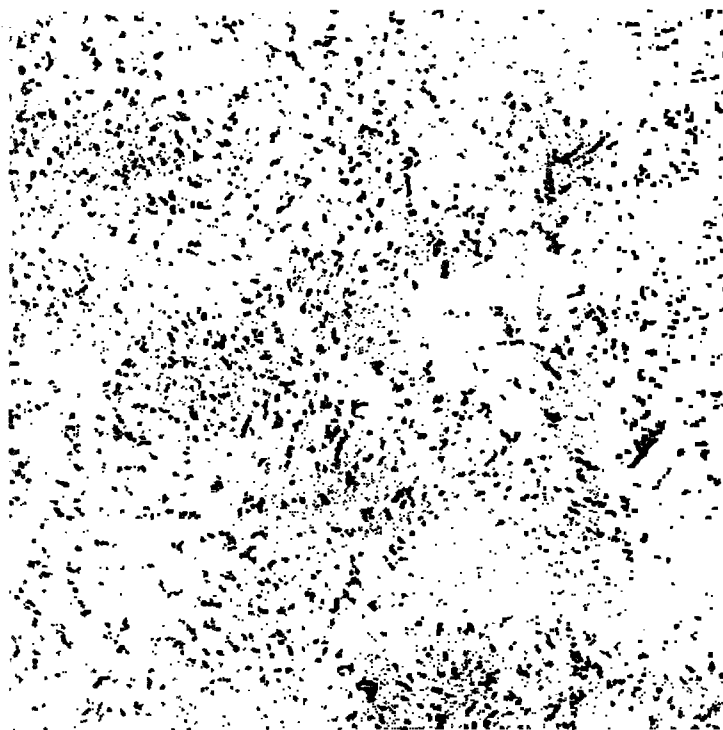


Figure IV-2. TEM micrograph for 16.4% sSEBS incorporating CoFe₂O₄ nanoparticles. Scale bar at lower-left is 200 nm.

Figure IV-3 is a TEM image for 20.0% sSEBS incorporating CoFe₂O₄. There is a distribution of nanoparticles of average size ~20 nm although in this case the morphology of the block copolymer is not clearly observed.



Figure IV-3. TEM micrograph for 20.0% sSEBS incorporating CoFe_2O_4 nanoparticles. The scale bar at lower-left is 100 nm.

The TGA scans for these materials, that were run at $10^\circ \text{C}/\text{min}$ from 30 to 700°C , are shown in Figure IV-4. While the polymer matrix has chemically distinct blocks with widely separated T_g values, the degradation appears to be of single step profile. The mass residues remaining at $\sim 600^\circ \text{C}$ following thermal degradation are 5.2 and 5.8 weight percent for the 16.4 and 20.0% sulfonated samples, respectively. Each value is the average of the results for 3 samples. The percent organic char obtained from the corresponding sulfonated films was $\sim 1\%$ so that after subtraction of this percent from the composite organic-inorganic residue the effective particle loading is 4.2 and 4.8% for the 16.4 and 20.0% sulfonated samples, respectively. Although the difference in percent sulfonation is significant, the difference between these uptakes is small.

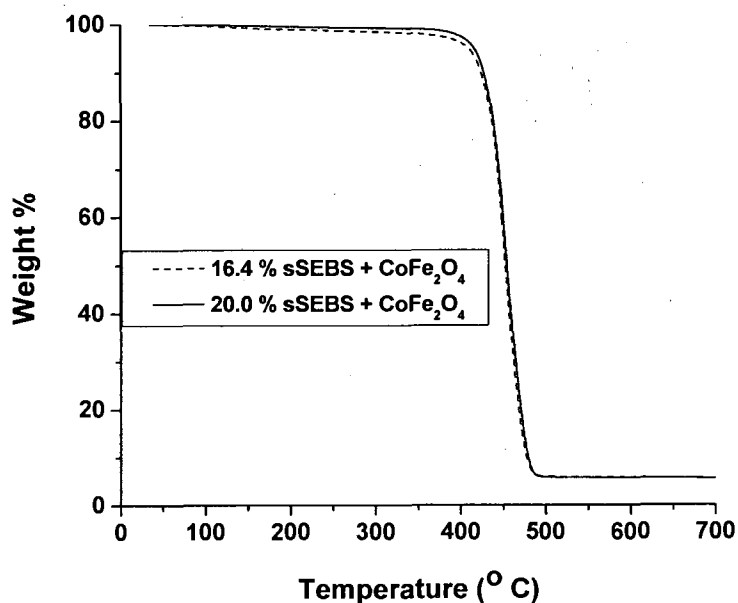


Figure IV-4. TGA thermograms for sSEBS/cobalt ferrite nanocomposites having two percent sulfonations.

For each percent sulfonation, dynamic mechanical data for the unmodified and sulfonated block copolymer and a cobalt ferrite filled sulfonated block copolymer were compared to ascertain changes in the hard (PS) and soft (EB) block domain glass transition temperatures (T_g) with each modification. The underlying hypothesis is that the inorganic inclusions will or will not reside in a given phase depending on whether or not the glass transition, reflective of long range chain motions, is significantly affected. Figures IV-5 and IV-6 are $\tan \delta$ vs. T curves for the two sulfonation percents. The T_g values obtained from these plots for the hard and soft block phases are listed in Table IV-2.

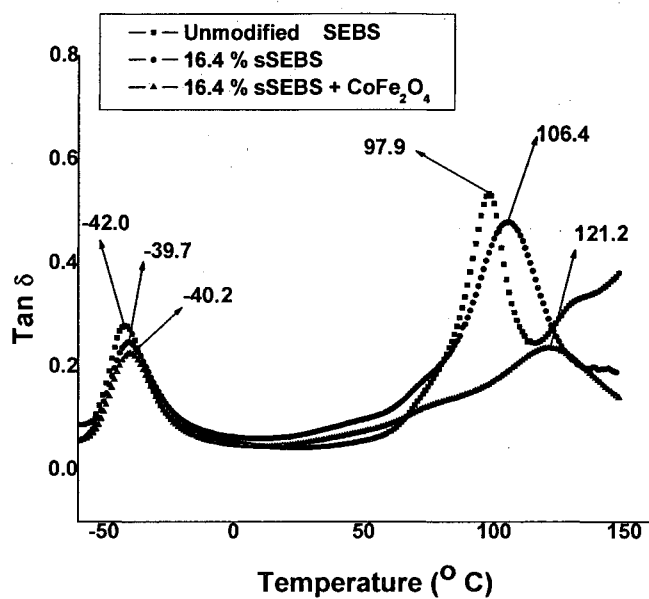


Figure IV-5. Tan δ vs. T curves for unmodified SEBS, 16.4% sSEBS and 16.4% sSEBS incorporating CoFe₂O₄.

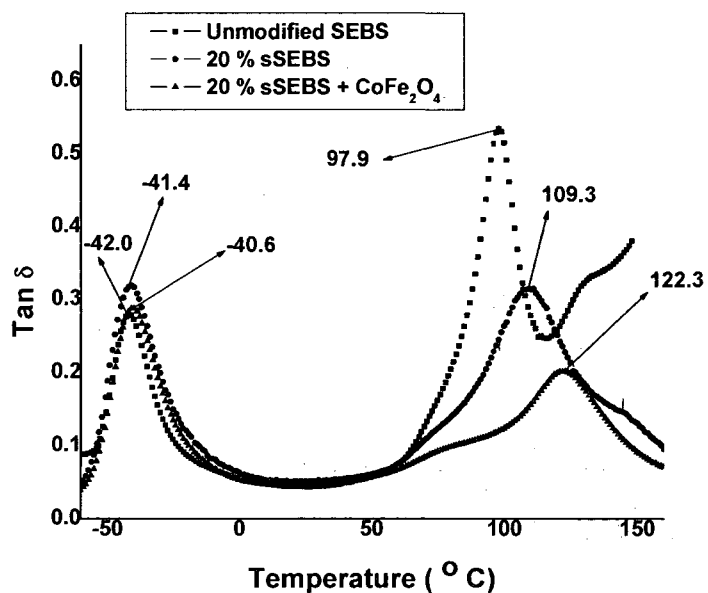


Figure IV-6. Dynamic mechanical tan δ vs. T curves for unmodified SEBS, 20% sSEBS and 20.0% sSEBS incorporating CoFe₂O₄.

Table IV-2. T_g (tan δ peak temperature) for EB and PS block domains after sulfonation and after subsequent cobalt ferrite incorporation.

	T_g (EB) ° C	T_g (S) ° C
SEBS	-42.0	97.9
16.4% _s SEBS	-39.7	106.4
16.4% _s SEBS+CoFe	-40.2	121.2
20.0 % _s SEBS	-41.4	109.3
20.0 % _s SEBS+CoFe	-40.6	122.3

It is seen in Table IV-2 that T_g for the EB phase increases by a significant amount upon sulfonation to either 16.4 or 20.0 percent and even more by subsequent metal oxide incorporation. This is strong indirect evidence that the particle inclusions do not reside in the rubbery phase - as there is no apparent perturbation on segmental motions in these blocks – but rather in the S block domains.

The T_g increase in the hard blocks with sulfonation can be reasonably attributed to constraints on block segmental motions posed by hydrogen bonding interactions between sulfonic acid groups. The further T_g increase with metal oxide incorporation might be accounted for by sulfonate groups experiencing interactions with surface charges on the invasive metal oxide structures. The latter assertion is further supported by the observed suppression of the magnitude of this transition, i.e., area under the tan δ peak, upon sulfonation, and more so by metal oxide incorporation. Another feature of all curves is the broadening of the PS block phase transition with sulfonation, and then further with metal oxide incorporation. This broadening, in a general sense, might reflect a broadening of the environment of the relaxing chain elements by an uneven dispersion of

metal oxide nanostructures as they have grown along the PS block domains. However, the PS block phase T_g is quite the same for the two composites, which is reasonable considering that the two low inorganic uptakes do not differ by much.

The behavior of $\tan \delta$ at the highest temperatures, beyond the PS block phase glass transition, is also affected by these modifications. For one, while the curve for unmodified SEBS undergoes a steep rise, those for the sulfonated and sulfonated - then metal oxide modified samples - turn down. This might diagnose a condition where 'flow' is not possible owing to interactions between sulfonic acid groups as well as interactions with the metal oxide inclusions.

For the unmodified SEBS sample the feature to the right of the peak corresponding to the glass transition for the PS block phase might be, as seen in earlier similar studies, would seem to be an irreversible order-order transition.²³⁻²⁶

The results of magnetic property characterization by the use of alternating gradient magnetometry are as follows. Room temperature curves of magnetization vs. an applied magnetic field that was increased up to 18 kOe for the nanocomposites are displayed in Figure IV-7.

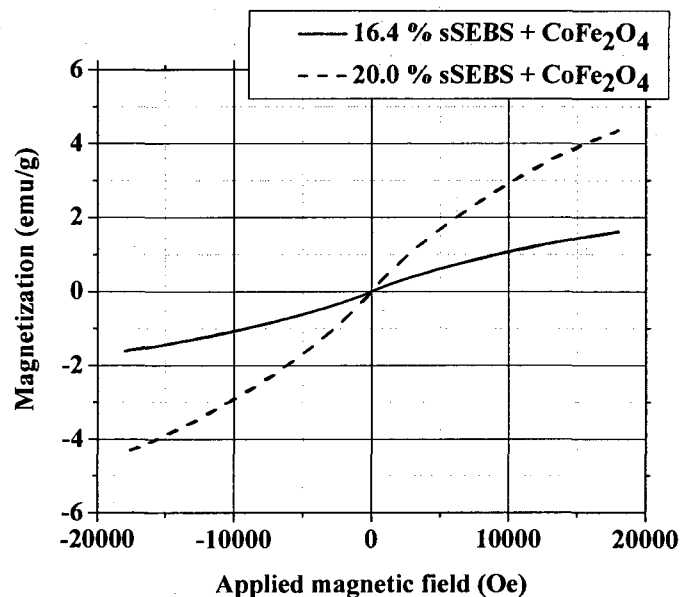


Figure IV-7. Room temperature AGM scans of magnetization (in electromagnetic units [emu]/g) vs. applied magnetic field (in Oersted = Oe) for sSEBS/CoFe₂O₄ nanocomposites having the indicated SEBS sulfonation percents.

The 20% sSEBS curve rises significantly above that for 16.4% sulfonation over the tested range of applied field, which is interesting considering the slight difference in inorganic uptake. Perhaps, the difference resides in electrostatic interactions with SO₃⁻ groups - there being more per unit volume in 20% sSEBS - and charges on the surfaces of cobalt ferrite nanoparticles. In any case, the magnetization does not saturate, i.e., has not reached an asymptote at the highest tested applied field of 18 kOe and there is no coercivity (H_c) at this temperature. As the curve for the 16.4% sSEBS/CoFe₂O₄ sample bends downward more, saturation would be expected at a lower applied field and there is no coercivity, which is characteristic of superparamagnetism.⁵ The critical size for cobalt ferrite nanoparticles, above which they are ferri- or ferromagnetic and beneath which they are superparamagnetic, is ~14 nm.²² This is viewed as a transition from multi- to single magnetic domain character when particle size is reduced beneath this critical size

owing to minimal free energy considerations involving domain walls. More specifically, sizes of 22.5 and 28 nm were observed for particles in the 16.4 and 20.0% sSEBS/cobalt ferrite nanocomposites, respectively. The nanoparticles in this work are above this critical size for superparamagnetism but the test temperature is above the blocking temperature, T_B , as discussed below. 14 nm should be considered as an approximate, hypothetical value based on a simple equation that does not incorporate chemical details. T_B is related to particle size through the equation, $T_B = KV/25k_B$, where K is the anisotropy constant, k_B is the Boltzmann constant, and V is the particle volume,^{18,27-30} For $T < T_B$ magnetic moments are thermally frozen and above T_B they are free to align along the applied field direction.^{31,32}

From the TEM images in Figures 2 and 3, the morphology of 16.4 % sSEBS + CoFe_2O_4 is observed, whereas for 20% sSEBS + CoFe_2O_4 the morphology is not apparent. The particle size in both the samples is the same at ~ 20 nm. And saturation magnetization (M_s) for 16.4 % sSEBS + CoFe_2O_4 is 1.61 emu/g whereas for 20 % sSEBS + CoFe_2O_4 it is 4.56 emu/g. The increase in magnetization can be related to two facts: the nature of the host material (block copolymer) and inter-particle distances. When magnetic nanoparticles are dispersed in a diamagnetic host media, the resultant magnetic nature of the composite materials is composed of the individual magnetic characteristics which will also be influenced by inter-particle distances and how well the particles are dispersed. If the nanoparticles are dispersed such that the distances between them are great the interactions between magnetic moments will be small; and the diamagnetic polymeric media makes these interactions negligible which makes the magnetic response superparamagnetic.³³⁻³⁶

The ZFC and FC plots for the 20.0% sSEBS/cobalt ferrite sample that were generated using SQUID are shown in Figure IV-8.

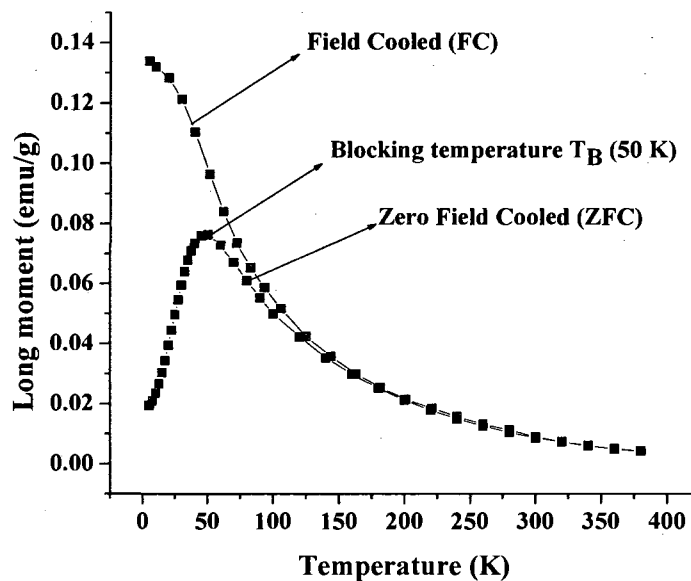


Figure IV-8. ZFC and FC plots for [20.0% sSEBS]/CoFe₂O₄ obtained using SQUID.

The ZFC curve was used to determine the blocking temperature, T_B , which is the temperature corresponding to the peak maximum which, in this case, is 50 K. Below 50 K, the particles behave in ferromagnetic manner and above 50K they are superparamagnetic. Owing to the fact that the hysteresis measurements using AGM were done at room temperature (300 K), which is well above T_B , all magnetic moments are thermally mobile and randomly aligned at room temperature which accounts for the lack of hysteresis.

The peak on the ZFC curve is broad, which suggests that there is a considerable range of particle size and this can be clearly observed in the TEM images.

Conclusions

Cobalt ferrite nanoparticles were grown in partially sulfonated poly (styrene-ethylene/butylene-styrene) phase separated block copolymers *via* an *in-situ* precipitation method. Thermogravimetric analysis indicated single step degradation and essentially the same inorganic uptake of around 4.5 wt% for both 16.4 and 20.0% degrees of hard block sulfonation.

TEM analysis for both degrees of sulfonation revealed particles having an average size of ~20 nm. At least in the case of 16.4% sSEBS, these particles appear to reside in the inter-domain spacings in the phase separated block copolymer morphology. Further experiments are needed to explore whether this phenomenon is universal. Wide angle ray diffraction results for 20.0% sSEBS showed that the nanoparticles possess an inverse spinel cobalt ferrite structure. Using dynamic mechanical analysis, the behaviors of the glass transitions for the hard and soft block phases to sulfonation, and then to cobalt ferrite incorporation, provided indirect evidence that the nanoparticles selectively incorporate in the sSEBS phase.

Magnetization curves generated using an alternating gradient magnetometer showed that these nanocomposites were superparamagnetic at room temperature. Zero-field-cooled and field-cooled curves that were generated using a SQUID magnetometer revealed a blocking temperature of 50K which reinforces the assertion that these nanocomposites possess the property of superparamagnetism at room temperature. The lack of magnetic hysteresis for these nanocomposite materials would make them unsuitable as EM energy absorbing materials because there would be no magnetic

energy loss per cycle. Particles large enough to support domain walls would be needed for this purpose.

Acknowledgements

We acknowledge the National Science Foundation Materials Research Science and Engineering Center, Division of Materials Research (DMR-0213883) for Stimuli Responsive Materials at the University of Southern Mississippi for funding. We also thank Kraton[®] LLC for donating SEBS block copolymers. This work made use of the NSF MRSEC DMR-0213985 Shared Facilities at the University of Alabama for AGM measurements.

References

- (1) Ishino, K.; Narumiya, Y. *American Ceramic Society Bulletin* **1987**, 66, 1469.
- (2) Neelakanta, P. S.; Park, J. C. *IEEE Transactions on Microwave Theory and Techniques* **1995**, 43, 1381.
- (3) Cho, H.-S.; Kim, S.-S. *IEEE Transactions on Magnetics* **1999**, 35, 3151.
- (4) Knott, E. F.; Shaeffer, J. F.; Tuley, M. T. *Radar Cross Section*, 2nd Ed., Scitech, Raleigh, NC, 2004, p. 334.
- (5) Kim, Y. I.; Kim, D.; Lee, C. S. *Physica B: Condensed Matter (Amsterdam, Netherlands)* **2003**, 337, 42.
- (6) Ennas, G.; Casula, M. F.; Falqui, A.; Gatteschi, D.; Marongiu, G.; Marras, S.; Piccaluga, G.; Sangregorio, C. *Journal of Sol-Gel Science and Technology* **2003**, 26, 463.
- (7) Chipara, M.; Hui, D.; Sankar, J.; Leslie-Pelecky, D.; Bender, A.; Yue, L.; Skomski, R.; Sellmyer, D. J. *Composites, Part B: Engineering* **2004**, 35B, 235.
- (8) Davies, K. J.; Wells, S.; Upadhyay, R. V.; Charles, S. W.; O'Grady, K.; El Hilo, M.; Meaz, T.; Morup, S. *Journal of Magnetism and Magnetic Materials* **1995**, 149, 14.
- (9) Moumen, N.; Veillet, P.; Pileni, M. P. *Journal of Magnetism and Magnetic Materials* **1995**, 149, 67.
- (10) Ahmed, S. R.; Ogale, S. B.; Kofinas, P. *IEEE Transactions on Magnetics* **2003**, 39, 2198.

- (11) Godovsky, D. Y.; Varfolomeev, A. V.; Efremova, G. D.; Cherepanov, V. M.; Kapustin, G. A.; Volkov, A. V.; Moskvina, M. A. *Advanced Materials for Optics and Electronics* **1999**, *9*, 87.
- (12) Cendoya, I.; Lopez, D.; Alegria, A.; Mijangos, C. *Journal of Polymer Science, Part B: Polymer Physics* **2001**, *39*, 1968.
- (13) Lopez, D.; Cendoya, I.; Torres, F.; Tejada, J.; Mijangos, C. *Journal of Applied Polymer Science* **2001**, *82*, 3215.
- (14) Li, X. G.; Takahashi, S.; Watanabe, K.; Kikuchi, Y.; Koishi, M. *Nano Letters* **2001**, *1*, 475.
- (15) Rajan, G. S.; Mauritz, K. A.; Stromeyer, S. L.; Kwee, T.; Mani, P.; Weston, J. L.; Nikles, D. E.; Shamsuzzoha, M. *Journal of Polymer Science, Part B: Polymer Physics* **2005**, *43*, 1475.
- (16) Rajan, G. S.; Stromeyer, S. L.; Mauritz, K. A.; Miao, G.; Mani, P.; Shamsuzzoha, M.; Nikles, D. E.; Gupta, A. *Journal of Magnetism and Magnetic Materials* **2005**, *299*, 211.
- (17) Mauritz, K. A.; Blackwell, R. I.; Beyer, F. L. *Polymer* **2004**, *45*, 3001.
- (18) O'Handley, R. C. *Modern Magnetic Materials: Principles and Application*; 1999.
- (19) Blaskov, V.; Petkov, V.; Rusanov, V.; Martinez, L. M.; Martinez, B.; Munoz, J. S.; Mikhov, M. *Journal of Magnetism and Magnetic Materials* **1996**, *162*, 331.
- (20) Pillai, V.; Shah, D. O. *Journal of Magnetism and Magnetic Materials* **1996**, *163*, 243.
- (21) Moumen, N.; Pileni, M. P. *Journal of Physical Chemistry* **1996**, *100*, 1867.
- (22) Hoh, J. C.; Yaacob, I. I. *Journal of Materials Research* **2002**, *17*, 3105.

- (23) Blackwell, R. I.; Mauritz, K. A. *Polymer* **2004**, 45, 3457.
- (24) Weiss, R. A.; Sen, A.; Willis, C. L.; Pottick, L. A. *Polymer* **1991**, 32, 1867.
- (25) Joint Committee on Powder Diffraction Standards, Powder Diffraction File 22-1086 (Cobalt Ferrite, CoFe_2O_4).
- (26) Weiss, R. A.; Sen, A.; Pottick, L. A.; Willis, C. L. *Polymer* **1991**, 32, 2785.
- (27) Chikazumi, S. *Physics of Magnetism*; New York: John Wiley; 1964.
- (28) Cullity, B. D. *Introduction to Magnetic Materials*; Addison-Wesley Publishers: 1972.
- (29) Spaldin, N. A. *Magnetic Materials: Fundamentals and Device Applications*; New York: Cambridge University Press; 2003.
- (30) Zhang, X. X.; Hernandez, J. M.; Tejada, J.; Ziolo, R. F. *Physical Review B: Condensed Matter* **1996**, 54, 4101.
- (31) Leslie-Pelecky, D. L.; Rieke, R. D. *Chemistry of Materials* **1996**, 8, 1770.
- (32) Vassiliou, J. K.; Mehrotra, V.; Russell, M. W.; Giannelis, E. P.; McMichael, R. D.; Shull, R. D.; Ziolo, R. F. *Journal of Applied Physics* **1993**, 73, 5109.
- (33) Dormann, J. L.; Fiorani, D.; Tronc, E. *Advances in Chemical Physics* **1997**, 98, 283.
- (34) Chantrell, R. W.; Coverdale, G. N.; El Hilo, M.; O'Grady, K. *Journal of Magnetism and Magnetic Materials* **1996**, 157/158, (European Magnetic Materials and Applications Conference, 1995), 250-255.
- (35) Mamiya, H.; Nakatani, I.; Furubayashi, T. *Physical Review Letters* **1998**, 80, 177.

- (36) Dormann, J. L.; D'Orazio, F.; Lucari, F.; Tronc, E.; Prene, P.; Jolivet, J. P.; Fiorani, D.; Cherkaoui, R.; Nogues, M. *Physical Review B: Condensed Matter* **1996**, *53*, 14291.

CHAPTER V

MORPHOLOGY AND MAGNETIC PROPERTIES OF SULFONATED POLY
[STYRENE-(ETHYLENE/BUTYLENE)-STYRENE]/ IRON OXIDE COMPOSITES

Abstract

Iron oxide particles were grown in the sulfonated polystyrene block domains of poly [styrene-(ethylene/butylene)-styrene] block copolymers *via* a domain targeted *in-situ* precipitation method. The crystal structure of these nanoparticles was determined by wide angle X-ray diffraction and selected area electron diffraction on a transmission electron microscope (TEM). TEM revealed that for less sulfonated SEBS (10 mole % sSEBS), the particles were aggregated with a size range of 100-150 nm whereas for high sulfonation (16 and 20 mole % sSEBS), they were needle-like structures with a length and width of 200-250 nm and 50 nm, respectively. Dynamic mechanical analysis results suggest that iron oxide nanoparticle growth takes place specifically in sulfonated polystyrene block domains. The magnetic properties these nanocomposites was probed with a superconducting quantum interference device magnetometer at 5 and 150 K as well as with an alternating gradient magnetometer at 300 K. The materials exhibited superparamagnetism at 150 K and 300 K and ferrimagnetism at 5 K.

Introduction

Styrene based block copolymers (BCP) can be used as nanoreactor matrices by rendering polystyrene (PS) block domains polar group through their sulfonation. For example, Mauritz *et al.*¹⁻⁴ created metal alkoxide nanostructures in these sulfonated PS domains using in situ sol-gel chemistry and studied their effect on the morphology of the final nanocomposites. The main advantage of this bottom-up self assembly process is to

create nanostructures without aggregation and better particle dispersion than in conventional mixing methods.⁵

Guru *et al.*^{6,7} used pre-formed, sulfonated (s) poly [(styrene)-(ethylene/butylene)-(styrene)] (SEBS) films as a growth medium for cobalt ferrite and other metal oxide nanoparticles *via* an *in-situ* precipitation method. The synthesized cobalt ferrite nanoparticles were spherical in shape and having different sizes at two different reaction times. It was also reported that these metal oxide nanoparticles exhibited magnetism depending on the temperature.

A macroscopic magnetic material is viewed as an array of small magnetic domains separated by domain walls. Magnetic domains, in turn, consist of fundamental magnetic moments (e.g., electron spin, orbit) all oriented in same direction.⁸⁻¹¹ When a macroscopic magnetic material, that is ferrimagnetic or ferromagnetic, is divided into particles below the size of a critical single domain (SD) it can no longer exhibit magnetic hysteresis due to domain wall motion and the system becomes superparamagnetic. For example, the critical single domain size for magnetite and maghemite are 128 and 166 nm, respectively.¹² For iron oxide systems, the critical superparamagnetic size is reported to be approximately below 20 nm, i.e., nanoscopic.¹³

Oxides such as maghemite, cobalt ferrite (generally of the type $MO \cdot Fe_2O_3$, cubic) and barium ferrite ($MO \cdot 6Fe_2O_3$, hexagonal) are ferrimagnetic. Bulk maghemite ($\gamma-Fe_2O_3$) is ferrimagnetic at room temperature with a saturation magnetization (M_s) and coercivity (H_c) of about 80 emu/g and 250–450 Oe, respectively. Magnetite (Fe_3O_4) is ferrimagnetic with values of ~ 92 emu/g and ~ 350 Oe, respectively. A polymorph of maghemite is hematite ($\alpha-Fe_2O_3$), which is of the hexagonal corundum structure and is

parasitic or canted antiferromagnetic.¹⁴ Maghemite is only a metastable, low temperature Fe_2O_3 structure and the phase transition to the α form can take place above 300°C .¹⁵

Detailed analyses of other types of iron oxides and oxyhydroxides such as: η -, ϵ -, and β - Fe_2O_3 and FeO and FeOOH (its different forms such as α -, β -, γ -, and δ), which have different crystal structure and magnetic properties are in the literature.¹⁶⁻³²

In principle, the magnetic properties of these nanomaterials can be studied and fine tuned by manipulating the chemistry of preparation.

Here, we report the preparation and characterization of magnetic nanocomposites created by the precipitation of iron oxide nanoparticles in preformed sulfonated SEBS phase separated templates. The size of the nanoparticles was determined using TEM and crystal structure was probed using wide angle X-ray diffraction. The inorganic mass uptake was determined using thermogravimetric analysis. Changes in glass transition temperatures, as related to morphology, were determined using dynamic mechanical analysis. Magnetic properties were studied using an alternating gradient magnetometer and a superconducting quantum interference device magnetometer.

Experimental

Materials

The commercial SEBS block copolymer, Kraton[®], G 1652 grade with $M_n = 73,600\text{ g mol}^{-1}$ and having ~30% styrene composition, was obtained from Kraton[®] LLC. Toluene, 1, 2-dichloroethane (DCE), 1-hexanol, acetic anhydride, sulfuric acid (H_2SO_4), dimethyl acetamide (DMAc), anhydrous ferric chloride (FeCl_3), and sodium hydroxide were obtained from Fisher Co. All reagents were used without further purification.

Sulfonation Reaction

Sulfonation of SEBS was performed according to a procedure reported elsewhere,⁴⁻³³ Here, samples were prepared with three different levels of sulfonation up to 20% by mole. The three sulfonated samples are labeled as follows: 10 mole % sulfonated SEBS = 10SEBS, 16 mole % sulfonated SEBS = 16SEBS, and 20 mole % sulfonated SEBS = 20SEBS. Films of these samples were cast from toluene and hexanol solutions into Teflon[®] Petri dishes with a thickness of around 1 mm. The films were dried at 45° C under N₂ for 7d to remove solvents and then annealed at 120° C for 2d under vacuum.

Metal Oxide Incorporation

Pre-formed films having these sulfonation levels were swollen in DMAc for 48h and constantly shaken. A 3.0 M solution of FeCl₃ in DMAc was prepared and the swollen films were submerged in these solutions separately for 48h in a shaker. The samples were taken out and surface wiped with tissue paper to minimize surface precipitation. These metal chloride-doped samples were then washed with DI water several times to leach out excess electrolyte. In the final step, each of the three samples was placed in a freshly prepared 2 M NaOH solution for 48h and washed with DI water continuously for 48h and the water was monitored from time to time to replace the basic water with fresh water to leach out excess Na⁺ ions. After washing, samples were dried in an oven for 48h at 120° C to remove excess solvents and water.

Material Characterization

Composite morphology was inspected using TEM. Samples were cryo-microtomed with a Leica UC FC6. The microtome chamber, sample, and knife were

maintained at -75°C . At least 3 thin sections of ~ 80 nm were obtained for each sample and placed on a copper grid. Morphology was observed by using a JEOL JEM-2100 LaB6 operating at 200 KeV. The crystalline nature of nanoparticles was observed with the same microscope in select area electron diffraction (SAED) mode. Crystal structures of metal oxide particles were studied using a Rigaku Ultima III X-Ray diffractometer using a wavelength ($\text{CuK}_{\alpha 1}$ radiation) of 1.54 \AA . A continuous scan ranging between 15 and 75° was performed. JadeTM graphical analytical software was used to find the peak positions, relative intensity and full-width-at-half-maximum (FWHM) of the main peak and its 2θ angular position.

Thermogravimetric analysis (TGA) was performed using a TA instruments TGA model Q50. Samples were heated from 30 to 700°C at $10^{\circ}\text{C}/\text{min}$ under nitrogen atmosphere. Dynamic mechanical analysis (DMA) was performed for each metal oxide containing sBCP and its unmodified BCP control to observe the shift of the glass transition temperatures (T_g) for both the EB and PS (and sPS) block phases before and after metal oxide incorporation. Two trials were performed for each sample to confirm reproducibility of the TGA and DMA experiments, which was indeed the case.

Magnetic measurements of sSEBS/iron oxide samples were performed using a Quantum Design Model MPMS SQUID magnetometer with helium cryostat. Zero field cooled (ZFC) measurements were performed by inserting the sample into the Dewar with the magnetic field set to zero. The temperature was lowered to 5 K and stabilized at this temperature for 15 min with no applied field. ZFC measurements were then carried out by applying a magnetic field; in this case two different fields (50 and 100 Oe) were applied for each sample separately to study the effect of applied field. Magnetization was

measured at this applied field and at each measurement point the system was equilibrated. Measurements were conducted from 5 to 300 K at 5 K increments. For the FC measurements, the system was stabilized at 300 K for 15 min at specified fields (50 and 100 Oe) and measurements were taken at each 5 K decrement until the system reached 5K. Magnetization vs. applied field curves were determined at 5, 150 K for all three samples. The measured magnetization values were divided by the total mass of iron oxide content in sPS block determined from TGA analysis.

Room temperature magnetic measurements were performed using a MicroMag™ Mode alternating gradient magnetometer (AGM, Princeton Measurement Corp.) Films were weighed prior to measurement and mounted on a piezoelectric transducer which oscillates when the sample is subjected to an alternating gradient magnetic field. The alternating field was decreased from 18 kOe to -18 kOe in steps of 100 Oe and increased back to 18 kOe. The magnetization values were divided by the total mass of inorganic oxide content in sPS block determined from TGA analysis.

Results and Discussion

Sample Analysis

Mole percent sulfonation was determined for each sample prior to film casting using a standard titration method described elsewhere and the values obtained differed from elemental analysis by only 2%.³⁴ Metal ion incorporation was performed according to a procedure described elsewhere.³⁵ DMAc was chosen as a solvent because it selectively swells the sulfonated PS block domains, which promotes the incorporation of metal ions followed by the synthesis of metal oxide particles atom-by-atom in subsequent steps in the sPS block domains.

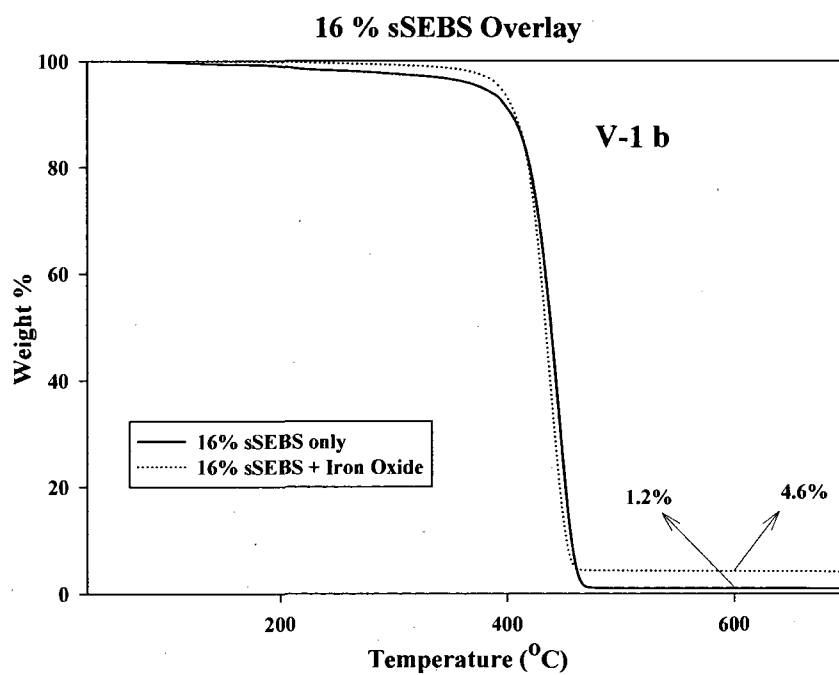
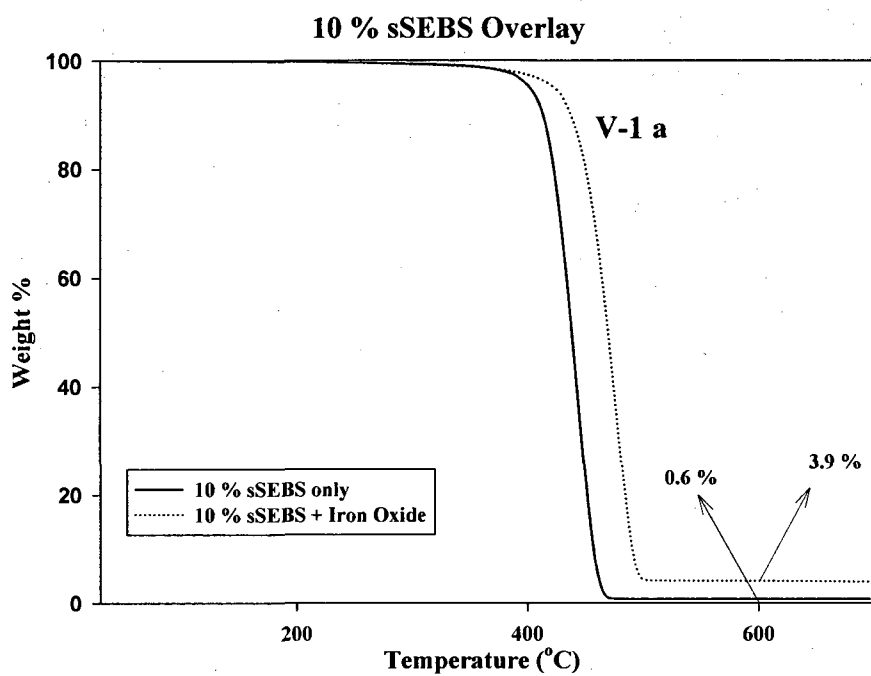
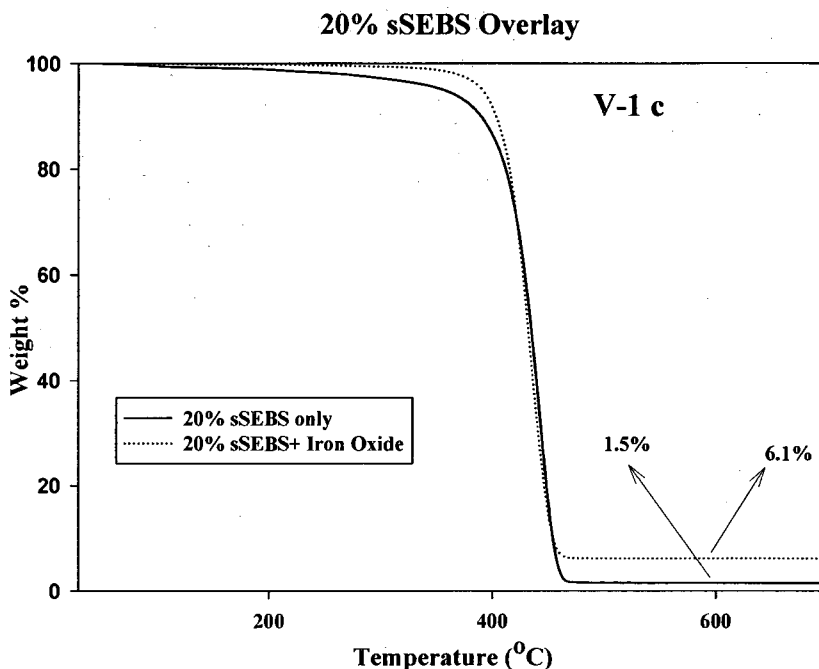


Figure V-1 (a-c). TGA scans of 10SEBS/iron oxide, 16SEBS/iron oxide and 20SEBS/iron oxide, respectively.



Figures V-1 a, b and c show TGA curves for 10SEBS/iron oxide, 16SEBS/iron oxide and 20SEBS/iron oxide respectively. Inorganic oxide content is expressed as weight percent remaining at 600°C by subtracting the char at the same temperature from that of its unloaded sBCP sample. The iron oxide uptakes were 3.3, 3.6 and 4.6 wt % respectively for samples in the same order. Iron oxide uptake increases somewhat with increase in percent mole sulfonation in the BCP under the same reaction and *in-situ* precipitation conditions. Moreover, it is seen that these inclusions increase thermal degradation stability.

Morphology

A wide angle x-ray diffraction (WAXD) pattern for a 10SEBS/iron oxide nanocomposite film is shown in Figure V-2. The Miller indices (hkl) for the peaks for this sample listed in Table V-1 match those of the α -Fe₂O₃ (hematite) unit cell.³⁶ Specific

peaks for α -Fe₂O₃ are labeled in Figure V-1 and the d-spacings and FHTM values were obtained from Jade™ Graphic Analysis software.

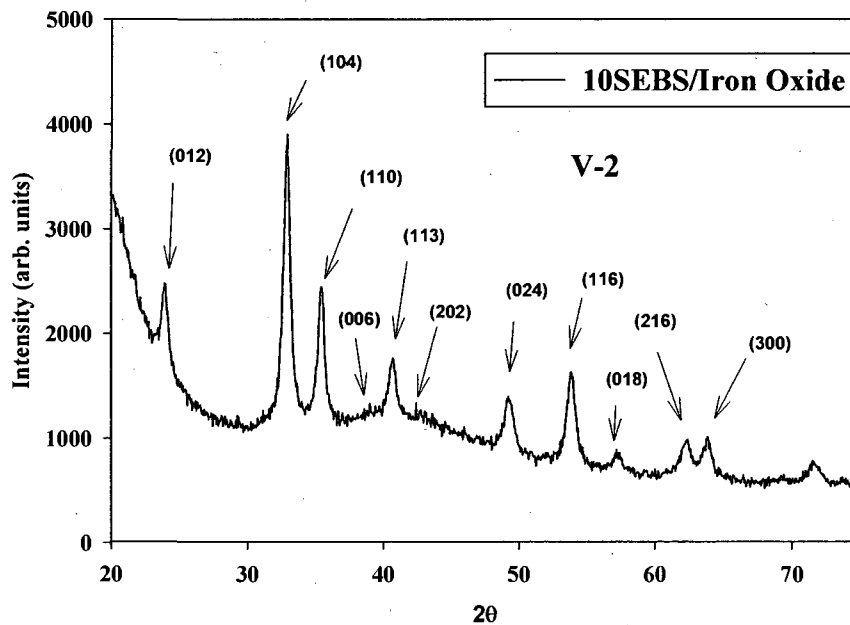


Figure V-2. WAXD scan for the 10SEBS/iron oxide nanocomposite having 3.3 wt% iron oxide filler. Miller indices of prominent reflections are indicated.

Table V-1. Bragg spacings and Miller indices for 10SEBS/iron oxide sample

2θ	d (Å)	(h k l)
23.9	3.712	(0 1 2)
32.9	2.720	(1 0 4)
35.4	2.530	(1 1 0)
39.3	2.291	(0 0 6)
40.7	2.215	(1 1 3)
49.2	1.850	(0 2 4)
53.8	1.702	(1 1 6)
57.1	1.610	(1 2 2)
62.4	1.487	(2 1 4)
63.8	1.456	(3 0 0)

Approximate particle sizes were calculated from the Scherrer equation:^{9,37} $D = (0.9)\lambda / (\text{FWHM} \times \cos \theta)$, where D = particle size, λ = wavelength of incident x-rays ($\text{CuK}_{\alpha 1}$) = 1.54 Å and θ is one-half the diffraction angle 2θ . The Scherrer equation was applied to all the peaks listed in the Table and yielded the same particle size with less than < 5 % error. This particle size was 28 nm, which is in the range of inter-domain spacings of styrene-based block copolymers.^{3,38}

Figure V-3 a is a TEM micrograph of a 10SEBS/iron oxide sample. Most of the features appear as clusters of smaller particles that have sizes 100-150 nm, the lowest particle size being ~10 nm. The inset of Figure V-3 a is a SAED pattern of a single nanoparticle in a cluster which shows short arcs corresponding to various crystal scattering planes. The five main intense arcs correspond to the unit cell structure of $\alpha\text{-Fe}_2\text{O}_3$. Figures V-3 b and c are TEM micrographs of the 16SEBS/iron oxide and 20SEBS/iron oxide composites, respectively. In Figure V-3 b, the particle shape is needle-like with a length of 200-250 nm and width of 50 nm. These needles appear to be monolithic and do not form clusters. In Figure V-3 c the iron oxide in the 20 mole % sulfonated SEBS matrix also forms needles with lengths 200-225 nm with a width of 50 nm, and no aggregation. SAED patterns for both Figures 3b and c are in the inset and single crystal patterns are observed. The in-plane lattice dimensions of these single crystal structures were $a = 0.4754$ and $c = 1.299$ nm with rhombohedral symmetry.^{36,39} The unit cell dimensions obtained from SAED differed from reported values by 6% but, as per earlier literature, this mismatch is considered acceptable.⁴⁰

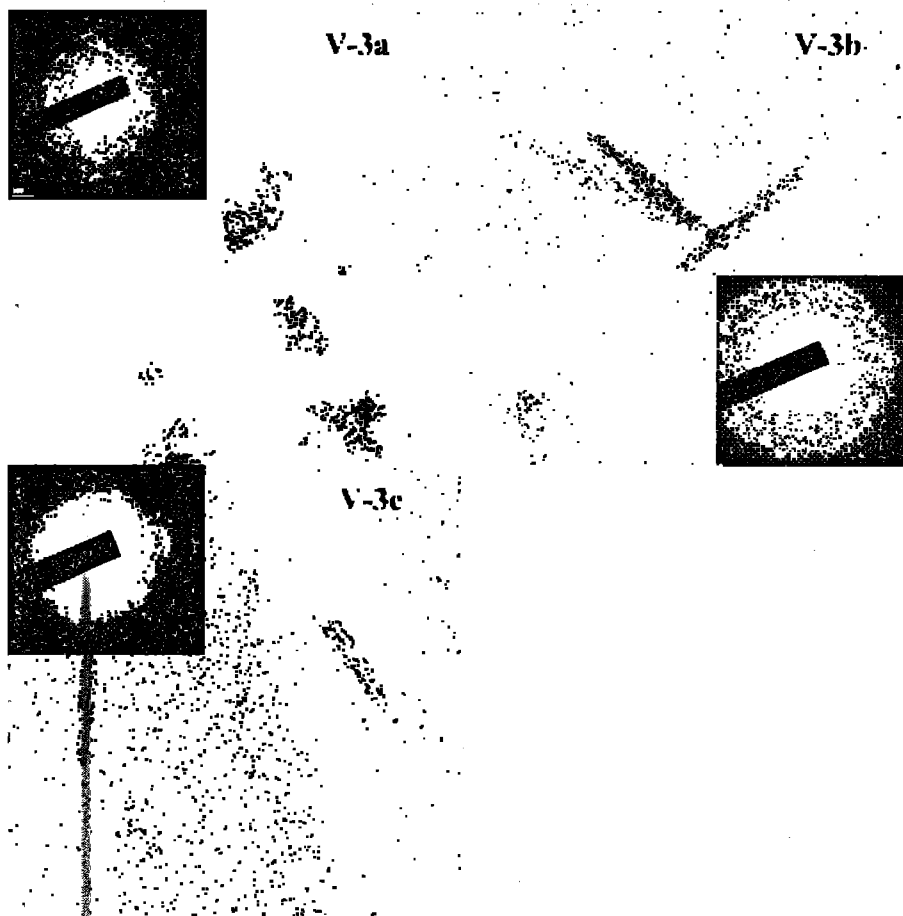


Figure V-3 (a-c). TEM micrographs of 10SEBS/iron oxide, 16SEBS/iron oxide and 20SEBS/iron oxide, respectively. The image insets are SAED diffraction patterns of iron oxide crystalline structures.

DMA studies were performed on each sample to detect changes in the PS and EB block domain glass transition temperatures (T_g) before and after incorporating the iron oxide nanoparticles. Figures V-4 a, b and c show $\tan \delta$ vs. temperature for the three samples and, for comparison, the results for unsulfonated SEBS (0SEBS). T_g for both block domains, before and after sulfonation, and iron oxide incorporation, are listed in Table V-2. The lowest EB block T_g is that for 0SEBS and the value progressively increases, although by small degrees with increase in sulfonation. This might be viewed as being due to the formation of strong- SO_3H interactions between adjacent chains in the hard block domains, a sort of enhanced crosslinking.³³

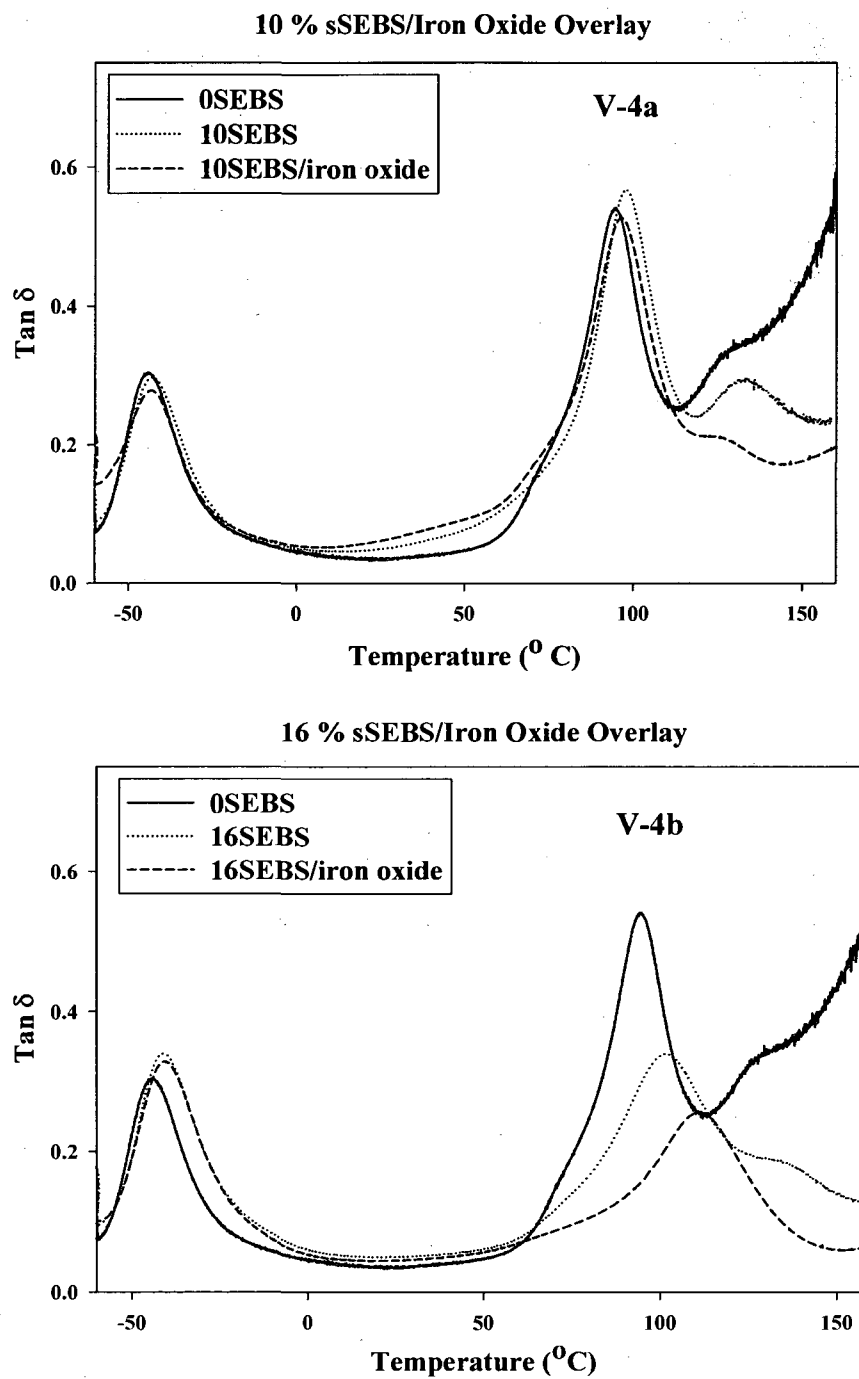


Figure V-4. $\tan \delta$ vs. T for (a) 10SEBS/iron oxide, (b) 16SEBS/iron oxide and (c) 20SEBS/iron oxide, respectively.

20 %sSEBS/Iron Oxide Overlay

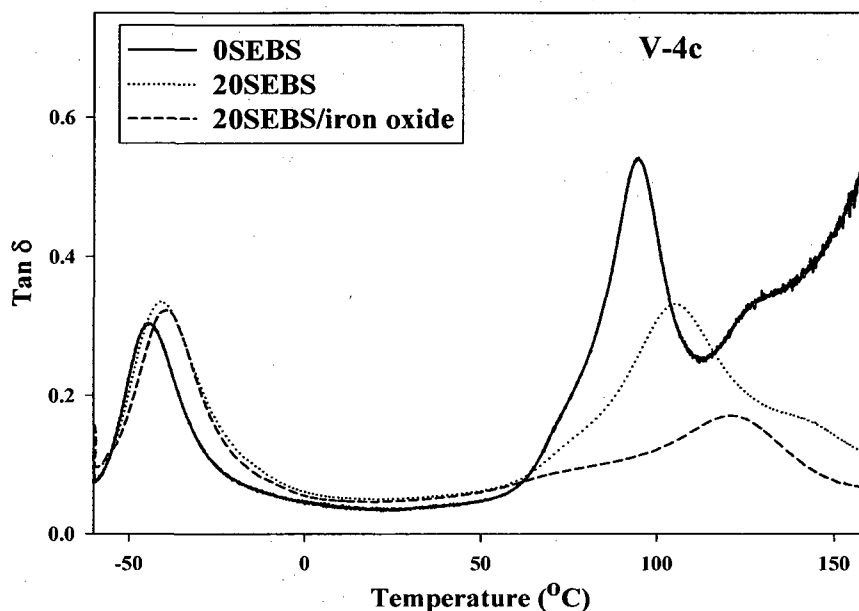


Table V-2. Glass transition temperatures for the ethylene-butylene and styrene block domains for unmodified SEBS, sulfonated (s) SEBS and sSEBS containing iron oxide.

Sample ID	T_g of EB block ($^{\circ}\text{C}$)	T_g of PS(sPS) block ($^{\circ}\text{C}$)
0SEBS	-44.3	94.5
10SEBS	-43.0	97.9
10SEBS/iron oxide	-43.0	96.7
16SEBS	-40.9	102.0
16SEBS/iron oxide	-40.4	111.9
20SEBS	-40.5	105.6
20SEBS/iron oxide	-39.0	121.5

The T_g of PS blocks increased monotonically, and more significantly, after sulfonation by about 11 $^{\circ}\text{C}$ over the entire range, which is reasonable considering that hydrogen bonding SO_3H groups were introduced in these regions.

After iron oxide incorporation, T_g of the sulfonate blocks was increased by 9.9 and 15.9 $^{\circ}\text{C}$ for 16SEBS/iron oxide and 20SEBS/iron oxide, although the change for 10SEBS was negligible. There were essentially no changes in the EB block domains.

This result is indirect evidence that iron oxide nanoparticles preferentially grow in the sPS block domains although there are particles that exceed the inter-domain spacings.

Finally, the sulfonated – but not filled – samples have a transition above T_g for the sPS block phase. This has been described earlier in terms of sPS subdomains that consist of SO_3H group aggregates.^{33,34,38}

ZFC and FC curves for all three samples were measured at magnetic field strengths of 50 and 100 Oe and are displayed in Figures V-5 a, b and c. The temperature corresponding to the peak on a ZFC curve gives the blocking temperature (T_B) above which the magnetic moments are thermally randomized. The effect of applied field on T_B was studied by comparing ZFC and FC curves at two different fields. The ZFC curves exhibit a peak which gives T_B and the width of this peak reflects the distribution of magnetic domain and particle sizes. Below T_B , the material is ferrimagnetic or ferromagnetic i.e., exhibits magnetic hysteresis on applied magnetic field cycling between positive and negative values. For $T > T_B$, the material exhibits paramagnetism.

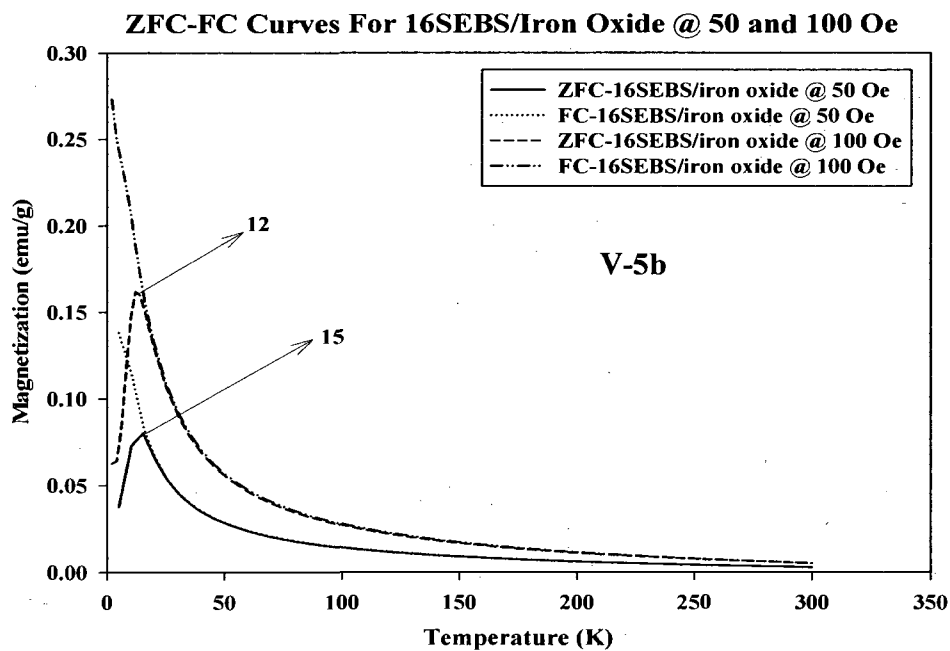
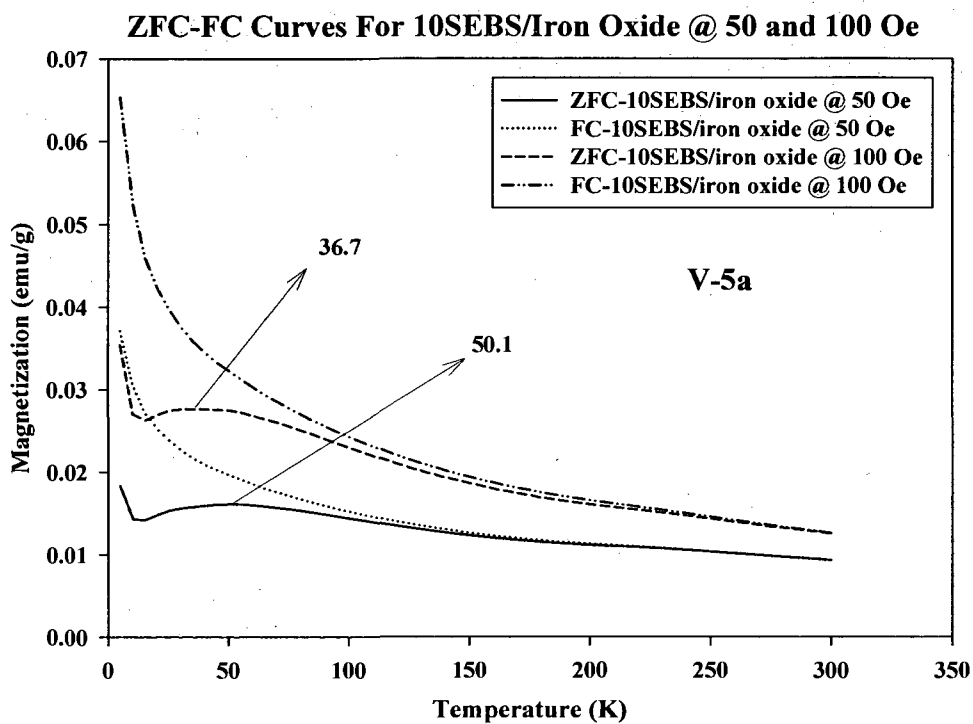
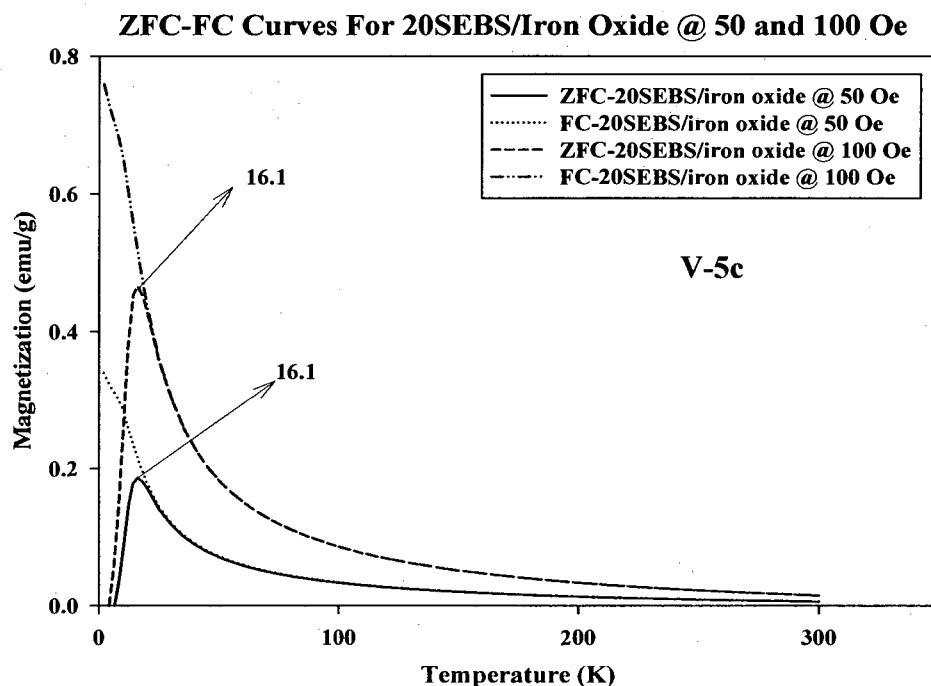


Figure V-5 (a-c). ZFC-FC plots of 10SEBS/iron oxide, 16SEBS/iron oxide and 20SEBS/iron oxide measured at 50 and 100 Oe, respectively.



Nanoparticles that are too small to have domain walls can be superparamagnetic. The convergence of ZFC and FC curves at higher temperatures, and divergence at lower temperatures, is typical for superparamagnetic materials.⁴¹ In Figure V-5 a, the ZFC and FC plots of 10SEBS/iron oxide at 50 and 100 Oe show that T_B at 50 Oe is 50.1 K which is 13.7 K higher than T_B obtained at 100 Oe (36.7 K). This is in conformance with the main property of superparamagnetic particles, namely a decrease of T_B with increase in applied magnetic field. From the ZFC and FC curves for 16SEBS/iron oxide and 20SEBS/iron oxide seen in Figures V-5 b and c, T_B for 16SEBS/iron oxide decreased by 3 K from $T_B = 15$ K at 50 Oe to 12 K at 100 Oe. For 20SEBS/iron oxide $T_B = 16.1$ K was the same for both fields.

The ZFC peak width for 10SEBS/iron oxide is wide at both fields indicating a broad distribution of iron oxide magnetic domains and wide particle size distribution.

The SAED pattern of the same sample shown in Figure V-5 a is in harmony with this wide distribution of particles, which represents the mixture of various crystalline ring arcs including rings related to α -Fe₂O₃. The two ZFC curves of the remaining two samples (16SEBS/iron oxide and 20SEBS/iron oxide) exhibit very narrow and sharp peaks commensurate with very narrow magnetic domain and particle size distributions. The SAED patterns for these samples shown in Figures V-5 b and c confirm that the matrix-incorporated nanoparticles exist as single crystal structures.

TEM micrographs for the same nanocomposites show large aspect ratio monolithic structures, so it would appear that they are single crystals. However, for 10SEBS/iron oxide, the primary particles formed aggregates, which can be understood in terms of a low degree of aggregation of -SO₃H groups. At lower sulfonation levels, the iron oxide nanoparticles grow around these reactive ion exchange sites to form 100-150 nm in size aggregated particles.

Magnetization (M) vs. applied magnetic field (H) curves were obtained for samples incorporating the three iron oxide contents at room temperature (300 K) using AGM. A SQUID magnetometer was used for measurements at 5 and 150 K.

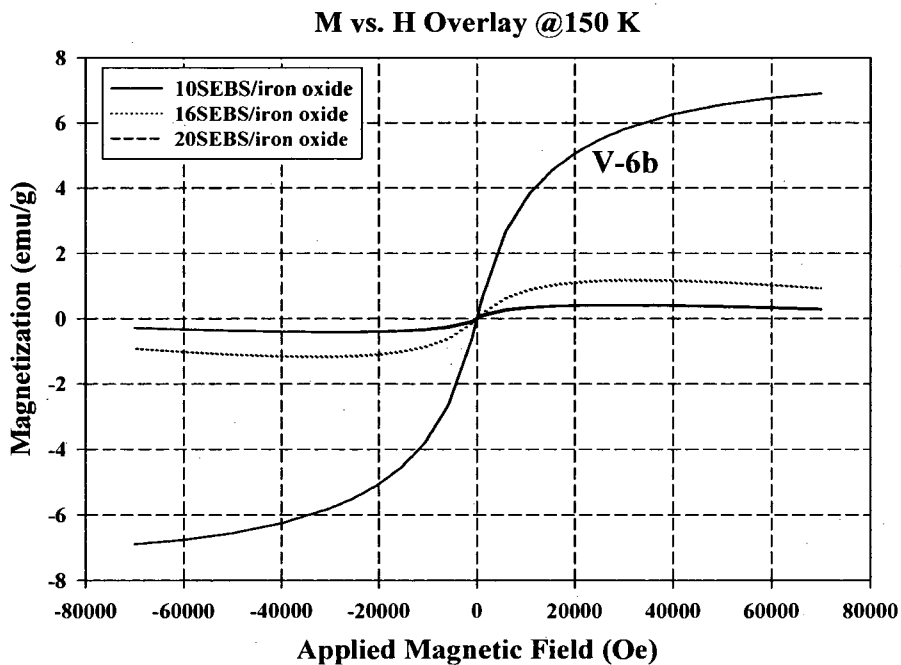
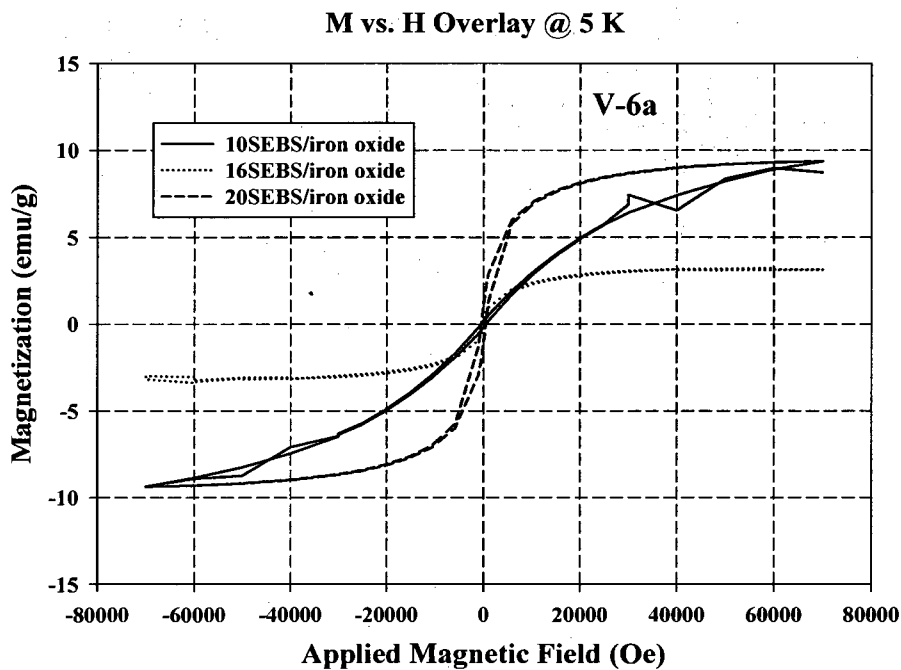
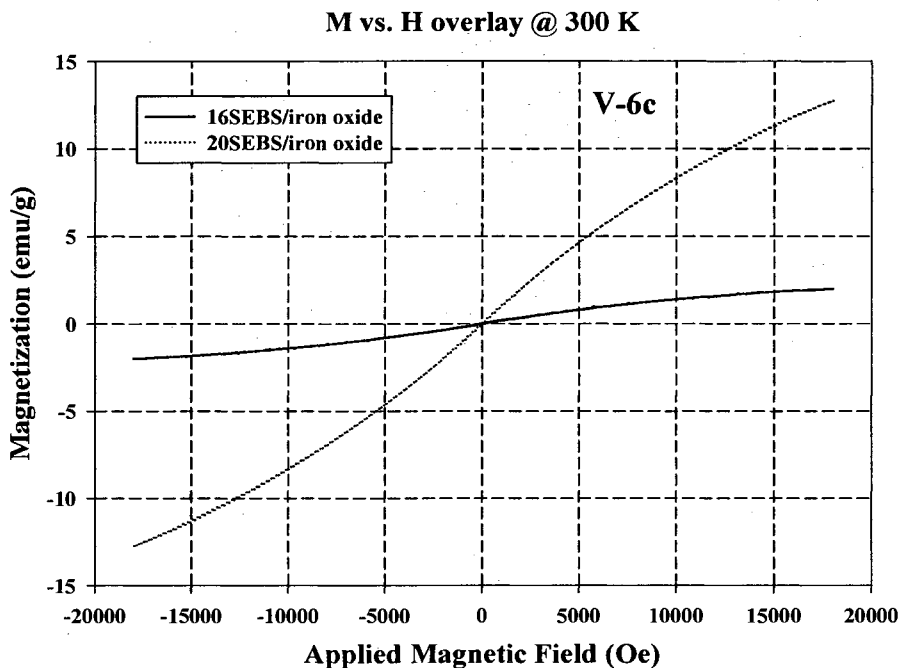


Figure V-6 (a-c). Overlay M vs. H plots measured at temperatures of 5, 150 and 300 K for 10SEBS/iron oxide, 16SEBS/iron oxide and 20SEBS/iron oxide, respectively.



Figures V-6 a and b are M vs. H curves for all three compositions at 5 and 150 K, respectively. At 5 K the coercivities, H_c , (magnetic field required to demagnetize) for 10SEBS/iron oxide, 16SEBS/iron oxide, 20SEBS/iron oxide are 497, 292, and 448 emu/g respectively. For 16SEBS/iron oxide and 20SEBS/iron oxide, the curves saturate at 80 kOe whereas for 10SEBS/iron oxide there is no saturation at this field strength. The three samples show no hysteresis at 150 K which suggests superparamagnetism because the magnetization and demagnetization curves coincide through the origin. The trend of M_s is that 10SEBS/iron oxide shows the lowest value at 0.4 emu/g, that for 16SEBS/iron oxide is 1.2 emu/g and 20SEBS/iron oxide tends towards saturation at 80 kOe. For 10SEBS/iron oxide and 16SEBS/iron oxide, once magnetization reaches M_s , there is a decrease attributed to the diamagnetic character of the polymer matrix. M vs. H curves for 16SEBS/iron oxide and 20SEBS/iron oxide samples at 300 K are shown in Figure V-6(c). The 16SEBS/iron oxide curve saturates at $M_s = 2.1$ emu/g at an applied field of 18

kOe, whereas 20SEBS/iron oxide does not show saturation at 18 kOe. M_s was obtained by plotting magnetization vs. $1/H$ and extrapolating to zero.⁹ M_s thus obtained for 20SEBS/iron oxide is 12.6 emu/g. From M vs. H curves for these three samples at 5, 150 and 300 K, 10SEBS/iron oxide does not saturate at 80 kOe whereas in 16SEBS and 20SEBS there is saturation at 5 K and 150 K. At room temperature, 300 K, iron oxide nanoparticles in the higher sulfonated sample, 20SEBS, do not saturate at 18 kOe whereas the 16SEBS system did. The former might be related to weak surface pinning at the particle surface in the vicinity of $-\text{SO}_3\text{H}$ groups at 5 and 150 K, whereas at 300 K, interactions between the particle and $-\text{SO}_3\text{H}$ groups are strong enough to have a stronger surface pinning effect between the particle surface and polymer interface.^{42,43} It is noted that, at lower temperatures (5 and 150 K), the lower sulfonation sample (10SEBS/iron oxide) exhibits greater surface pinning effects than the higher sulfonation samples. At room temperature (300 K) the higher sulfonation level sample (20SEBS/iron oxide) exhibits a higher greater surface pinning. Surface pinning usually occurs in magnetic nanoparticles dispersed in either fluids or polymer matrices where surface interactions between nanoparticles and the matrix or fluid hinder magnetic moment orientation and/or magnetic domain wall contraction and expansion, with an applied external magnetic field. Perhaps surface interactions between iron oxide nanoparticles and $-\text{SO}_3\text{H}$ groups thermally influence surface pinning effects.

Conclusions

Iron oxide nanoparticles were successfully grown in sulfonated PS domains in an SEBS block copolymer *via* an *in-situ* precipitation method. WAXD analysis indicated that the crystal structure in 10SEBS/iron oxide was $\alpha\text{-Fe}_2\text{O}_3$ (hematite) with an average

particle size of 28 nm which is within the inter-domain spacing value of SEBS block copolymers, suggesting that nanoparticle growth was controlled by the morphology of the block copolymer. TEM micrographs of all three samples showed iron oxide nanoparticles and in the 10SEBS matrix they existed as clusters of 100-150 nm size. The formation of clustered nanoparticles can be understood based on the aggregation of $-\text{SO}_3\text{H}$ groups in the less sulfonated samples. In 16SEBS and 20SEBS matrices, iron oxide nanoparticles exhibited needle-like structures with a length of 200-250 nm and width of 50 nm.

Selected area electron diffraction patterns for nanoparticles in 10SEBS consisted of arcs that matched with $\alpha\text{-Fe}_2\text{O}_3$ (hematite) and in 16SEBS and 20SEBS matrices, iron oxide single crystals were observed with lattice parameters $a = 0.4754$ nm and $c = 1.299$ nm with rhombohedral structure with a 6% mismatch with literature values.

Thermogravimetric analysis determined inorganic uptakes as 3.3, 3.4 and 4.6 wt. % for 10SEBS, 16SEBS and 20SEBS with iron oxide. Dynamic mechanical analysis confirmed the growth of iron oxide nanoparticles occurred mainly in sPS blocks as the T_g of unfilled sSEBS increased with iron oxide incorporation. ZFC and FC studies for all three samples determined the blocking temperature for the iron oxide component at two applied fields. M vs. H curves at 5, 150 and 300 K for these three samples showed that the iron oxide nanoparticles exhibited superparamagnetism at 150 K and 300 K whereas they possessed ferrimagnetism at 5 K with coercivities of 497, 292 and 448 Oe for 10SEBS, 16SEBS and 20SEBS containing iron oxide, respectively.

Acknowledgements

We acknowledge the National Science Foundation Materials Research Science and Engineering Center, Division of Materials Research (DMR-0213883) for Stimuli

Responsive Materials at the University of Southern Mississippi for funding. We also thank Kraton[®] LLC for donating SEBS block copolymers. This work made use of the NSF MRSEC DMR-0213985 Shared Facilities at the University of Alabama for AGM measurements. And for the Work at AMRI/UNO was supported by DARPA through Grant No. HR0011-07-1-0031.

References

- (1) Mauritz, K. A.; Storey, R. F.; Mountz, D. A.; Reuschle, D. A. *Polymer* **2002**, *43*, 4315.
- (2) Mauritz, K. A.; Storey, R. F.; Reuschle, D. A.; Beck Tan, N. *Polymer* **2002**, *43*, 5949.
- (3) Mauritz, K. A.; Blackwell, R. I.; Beyer, F. L. *Polymer* **2004**, *45*, 3001.
- (4) Blackwell, R. I.; Mauritz, K. A. *Polymer* **2004**, *45*, 3457.
- (5) Rajan, G. S.; Sur, G. S.; Mark, J. E.; Schaefer, D. W.; Beaucage, G. *Journal of Polymer Science, Part B: Polymer Physics* **2003**, *41*, 1897.
- (6) Rajan, G. S.; Mauritz, K. A.; Stromeyer, S. L.; Kwee, T.; Mani, P.; Weston, J. L.; Nikles, D. E.; Shamsuzzoha, M. *Journal of Polymer Science, Part B: Polymer Physics* **2005**, *43*, 1475.
- (7) Rajan, G. S.; Stromeyer, S. L.; Mauritz, K. A.; Miao, G.; Mani, P.; Shamsuzzoha, M.; Nikles, D. E.; Gupta, A. *Journal of Magnetism and Magnetic Materials* **2005**, *299*, 211.
- (8) Chikazumi, S. *Physics of Magnetism* New York: John Wiley; 1964.
- (9) Cullity, B. D. *Introduction to Magnetic Materials* Addison-Wesley Publishers; 1972.
- (10) O'Handley, R. C. *Modern Magnetic Materials: Principles and Applications* 1999.
- (11) Spaldin, N. A. *Magnetic Materials: Fundamentals and Device Applications* New York: Cambridge University Press; 2003.
- (12) Klabunde, K. J, Editor. *Nanoscale Materials in Chemistry* 2001.
- (13) Leslie-Pelecky, D. L.; Rieke, R. D. *Chemistry of Materials* **1996**, *8*, 1770.

- (14) Ye, X.; Lin, D.; Jiao, Z.; Zhang, L. *Journal of Physics D: Applied Physics* **1998**, 31, 2739.
- (15) Schimanke, G.; Martin, M. *Solid State Ionics* **2000**, 136-137, 1235.
- (16) Laberty, C.; Navrotsky, A. *Geochimica et Cosmochimica Acta* **1998**, 62, 2905.
- (17) Mitov, I.; Cherkezova-Zheleva, Z.; Mitrov, V. *Physica Status Solidi A: Applied Research* **1997**, 161, 475.
- (18) Chen, L.; Yang, W.-J.; Yang, C.-Z. *Journal of Materials Science* **1997**, 32, 3571.
- (19) Wan, M.; Fan, J. *Journal of Polymer Science, Part A: Polymer Chemistry* **1998**, 36, 2749.
- (20) Sauzedde, F.; Elaissari, A.; Pichot, C. *Colloid and Polymer Science* **1999**, 277, 846.
- (21) Horak, D.; Bohacek, J.; Subrt, M. *Journal of Polymer Science, Part A: Polymer Chemistry* **2000**, 38, 1161.
- (22) Rane, K. S.; Verenkar, V. M. S. *Bulletin of Materials Science* **2001**, 24, 39.
- (23) Millan, A.; Palacio, F. *Applied Organometallic Chemistry* **2001**, 15, 396.
- (24) Radhakrishnan, S.; Saujanya, C.; Sonar, P.; Gopalkrishnan, I. K.; Yakhmi, J. V. *Polyhedron* **2001**, 20, 1489.
- (25) Wormuth, K. *Journal of Colloid and Interface Science* **2001**, 241, 366.
- (26) Gonsalves, K. E.; Li, H.; Santiago, P. *Journal of Materials Science* **2001**, 36, 2461.
- (27) Raming, T. P.; Winnubst, A. J. A.; van Kats, C. M.; Philipse, A. P. *Journal of Colloid and Interface Science* **2002**, 249, 346.
- (28) Chaneac, C.; Tronc, E.; Jolivet, J. P. *Journal of Materials Chemistry* **1996**, 6, 1905.
- (29) Rane, K. S.; Verenkar, V. M. S.; Sawant, P. Y. *Bulletin of Materials Science* **2001**, 24, 331.

- (30) Venkataraman, A.; Hiremath, V. A.; Date, S. K.; Kulkarni, S. D. *Bulletin of Materials Science* **2001**, 24, 617.
- (31) Yen, F. S.; Chen, W. C.; Yang, J. M.; Hong, C. T. *Nano Letters* **2002**, 2, 245.
- (32) Hiremath, V. A.; Venkataraman, A. *Bulletin of Materials Science* **2003**, 26, 391.
- (33) Weiss, R. A.; Sen, A.; Willis, C. L.; Pottick, L. A. *Polymer* **1991**, 32, 1867.
- (34) Blackwell, R. I. Self-Assembled Hybrid Materials Based on Ionomers of Styrene/Ethylene-co-Butylene/Styrene (SEBS): Evolution of Morphology and Rheo-Mechanical Behavior. PhD. Thesis, University of Southern Mississippi, Hattiesburg, MS, May 2004.
- (35) Ahmed, S. R.; Kofinas, P. *Macromolecules* **2002**, 35, 3338.
- (36) Joint Committee on Powder Diffraction Standards, Powder Diffraction File 33-0664 (hematite, α -Fe₂O₃).
- (37) Patterson, A. L. *Physical Review* **1939**, 56, 978.
- (38) Weiss, R. A.; Sen, A.; Pottick, L. A.; Willis, C. L. *Polymer* **1991**, 32, 2785.
- (39) Minhua, C.; Tianfu, L.; Song, G.; Genban, S.; Xinglong, W.; Changwen, H.; Zhong, L. W. *Angewandte Chemie-International Edition* **2005**, 44, 4197.
- (40) Lee, I. J.; Kim, J.-Y.; Yu, C.; Chang, C.-H.; Joo, M.-K.; Lee, Y. P.; Hur, T.-B.; Kim, H.-K. *Journal of Vacuum Science & Technology, A: Vacuum, Surfaces, and Films* **2005**, 23, 1450.
- (41) Ennas, G.; Casula, M. F.; Falqui, A.; Gatteschi, D.; Marongiu, G.; Marras, S.; Piccaluga, G.; Sangregorio, C. *Journal of Sol-Gel Science and Technology* **2003**, 26, 463.
- (42) Coey, J. M. D. *Physical Review Letters* **1971**, 27, 1140.

- (43) Linderoth, S.; Hendriksen, P. V.; Boedker, F.; Wells, S.; Davies, K.; Charles, S. W.; Moerup, S. *Journal of Applied Physics* **1994**, *75*, 6583.

CHAPTER VI

BROADBAND DIELECTRIC SPECTROSCOPIC CHARACTERIZATION
OF SULFONATED POLY [(STYRENE)-(ETHYLENE/BUTYLENE)-STYRENE]/ IRON
OXIDE COMPOSITES GROWN VIA AN IN-SITU PRECIPITATION METHOD

Abstract

Iron oxide nanoparticles were selectively grown in sulfonated (s) polystyrene (PS) domains of poly [(styrene)-(ethylene-co-butylene)-(styrene)] (SEBS) block copolymers via an in-situ precipitation method. The sulfonated samples were analyzed using a Fourier transform infrared spectroscopy and the specific bands confirmed the presence of sulfonic acid ($-\text{SO}_3\text{H}$) groups attached to PS blocks was confirmed. Tapping Mode TM Atomic Force Microscopy measurements on the nanocomposites revealed the presence of the iron oxide nanoparticles grown on the sPS/PS regions. Broad band dielectric relaxation spectroscopy (BDS) studies of unsulfonated, sulfonated and sulfonated samples filled with iron oxide nanoparticles revealed that after the incorporation of inorganic content in blocks (sPS) broadened the α relaxation process (glass transition (T_g) relaxation) on a time scale window in both EB and PS phases. The relaxation times (τ) in both phases were increased at least by an order of magnitude after incorporation of iron oxide nanoparticles. α relaxation process in both EB and PS phases for both sulfonated samples exhibited and non-Arrhenius type of non-linear curvature which is also called as Vogel-Fulcher-Tammann-Hesse (VFTH) behavior. The merging of β and α processes was observed in PS glass transition relaxation region for sulfonated samples and also in sulfonated samples filled with iron oxide after merging temperature and this trend

becomes dominant and the resultant α' relaxation process differed from the original α process by exhibiting Arrhenius type of linear dependence between τ_{\max} vs. T^{-1} curves.

Introduction

Styrene containing block copolymers (BCPs) such as poly[(styrene)-(ethylene-co-butylene)-(styrene)] (SEBS), poly[(styrene)-(butadiene)-(styrene)] (SBS), poly[(styrene)-(isobutylene)-(styrene)](SIBS) and etc., were successfully used as matrices for incorporation of nanoparticles by altering chemical properties of either of the blocks. The mechanical and chemical properties of these BCPs can be improved by partially sulfonating the styrenic blocks which in result, creates thermally reversible physical cross-linking networks.¹ Presence of sulfonated (s) PS chains (hard phase) in the BCP renders them into hydrophilic and the center soft blocks (rubbery phase) acts as hydrophobic, resulting a phase separated system at equilibrium annealing conditions. Mauritz *et al.* were successfully incorporated silica nanostructures in styrenic phase by selective sulfonation of styrenic groups in the backbone in SEBS and SIBS BCPs via Sol-Gel route.²⁻⁴

In case of BCPs, which consists of two different phases (blocks) separated by a considerable difference in dielectric constants, and having a phase separated morphology will be beneficial to observe the enhanced electrical energy dissipation at the inter phases of existing blocks. This occurs due to the mutual imbalance of permanent dipoles which won't cancel each other because of difference in dielectric constants on each side of the interfacial region at interphase.⁵ This energy dissipation depends on the extent of interfacial surface area or surface-to-volume ratio. Higher the ratio higher will be the energy loss. For achieving higher electric energy dissipative materials, surface-to-volume

ratio can be enhanced by adding nanoparticles in already existing phase separated BCPs. The presence of nanoparticles increase the interfacial region between the nanoparticle (a different dielectric constant) and polymer phase.

For microwave range magneto-dielectric and electromagnetic wave interference applications, magnetic nanoparticles can be incorporated in BCP matrices. Many researchers employed conventional blending of nanoparticles into the polymer matrix, but they lack controlling final particle size and prevention of particle aggregation in the final matrix.⁶⁻⁸ Kofinas *et al.* were successfully developed an *in-situ* bottom up process to grow magnetic nanoparticles in hydrophilic block copolymer matrices with controlled particle size.^{9,10} In this current study, we employed the same *in-situ* chemistry to incorporate iron oxide nanoparticles in sulfonated (s) SEBS matrix and dielectric properties of these nanocomposites were studied along with their sulfonated precursor materials.

Broadband Dielectric Spectroscopy (BDS)

BDS is a powerful technique for interrogating macromolecular motions (relaxations) over a vast range of time/distance scales. The basis of the method is the interaction between dipoles and an applied sinusoidal electric field of frequency f . Polymers will have a distribution of relaxation times due to a distribution in chain lengths, and microstructural heterogeneity. Information about sub-glass and glass transitions and phase separation can be probed using BDS.

In amorphous polymers the dynamic process responsible for backbone chain relaxation, termed the α process, is related to the glass transition.¹¹⁻¹⁴ In addition, there is usually another relaxation at a temperature below that of the α transition referred as a

secondary or Johari-Goldstein β (J-G β) process.^{15,16} In case of glass forming polymers, J-G β secondary processes occur due to local in-chain arrangements and side chain mobility whereas the α process is attributed to cooperative motions of the main chain.

Data, in the form of the real and imaginary parts of the complex dielectric constant $\epsilon^* = \epsilon' - i\epsilon''$ was collected at fixed temperatures (T) over a broad range of frequency f . ϵ'' vs. f graphs consist of one or more peaks for each operative relaxation while the ϵ' vs. f graphs usually show monotonically decreasing behavior. The Havriliak-Negami (HN) equation.¹⁷⁻¹⁹ is commonly fitted to permittivity data to extract important parameters related to molecular motions and local molecular environment:

$$\epsilon^*(\omega) = \epsilon' - i\epsilon'' = -i \left(\frac{\sigma_0}{\epsilon_0 \omega} \right)^N + \sum_{k=1}^3 \left[\frac{\Delta\epsilon_k}{(1 + (i\omega\tau_{HN})^{\alpha_k})^{\beta_k}} + \epsilon_{\infty k} \right] \quad \text{Equation 1}$$

Eqn. 1 has the summation of three relaxation terms on the right. The left term accounts for dc conductivity, which, if present, is dominant at low f and high T . ϵ_0 is the permittivity of free space and $\omega = 2\pi f$. $\Delta\epsilon_k = (\epsilon_R - \epsilon_\infty)_k$, is the difference between ϵ' at very low and very high frequencies, respectively. For the d.c. term, σ_0 is the conductivity and the exponent $0 < N \leq 1$ characterizes the conduction process in terms of the nature of charge hopping pathways and charge mobility constraints. The parameters α and β ($0 < \alpha < 1$, $\alpha\beta \leq 1$) characterize the breadth and symmetry, respectively, of ϵ'' vs. ω peaks. τ_{HN} is the Havriliak-Negami relaxation time related to τ_{max} by the following equation [ref.¹⁹, p 64]:

$$\tau_{\max} = \tau_{HN} \left[\frac{\sin\left(\frac{\pi\alpha\beta}{2(\beta+1)}\right)}{\sin\left(\frac{\pi\alpha}{2(\beta+1)}\right)} \right]^{\frac{1}{\alpha}} \quad \text{Equation 2}$$

For glass forming polymers, τ_{\max} vs. $1/T$ plots for the α process exhibit curvature rather than being linear and the data is commonly represented using the Vögel-Fülcher-Tammann (VFT) equation:²⁰

$$\tau(T) = \tau_0 \exp\left(\frac{E_a}{k_B(T - T_V)}\right) \quad \text{Equation 3}$$

τ_0 , E_a , and T_V are obtained by fitting equation 3 to experimental data. k_B is the Boltzmann constant. τ_0 is a hypothetical relaxation time at infinite temperature. E_a is not an activation energy but related to the polymer fragility.²¹ T_V , the Vögel temperature, is that at which chain segments become frozen in a hypothetical situation when the polymer is cooled at a quasi-static rate from the liquid (rubbery state) and is considerably less than T_g .²²

In the literature, dielectric relaxation studies of sulfonated PS polymers²³ and sSEBS incorporating different ions have been reported.^{24,25} The presence of ions caused profound changes in dielectric constant (storage permittivity ϵ') and also two different activation energies observed corresponding to multiplets and clusters of ionic aggregates. Here, the relaxations of sSEBS filled with iron oxide nanoparticles that were synthesized via an *in-situ* bottom-up process are reported.

Experimental

Materials

The SEBS copolymer, Kraton[®] G1652, obtained from Kraton[®] LLC, had ~30 mol % styrene and total $M_n = 73,600$ g/mol. All reagents used for sulfonation were used without further purification. Dichloroethane (DCE) (99.8%), toluene, 1-hexanol (98%), acetic anhydride (ACS grade) and sulfuric acid (ACS grade) were obtained from Fisher Co.

Sulfonation Procedure

Sulfonation of styrene blocks in SEBS was performed up to ~20 mole % according to a previously reported procedure.^{26,27} In brief, the BCP was dissolved in DCE at ~54° C. The sulfonating agent, acetyl sulfate, was prepared by mixing DCE and acetic anhydride and cooled to -10° C after which sulfuric acid was added. Once acetyl sulfate was prepared, it was used in less than 10 min. In order to obtain the desired final sulfonation level, a required amount of acetyl sulfate was added to the BCP/DCE mixture. The color of the final reaction mixture changed from normal to light brown and then to dark brown from lower to higher levels of sulfonation. The reaction proceeded for 2h and the final polymer was recovered by boiling it several times, filtration, and finally drying under vacuum at 60° C for 7d to remove any residual water. The sulfonation level was determined by dissolving 0.1 mg of sample in a toluene/hexanol mixture at 80° C against standardized base to a phenolphthalein end point. Percent sulfonation values obtained from standard titration were 2-3 % and consistent with values obtained from elemental analysis. The names of sulfonated SEBS samples were shortened as in the

following examples: 0SEBS means 0 mole % sulfonation and 16SEBS means 16 mole % sulfonation, etc.

Film Casting Procedure

A 10% solution was prepared by dissolving an unmodified BCP in toluene which was then cast in a Teflon[®] petri dish and allowed to dry at ~45° C for 7d. Then it was annealed under vacuum (~30 in Hg) at 120° C for 2d. Films of sulfonated SEBS were cast in the same manner but were dissolved in a mixture of toluene and hexanol as a co-solvent. All the films were cast to have less 0.5 mm thickness. The same samples were used for both BDS and AFM measurements.

Metal Oxide Incorporation

Pre-formed films having these sulfonation levels were swollen in DMAc for 48h and constantly shaken. A 3.0 M solution of FeCl₃ in DMAc was prepared and the swollen films were submerged in them separately for 48h in a shaker. The samples were removed and surface wiped with tissue paper to minimize precipitation. These metal chloride-doped samples were then washed with DI water several times to leach out excess electrolyte. In the final step, each of the three samples was placed in a fresh 2 M NaOH solution for 48h and washed with DI water continuously for 48h. The water was monitored regularly and the basic water replaced with fresh water to leach out excess Na⁺ ions. After washing, samples were dried in an oven for 48h at 120° C to remove excess solvents and water.

Samples for AFM and BDS Investigations

All films were cut into small triangular shapes with a base at least 10 mm wide and pasted vertically on 12 mm diameter AFM discs with an epoxy steel resin, and dried

for a few hours until the epoxy hardened. Prior to pasting, the surfaces of AFM discs were polished with sandpaper to facilitate proper contact between epoxy and the metal surface. The top tip of a triangular shaped sample was trimmed with a razor blade to avoid wiggling when the sample approached a diamond knife. The surface polishing was performed at -75°C as T_g of the EB block is around -40°C . In order to avoid loss of surface features on the polished samples, the temperature below T_g of the EB block was chosen so that both PS and EB chains are frozen. Each sample was placed in a Leica ultra cryo-microtome chamber (UC FC6) at -75°C .

The storage of samples and their loading in the instrument were followed according to that of Rhoades *et al.*²⁸ Films for BDS measurements were previously cut into 20 mm diameter samples and preconditioned in a previously calibrated controlled 0% relative humidity chamber for at least 5d. Film thickness was measured inside the chamber without exposing the sample to the outside atmosphere before placing it between the gold electrodes. This unit was then transferred this to the BDS instrument. The entire step was completed within 2 min to minimize the exposure of the sample to atmospheric humidity.

Material Characterization

Fourier Transform Infrared Spectroscopy (FTIR)

FTIR spectroscopy was used to verify sulfonation of the styrene rings in the outer blocks. Absorption spectra for unsulfonated (0SEBS) and 16SEBS and 20SEBS samples were obtained using a Bruker Equinox 55 FT-IR optical bench. Attenuated total reflectance mode was used for the same films which were used for the AFM and BDS studies described later. Spectra were produced using a SensIR 3-Reflection horizontal

ATR module. The crystals were composed of ZnSe/Diamond composite materials. All spectra were collected after 32 scans with 4 cm^{-1} resolution. A background spectrum of the crystal was subtracted from each spectrum. At least 4 spectra were obtained at different locations of the same sample and averaged.

AFM

Tapping mode - phase images for the 16SEBS/iron oxide and 20SEBS/iron oxide materials were obtained on polished mirror surfaces generated by cryo-microtoming. Scans were performed at ambient conditions using a Dimension 3000 AFM with NanoScope[®] III controller from Veeco Co. (Digital Instruments). The nominal spring constant and resonance frequency ranges were 20-80 N/m and 239-286 kHz, respectively. The tip radius curvature reported by the manufacturer was less than 10 nm. High resonance frequency tips were used to ensure maximized phase contrast between hard and soft blocks. Once the sample cross sections were polished and microtomed, tapping mode AFM (TMAFM) scans were performed within 5 min to ensure the surface was not contaminated with dust particles.

Dielectric Spectroscopy Measurements

Dielectric relaxation spectra for all the samples were collected using a Novocontrol GmbH Concept 40 broadband dielectric spectrometer over the frequency (f) range 0.01 Hz to 3 MHz and over the temperature range $-120\text{ }^{\circ}\text{C}$ to $200\text{ }^{\circ}\text{C}$. The temperature stability of instrument was controlled to within $\pm 0.2\text{ }^{\circ}\text{C}$. Samples were cut into 20 mm diameter discs and placed between two 20 mm diameter gold coated copper electrodes. Before placing the sample between the electrodes they were sandwiched between two thin aluminum foils (smaller diameter (19 mm)) to achieve good contact

with the electrodes and for easy removal. The diameter of aluminum foil was a bit smaller to avoid short circuiting the bridge. Two samples were tested for each type of material to verify the data reproducibility. Verification tests were also conducted to ensure that the aluminum foil did not alter the dielectric spectra of the polymer material.

Curve fitting for the loss permittivity (ϵ'') vs. frequency (f) data was performed using Novocontrol WinFit software. The parameters σ_0 , N , τ_{HN} , $\Delta\epsilon$, α , and β seen in Equation 1 were obtained by best-fitting using the HN equation at each temperature for each sample.

Results and Discussion

FTIR spectra of unsulfonated and sulfonated SEBS are shown in Figure VI-1. The bands for 0SEBS, 16SEBS and 20SEBS samples are listed in Table VI-1. The region of interest for the sulfonated samples is 600 to 1400 cm^{-1} . Peaks at 1370 and 905 cm^{-1} correspond to asymmetric sulfur-oxygen stretching vibrations having double-bond character ($\text{O}=\text{S}=\text{O}$) and stretching vibration of the SO having single-bond character. The bands at 1127 and 1007 cm^{-1} correspond to in-plane skeletal vibrations of benzene (aromatic) rings substituted by $-\text{SO}_3^-$ groups at the para (p -) position and in-plane bending of CH_2 on p -substituted aromatic rings respectively. The band at 612 cm^{-1} in both sulfonated samples corresponds to C-S stretching vibration in the $-\text{SO}_3\text{H}$ substituted benzene ring²⁹⁻³¹ which is direct evidence of sulfonation.

Table VI-1. IR absorption band assignments for unsulfonated and sulfonated SEBS samples

Unsulfonated SEBS (0SEBS)		Sulfonated SEBS (16SEBS and 20SEBS)	
Peak position (cm ⁻¹)	Assignment	Peak position (cm ⁻¹)	Assignment
696	Out of plane bending (aromatic C-C)	612	C-S stretching vibration
757	Out of plane bending (aromatic CH)	905	S-O stretching
1379	CH ₃ symmetric bending	1007	In-plane bending of CH ₂ on p-substituted aromatic rings
1455	CH ₂ scissor	1127	In-plane skeletal vibrations of p-substituted benzene ring with SO ₃ ⁻
1492	Aromatic ring stretching	1370	O=S=O anti-symmetric stretching vibrations
2851	CH ₂ symmetric stretching		
2920	CH ₂ asymmetric stretching		
2960	CH ₃ asymmetric stretching		

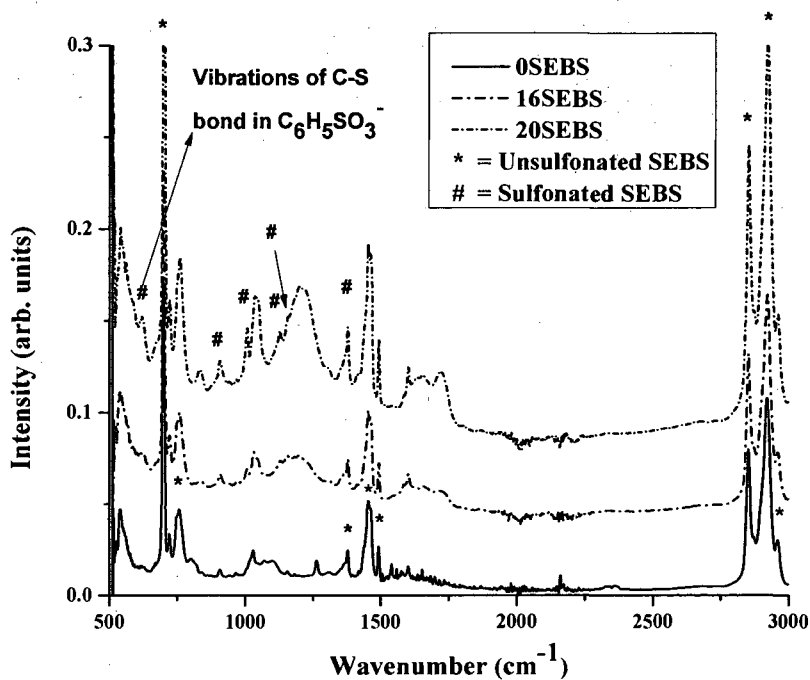
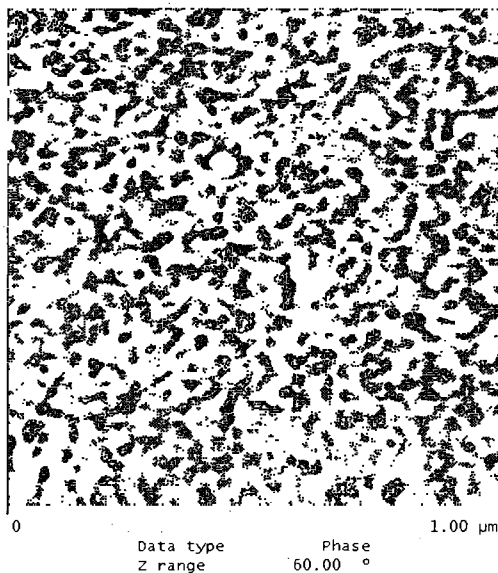


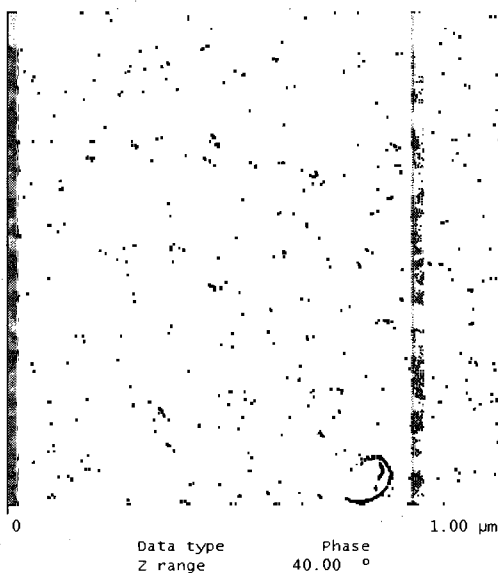
Figure VI-1. FTIR/ATR absorbance spectra of sulfonated and unsulfonated SEBS.

Tapping mode AFM images for 16 and 20SEBS/iron oxide samples are shown in Figures VI-2 a and b. The bright and dark parts of the images are hard (sPS) and soft (EB) block phases, respectively. Particles ~ 75 nm in size are observed against the bright features, which suggests the selective growth of nanoparticles in the sPS block domains which is also in harmony with dynamic mechanical analysis of the same nanocomposites from earlier studies.³²

VI-2(a)



VI-2(b)



Figures VI-2 (a-b). TMAFM phase images of 16SEBS/iron oxide and 20SEBS/iron oxide showing nanoparticles size of ~ 75 nm, respectively.

A 3-D ϵ'' vs. f and T plot is seen in Figure VI-3 for 0SEBS. There are three ridges on the surface that correspond to the EB and PS block domains in their respective relaxation temperature and frequency windows. These ridges represent the loci of all maxima on ϵ'' vs. f curves at each T . The first ridge which starts at -120°C , and is labeled

β_{EB} , extends to -70°C and is due to local conformational fluctuations in EB block segments.^{15,16,33} The second ridge starting from -40°C to 20°C corresponds to segmental relaxations, labeled α_{EB} , in the EB block domains. The third ridge, which starts from 100°C and extends to 150°C , corresponds to segmental relaxations, labeled α_{PS} , in the PS block domains. The α transitions are related to glass transitions whereas the β transition involves relaxations of styrene rings or Johari-Goldstein β relaxations.

Having fitted ϵ'' vs. f data with WinFit software, transitions are observed between 20 and 100°C corresponding to the β_{PS} relaxation or perhaps chain sections in EB and PS interphase regions. The α transition temperatures in both EB and PS blocks for the same 0SEBS sample matched with the glass transition temperature ranges as seen in dynamic mechanical $\tan \delta$ vs. temperature scans at a rate of $2^{\circ}\text{C}/\text{min}$ and frequency of 1 Hz.^{34,35}

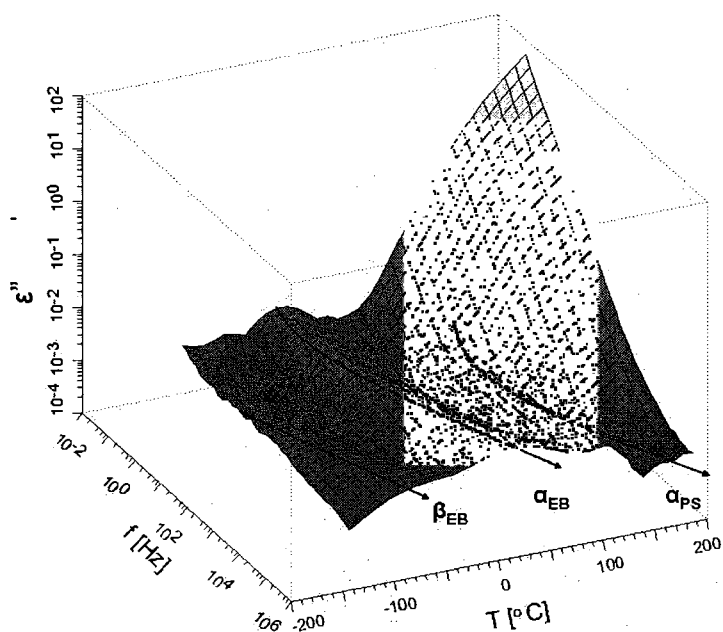
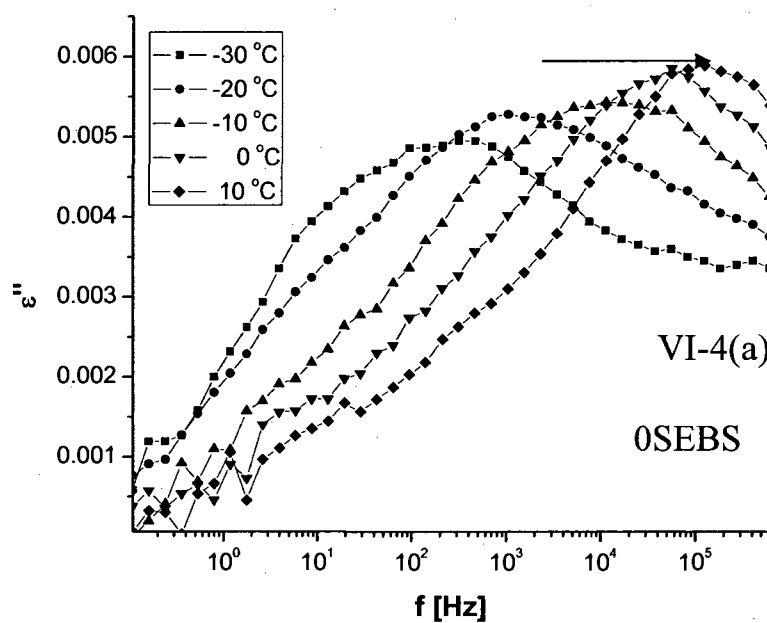
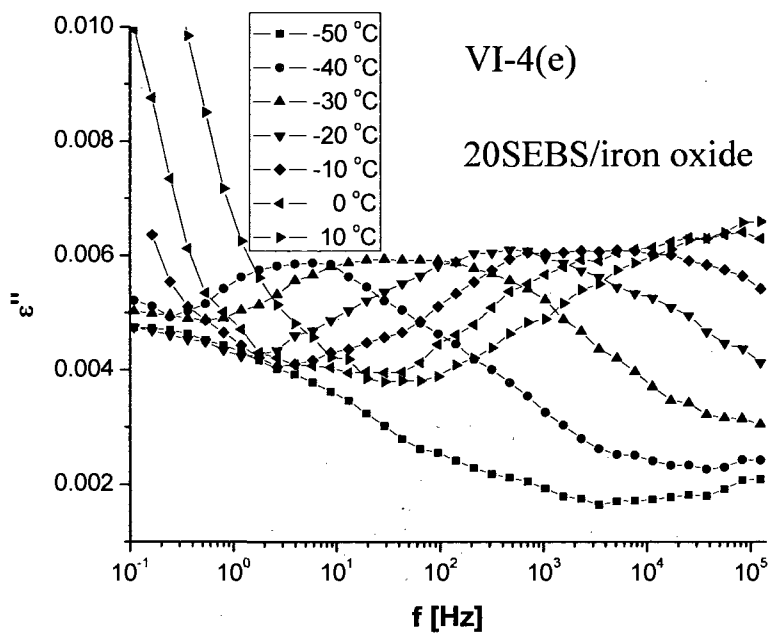
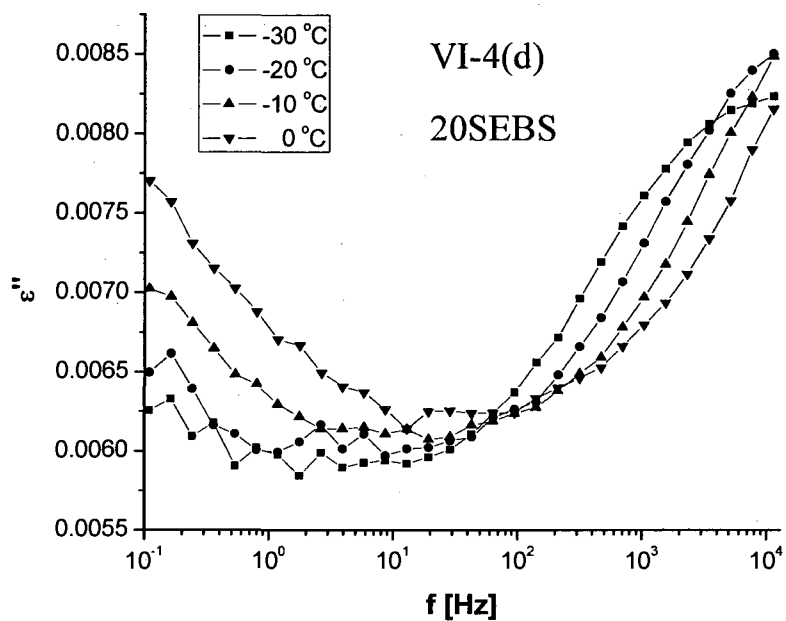


Figure VI-3. 3D surface showing ϵ'' versus $\log_{10}f$ versus temperature for 0SEBS sample.

The HN equation was fitted to permittivity data for each sample over the entire temperature range. Figures VI-4a-e and VI-5a-e show data fits for the α relaxations in the EB and PS block domains, respectively.



Figures VI-4 (a-e). ϵ'' versus $\log_{10}f$ plots for 0SEBS, 16SEBS, 16SEBS/iron oxide, 20SEBS, 20SEBS/iron oxide, respectively in EB block region. (The contribution of DC conductivity is subtracted from ϵ'' data in above all five figures).



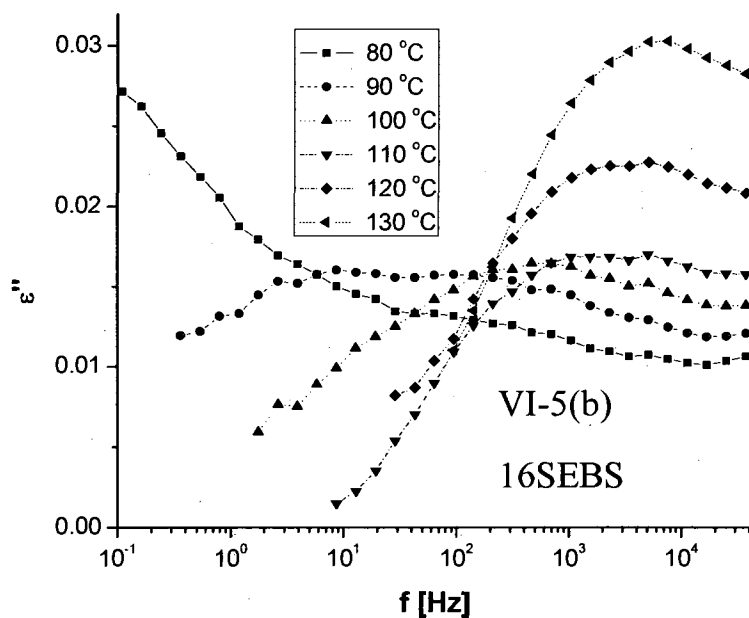
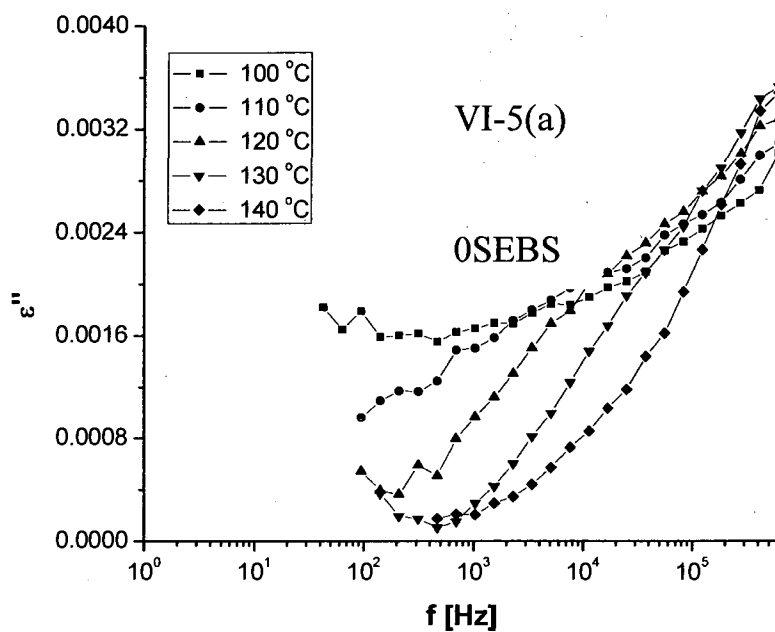
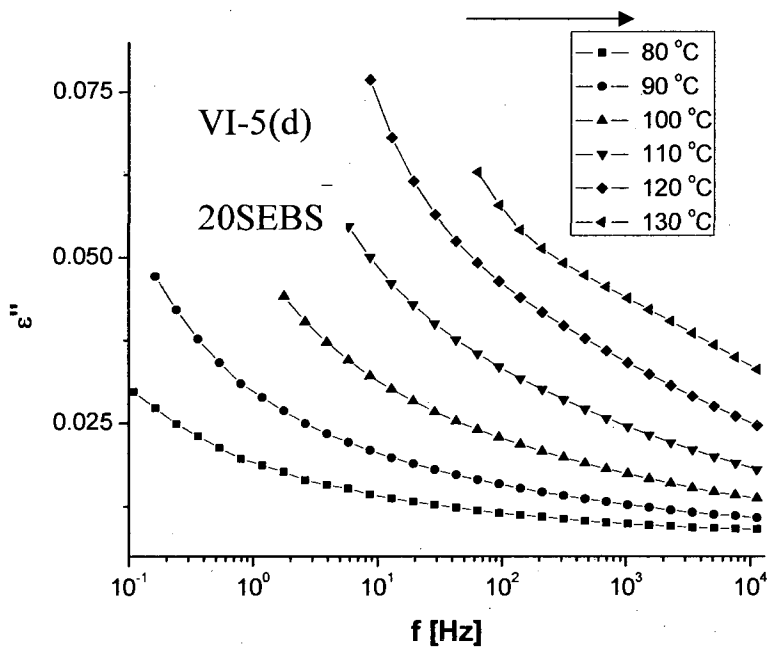
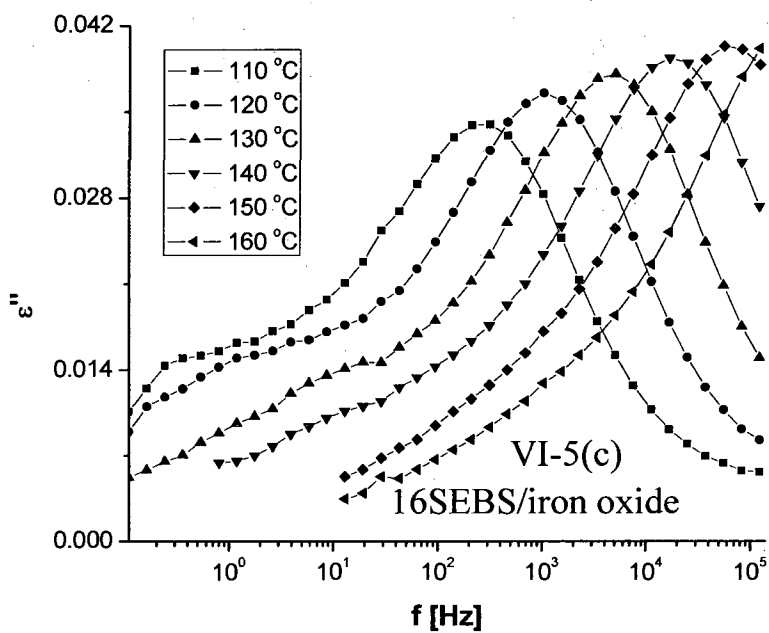
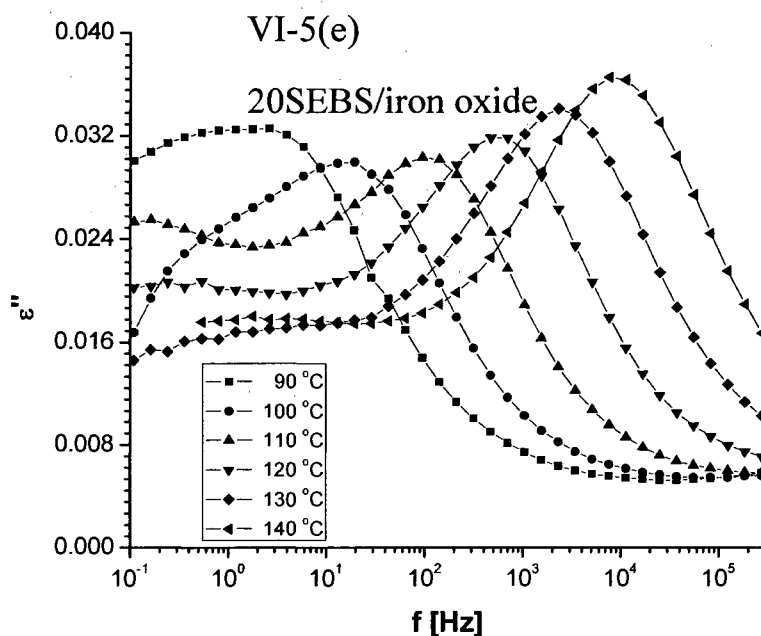


Figure VI-5 (a-e). ϵ'' vs. $\log_{10} f$ for 0SEBS, 16SEBS, 16SEBS/iron oxide, 20SEBS, 20SEBS/iron oxide, respectively, for PS block domain relaxation. (The contribution of DC conductivity is subtracted from ϵ'' data in above all five figures).

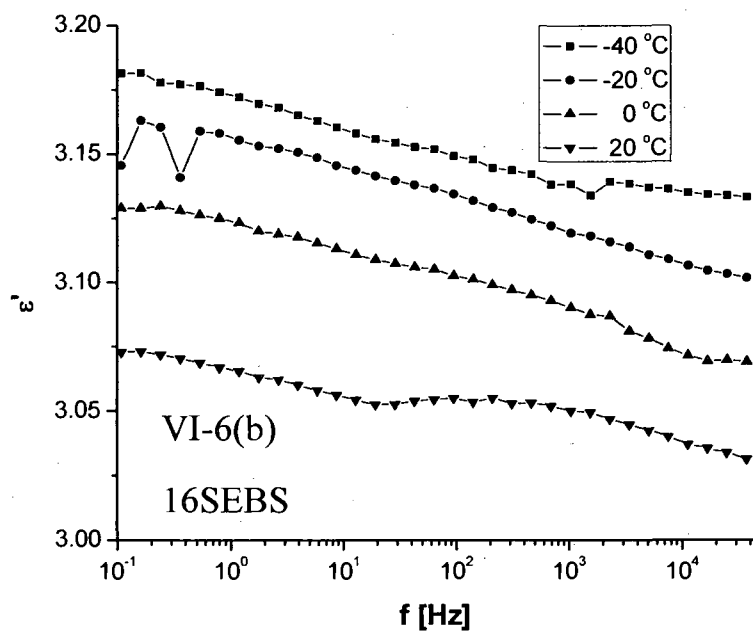
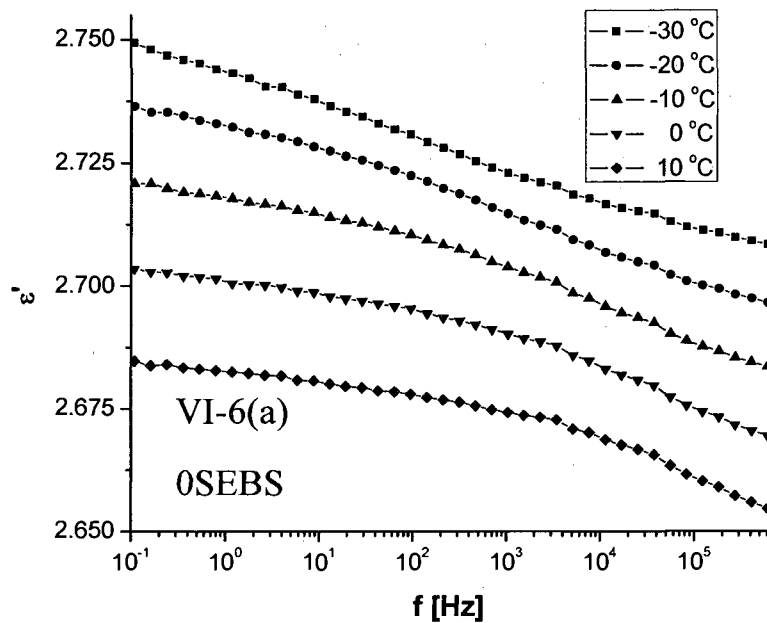




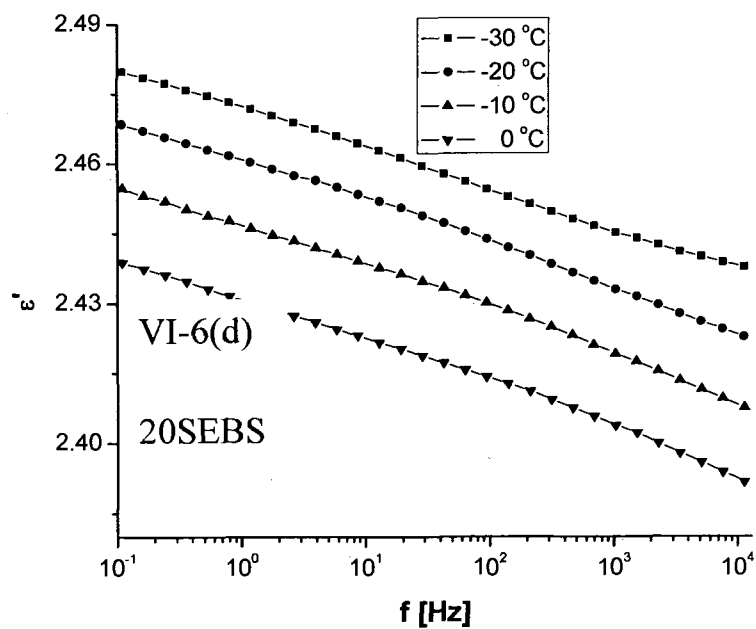
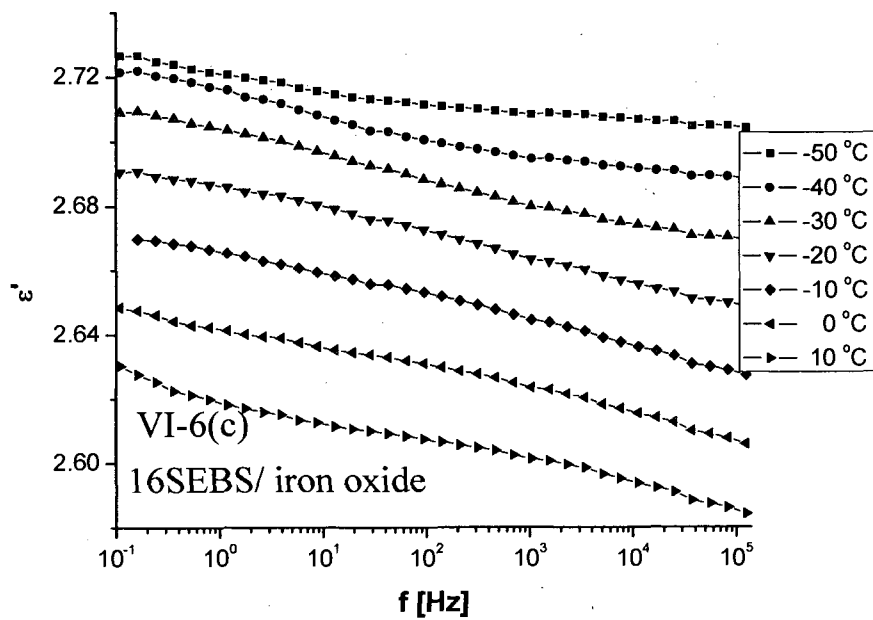
Each data curve had the obscuring low frequency d.c. conductivity contribution subtracted and it is seen that conductivity increases with sulfonate content, as is reasonable. Figures VI-5b and 5d contain ϵ'' vs. f curves for 16 and 20SEBS. The effect of d.c. conductivity in 20SEBS is more prevalent and overwhelms the α and/or β peaks. The signature of this phenomenon is the nearly straight lines seen in Figure VI-5d. The inorganic component in the sPS blocks caused ϵ'' vs. f curves for the relaxation in these regions to be narrower with increase in temperature. Some $-\text{SO}_3\text{H}$ groups may become embedded in iron oxide nanoparticles during their formation.

The frequency at peak maximum (f_{max}) for each curve at a given temperature determines a relaxation time $\tau_{\text{max}} = (2\pi f_{\text{max}})^{-1}$. In Figures VI-4 a-e and VI-5 a-e f_{max} is seen to increase with increase in temperature in the usual fashion. It was also observed that after incorporation of nanoparticles in the sPS phase the glass transition range

broadens by decades in both the EB and PS (sPS) block domains. This may be due to inhomogeneous distribution of $-\text{SO}_3\text{H}$ groups after the sulfonation reaction in the PS blocks or perhaps some $-\text{SO}_3\text{H}$ groups are relatively free while some are entrapped around the inorganic nanoparticles. Also, the $-\text{SO}_3\text{H}$ groups were exchanged with Fe^{+3} ions which were converting to iron oxide nanoparticles. The presence of an uneven number of $-\text{SO}_3\text{H}$ pendant groups on each PS chain may lead to unequal length physical cross-links that were formed in association with iron oxide nanoparticles, causing a wider distribution of polymer chains resulting in broadening the α_{PS} transition. For the EB region the formation of physical cross links within PS blocks indirectly hinders the motions of EB chains and widens the α_{EB} transition region. The storage permittivity (ϵ') vs. frequency data plots for all the samples in EB and PS block phases are shown in Figures VI-6 a-e and VI-7 a-e respectively.



Figures VI-6 (a-e). ϵ' versus $\log_{10} f$ plots for 0SEBS, 16SEBS, 16SEBS/iron oxide, 20SEBS, 20SEBS/iron oxide, respectively in EB block region. (The contribution of DC conductivity is subtracted from ϵ'' data in above all five figures).



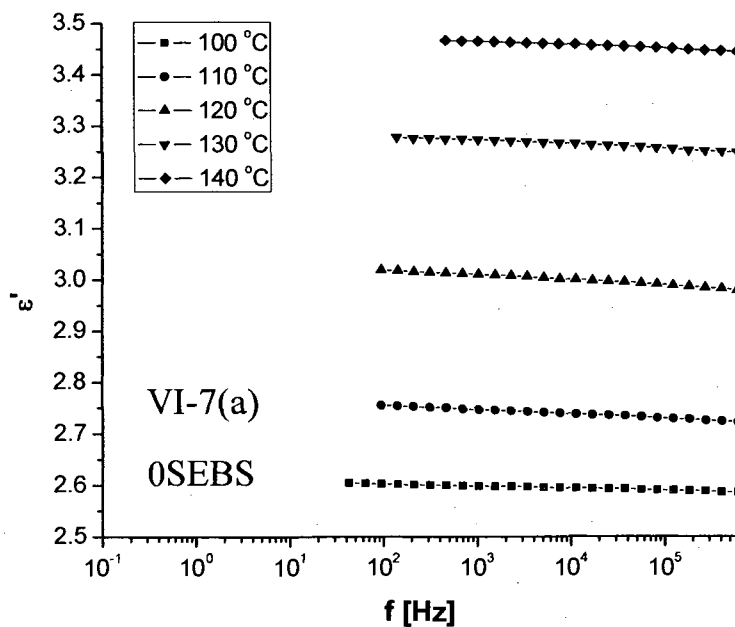
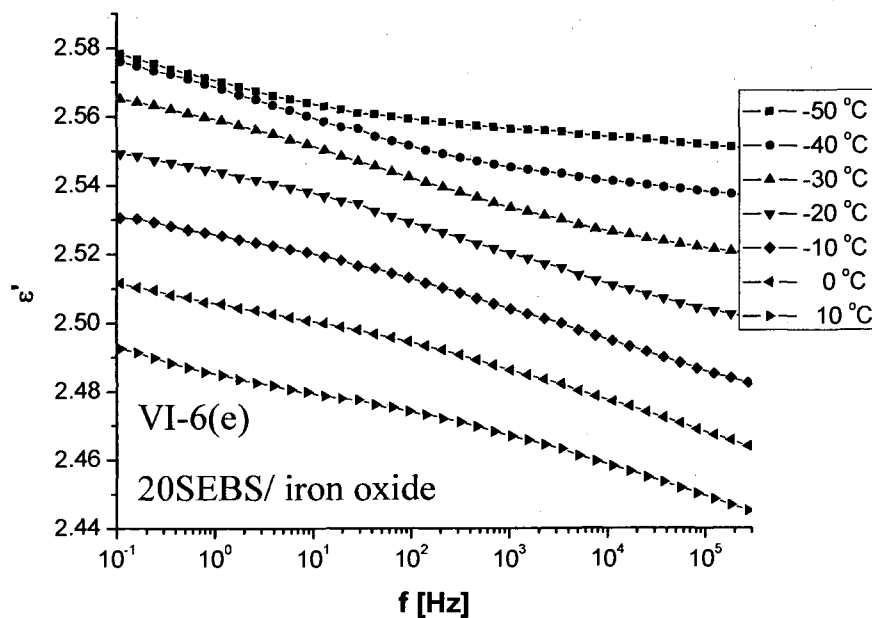
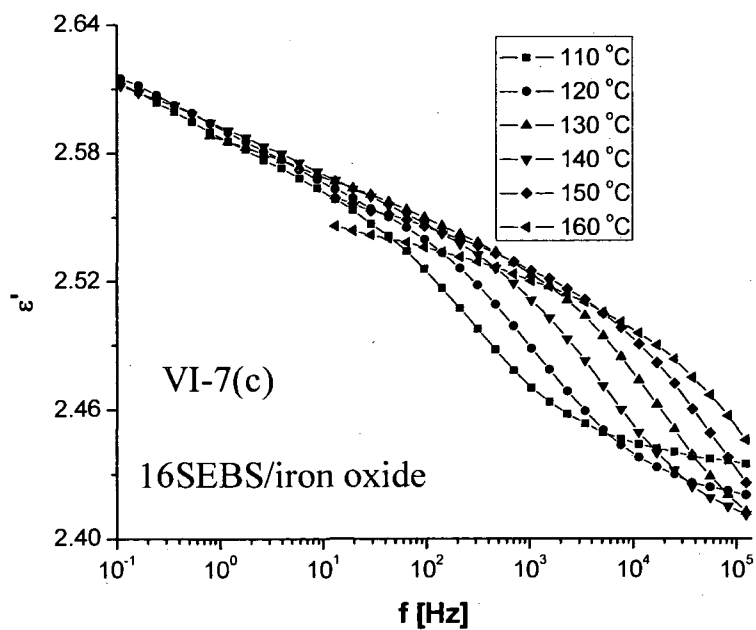
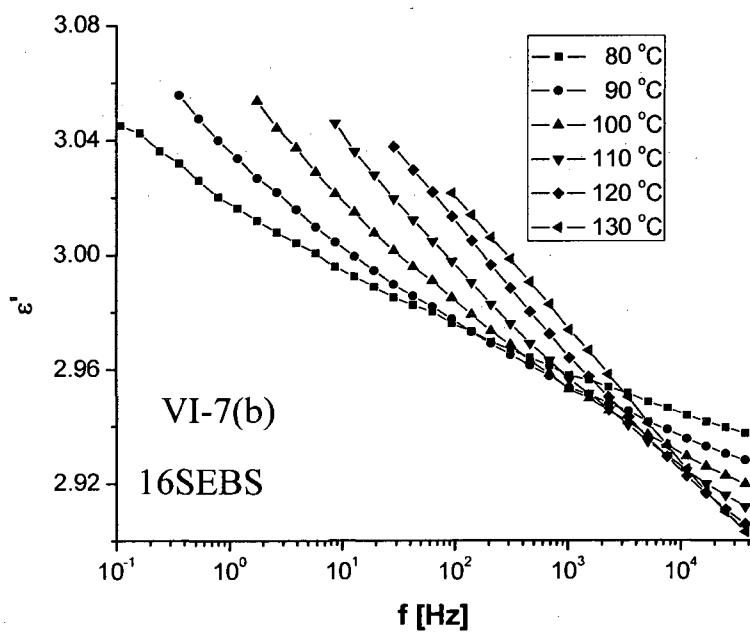
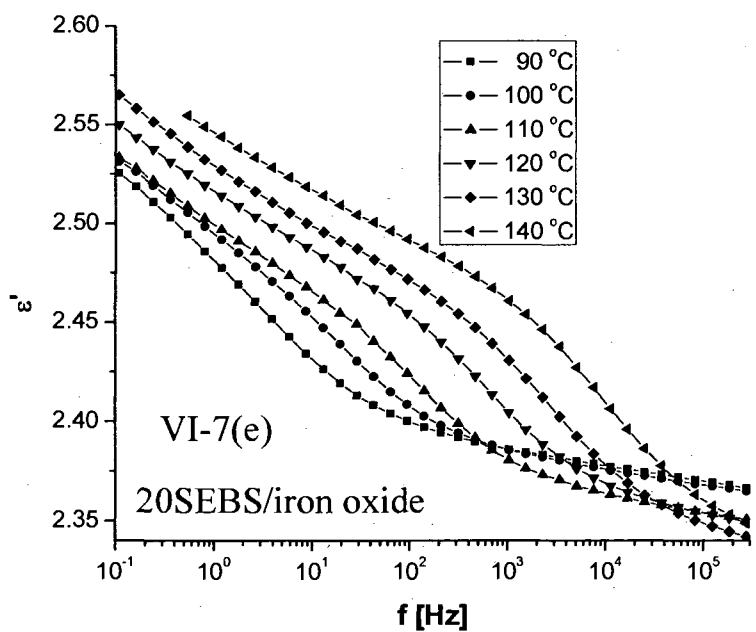
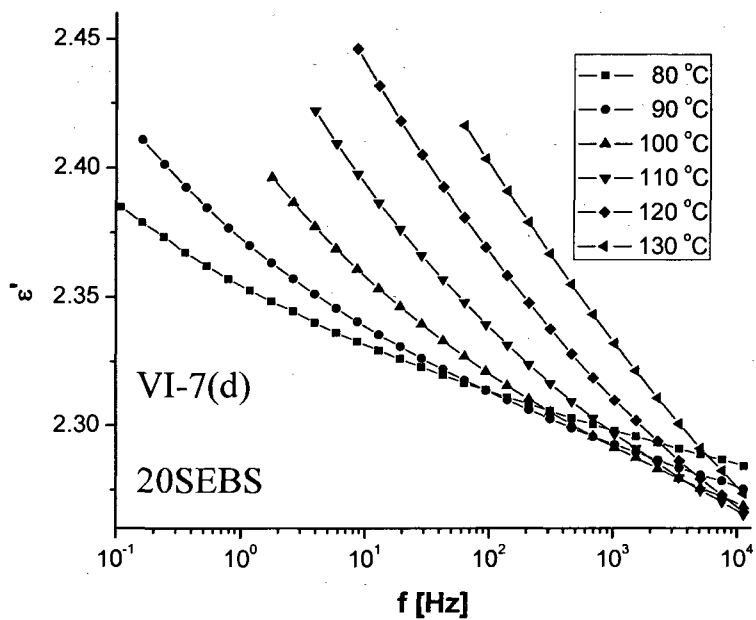


Figure VI-7 (a-e). ϵ' vs. $\log_{10} f$ for 0SEBS, 16SEBS, 16SEBS/iron oxide, 20SEBS, 20SEBS/iron oxide, respectively, for PS block domain relaxation. (The contribution of DC conductivity is subtracted from ϵ'' data in above all five figures).





From Figures VI-6 a-e and VI-7 a-e, the storage permittivity ϵ' values were decreasing with increase in temperature in EB phase where as PS phase they were increasing with increase in temperature.

Figures VI-8 and VI-9 show $\log \tau_{\max}$ vs. $1/T$ data plots to which were fitted the VFT equation for the α relaxation in the EB and PS block phases, respectively. In Figure VI-8 all the curves are nonlinear, i.e., non-Arrhenius. The relaxation times become longer with increase in sulfonation indicating a loss in chain mobility due to increased hydrogen bonding interactions. With incorporation of iron oxide nanoparticles, the relaxation time increases at the same temperature. The shift in τ_{\max} was over an order of magnitude between 16SEBS and 16SEBS/iron oxide and also between 20SEBS and 20SEBS/iron oxide at higher temperatures indicating chain constraints introduced by the inorganic structures. Figure VI-9 shows the VFT curves of all the samples in α transition region for the PS block phase. The presence of iron oxide nanoparticles in sPS phase broadened and shifted the α transition of the PS/sPS block phase to higher temperatures by a few decades. $\log \tau_{\max}$ vs. $1/T$ curves for both 16 and 20SEBS in the PS glass transition regions was nonlinear and fit VFT behavior, whereas, with incorporation of iron oxide nanoparticles in the sPS phase, these curves tend towards linearity with an infinite curvature (Arrhenius type behavior). The reason for this linear behavior is offered as follows.

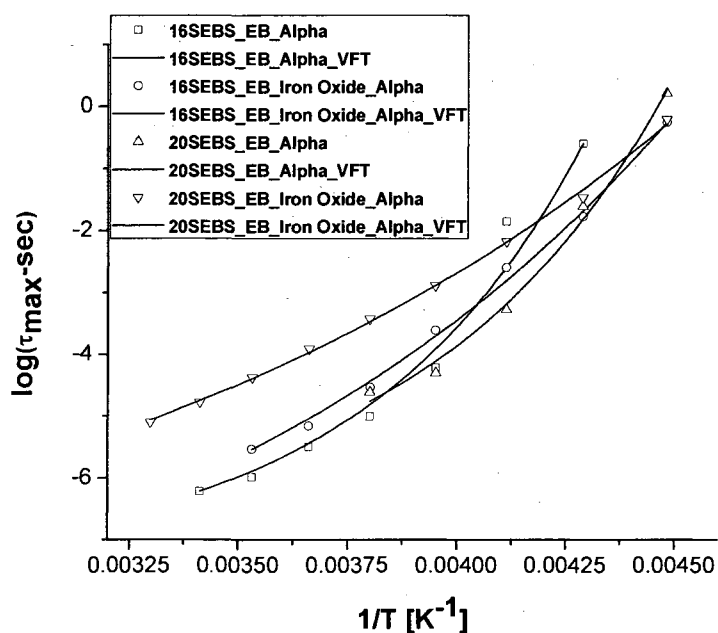


Figure VI-8. VFT equation fittings to data for unsulfonated and sulfonated SEBS and sulfonated SEBS filled with iron oxide nanoparticles in the EB glass transition region.

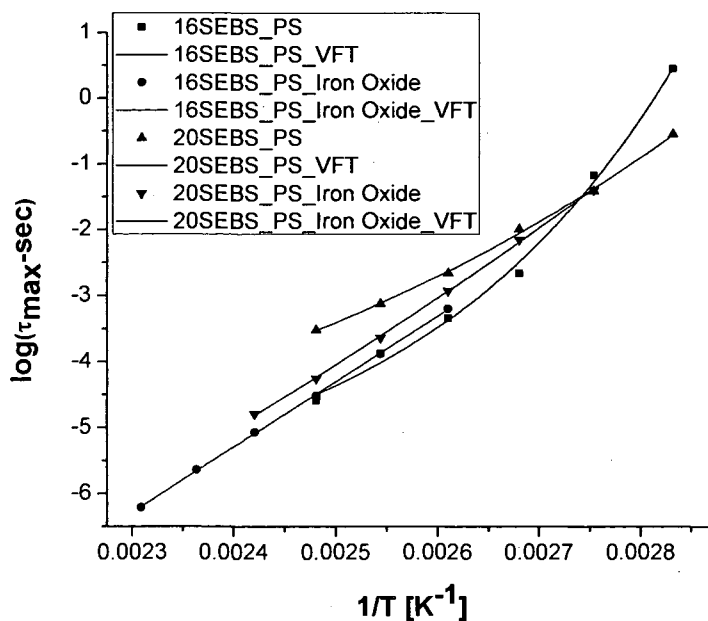


Figure VI-9. VFT equation fits to data in the PS block domain glass transition region for unsulfonated, sulfonated and sulfonated SEBS filled with iron oxide.

In glass forming polymers, both the α and β relaxations merge at one particular temperature and after that exhibit one single α -like transition. The characteristic of this α transition might be influenced by the presence of β relaxation after the merging region.³⁶ In the case of these sSEBS BCPs exchanged with iron oxide nanoparticles via a bottom-up process, as in the case here, the relaxation occurring earlier to the α relaxation (primary relaxation) may be partially or fully due to side chains (β type) or may be due to polymer chains in the interphases between the EB and PS block domains.

After incorporation of iron oxide nanoparticles, a wide distribution of chains that are attached to these iron oxide nanoparticle results. Thermal kinetic energy that is supplied to these sPS chains with iron oxide nanoparticles with different lengths will be activated at different frequencies (relaxation time scales) resulting in a broad distribution. When the temperature reaches a value to where both β and α processes merge and the influence of side chain relaxations in the interphases filled with nanoparticles overwhelms the α process to a limit, linearity in $\log \tau_{\max}$ vs. $1/T$ curves occurs. This α process can be denoted as α' because of its linearity on VFT curves while existing in the regular glass transition region. The merging of β and α process in the cases of 16 and 20SEBS/iron oxide samples is shown in Figures VI-10 a and b respectively.

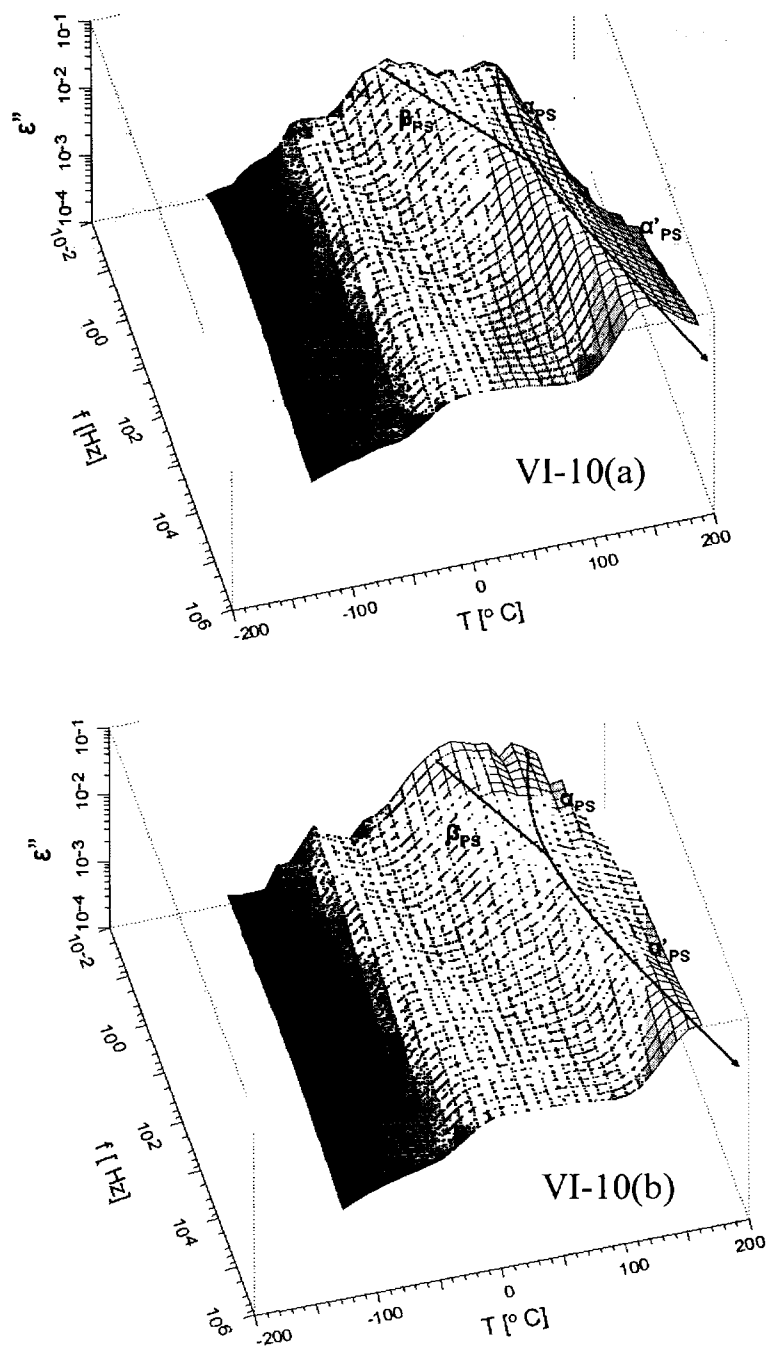


Figure VI-10 a-b: Merging of β and α transitions near the PS block glass transition region for 16 and 20SEBS/iron oxide.

The VFT curve fit parameters for all the samples in both the β and α relaxation regimes are listed in Table VI-2.

Table VI-2: VFTH parameters for α transitions in both EB and PS regions for all the samples

Sample	α_{EB}		α_{PS}	
	τ_{max} (s)	T_V (K)	τ_{max} (s)	T_V (K)
0SEBS	4.1×10^{-13}	182.9	6.5×10^{-10}	354.7
16SEBS	3.9×10^{-08}	228.5	1.0×10^{-09}	308.6
16SEBS/iron oxide	9.8×10^{-14}	140.2	6.0×10^{-13}	279.1
20SEBS	4.6×10^{-10}	187.1	1.0×10^{-11}	228.7
20SEBS/iron oxide	1.5×10^{-10}	143.5	4.1×10^{-11}	279.1

As predicted by previous workers and earlier literature an increase in acid content and presence of inorganic structures should increase τ_{max} due to obstructions to chain movements. In the case of the work here the trend does not follow that described earlier. τ_{max} increases with increase in sulfonation in the EB region whereas in the PS region the trend was random. τ_{max} values for the samples filled with iron oxide nanoparticles do not follow any trend in both EB and PS regions. Perhaps this lack of trend is due to incorporation of iron oxide nanoparticles in the $-SO_3H$ clusters in the interfacial regions.

Conclusions

Sulfonated SEBS films were ion exchanged with iron chloride solution in a suitable solvent to enable the growth of iron oxide nanoparticles in selective domains (sPS block domains) via an in-situ bottom up process. FT-IR spectra of the unsulfonated and sulfonated samples were compared to observe the changes due to the sulfonation level at specific functional groups and sulfonation of PS blocks was confirmed. Tapping mode AFM (TMAFM) was performed on the freshly polished surfaces of both 16SEBS/iron oxide and 20SEBS/iron oxide film cross-section, revealed that the growth of the nanoparticles was taken place in sPS domains leaving the EB domain unaffected. Dielectric relaxation spectroscopic analysis of unsulfonated, and sulfonated SEBS films

indicated, chains will relax faster with increase in temperature and $f_{\max} [= (2\pi\tau_{\max})^{-1}]$ value shifts to higher frequencies (τ_{\max} gets smaller). But with the incorporation of iron oxide nanoparticles in sPS phase, the relaxation spectrum of ϵ'' vs. f different temperatures in the neighborhood of glass transition regions of both EB and PS phases became broader. This is due to anchoring of iron oxide nanoparticles to different $-\text{SO}_3\text{H}$ groups and possible cross-linking network which might give rise to an apparent chain length with different relaxation times. The VFTH fittings all the samples in α_{EB} region for all samples, the relaxation time vs. $1/T$ (K^{-1}) plots exhibited a non-Arrhenius type behavior. The relaxation time for the iron oxide exchanged samples of 16SEBS and 20SEBS in α_{EB} region was increased by at least an order of magnitude. The VFTH fittings of iron oxide exchanged samples of 16SEBS and 20SEBS in α_{PS} exhibited a linear behavior whereas the unloaded samples exhibited non-Arrhenius type behavior. The departure from non-Arrhenius behavior in α_{PS} region in iron oxide loaded samples in 16SEBS and 20SEBS might be due to merging of β_{PS} process with the α_{PS} process leading to an apparent α'_{PS} process after the merging point with a huge influence of side chain relaxations (β process) in the interfacial regions.

Acknowledgements

We acknowledge the National Science Foundation (NSF) Material Research Science and Engineering Center (MRSEC) Division of Materials Research (DMR-0213883) for Stimuli Responsive Materials at the University of Southern Mississippi for funding. We also thank Kraton® LLC for donating SEBS block copolymers.

References

- (1) Holden, G.; Legge, N. R.; Quirk, R. P.; Schroeder, H. E. editors. *Thermoplastic Elastomers*, 2nd ed. 1996.
- (2) Mauritz, K. A.; Storey, R. F.; Mountz, D. A.; Reuschle, D. A. *Polymer* **2002**, 43, 4315.
- (3) Mauritz, K. A.; Storey, R. F.; Reuschle, D. A.; Tan, N. B. *Polymer* **2002**, 43, 5949.
- (4) Mauritz, K. A.; Blackwell, R. I.; Beyer, F. L. *Polymer* **2004**, 45, 3001.
- (5) Kremer, F.; Schonhals, A. *Broadband Dielectric Spectroscopy*: Springer; New York, 2003.
- (6) Singh, P.; Babbar, V. K.; Razdan, A.; Puri, R. K.; Goel, T. C *Journal of Applied Physics* **2000**, 87, 4362.
- (7) Chen, Y. J.; Cao, M. S.; Wang, T. H.; Wan, Q. *Applied Physics Letters* **2004**, 84, 3367.
- (8) Lim, K. M.; Lee, K. A.; Kim, M. C.; Park, C. G. *Journal of Non-Crystalline Solids* **2005**, 351, 75.
- (9) Ahmed, S. R.; Kofinas, P. *Macromolecules* **2002**, 35, 3338.
- (10) Rajan, G. S.; Mauritz, K. A.; Stromeyer, S. L.; Kwee, T.; Mani, P.; Weston, J. L.; Nikles, D. E.; Shamsuzzoha, M. *Journal of Polymer Science, Part B: Polymer Physics* **2005**, 43, 1475.
- (11) Anderson, P. W. *Science* **1995**, 2681154.
- (12) McCrum, N. G.; Read, B. E.; Williams, G. *Anelastic and Dielectric Effects in Polymeric Solids*; London; Wiley: 1967 (reprint: Dover: New York, 1991).

- (13) Alegri'a, A. J. *Basic Features of the Glassy State*; Colmenero, Eds.; World Scientific: Singapore, 1990.
- (14) Go'tze, W. *In Liquids, Freezing and the Glass Transition*; Hansen, J. P.; Levesque, D.; Zinn-Justin, J. Eds.; North- Holland: Amsterdam, 1991.
- (15) Johari, G. P.; Goldstein, M. *Journal of Chemical Physics* **1970**,53, 2372.
- (16) Johari, G. P.; Goldstein, M. *Journal of Chemical Physics* **1971**,55, 4245.
- (17) Johari, G. P. *Relaxations in Complex Systems* edited by Ngai, K. L.; Wright, G. B. ~Naval Research Laboratory, U.S. Government Printing House, Springfield, VA, 1984, p. 17.
- (18) Havriliak, S.; Negami, S. *Journal of Polymer Science, Polymer Symposia* **1966**,14,99.
- (19) Havriliak, S.; Negami, S. *Polymer* **1967**, 8,161.
- (20) Negami, S.; Ruch, R. J.; Myers, R. R. *Journal of Colloid Interface Science* **1982**,90,117.
- (21) Vogel, H.; *Physics Z* **1921**, 22, 645; Tammann,G.; Hesse,W.; *Anorg Allgem Chem* **1926**,56,245; G.S. Fulcher, G. S. *Journal of American Ceramic Society* **1923**,8,339.
- (22) Angell, C. A. *Journal of Non-Crystalline Solids* **1991**,131,13.
- (23) Schönhals, A. in: Runt, J. P.; Fitzgerald, J. J. (Eds.), *Dielectric Spectroscopy of Polymeric Materials: Fundamentals and Applications*; ACS Publications: Washington DC, 1997, p 89.
- (24) Atorngitjawat, P.; Klein, R. J.; Runt, J. *Macromolecules* **2006**,39,1815.
- (25) Ghosh, S. K.; De, P. P.; Khastgir, D.; De, S. K. *Macromolecule Rapid Communications* **1999**,20,505.

- (26) Ghosh, S. K.; De, P. P.; Khastgir, D.; De, S. K. *Journal of Applied Polymer Science* **2000**,77,816.
- (27) Blackwell, R. I.; Mauritz, K. A. *Polymer* **2004**, 45, 3457.
- (28) Weiss, R. A.; Sen, A.; Willis, C. L.; Pottick, L. A. *Polymer* **1991**, 32, 1867.
- (29) Rhoades, D. W.; Hassan, M. K.; Osborn, S. J.; Moore, R. B.; Mauritz, K. A. *Journal of Power Sources* **2007**,172,72.
- (30) Zundel, G. *Hydration and intermolecular Interaction: Infrared Investigations with Polyelectrolyte Membranes*; Academic Press: New York, 1969.
- (31) Fitzgerald, J. J.; Weiss, R. A. *In Coulombic Interactions in Macromolecular Systems*; American Chemical Society: Washington, DC, 1986, Chapter 3, p 35.
- (32) Chen, W.; Sauer, J. A.; Hara, M. *Polymer* **2003**,44,7729.
- (33) Peddini, S. K.; Pham, H. N.; Spinu, L.; Weston, J. L.; Nikles, D. E.; Mauritz, K. A. Manuscript Submitted to Polymer.
- (34) Ngai, K. L.; Paluch, M. *Journal of Chemical Physics* **2004**,120,857.
- (35) Peddini, S. K.; Mauritz, K. A. Manuscript Submitted to Polymer.
- (36) Weiss, R. A.; Sen, A.; Pottick, L. A.; Willis, C. L. *Polymer* **1991**,32,2785.
- (37) Gomez, D.; Alegria, A.; Arbe, A.; Colmenero, J. *Macromolecules* **2001**,34,503.